Interaction between Fluidelastic Instability and Acoustic Resonance

---

John Mahon

Department of Mechanical & Manufacturing Engineering

Parsons Building

Trinity College

Dublin 2

Ireland

May 2008

A thesis submitted to the University of Dublin in partial fulfillment of the requirements for the degree of Ph.D.

Declaration

I declare that I am the author of this thesis and that all work described herein is my own, unless otherwise referenced. Furthermore, this work has not been submitted in whole or part, to any other university or college for any degree or qualification.

I authorise the library of Trinity College, Dublin to lend this thesis.

John Mahon, May 2008

Abstract

The interaction between fluid damping controlled instability and acoustic resonance in normal triangular tube arrays has been investigated by experimental means. Tests are repeated for three array geometries with a single flexible cylinder free to oscillate in the cross flow direction only. The duct acoustics are excited with speakers placed adjacent to the tube array to artificially replicate flow-induced resonance at the second acoustic mode. It is seen that the imposed acoustic field showed no apparent effect on the vibration amplitude for the pitch ratio of 1.58. It is thought that the jet switching observed in pitch ratio of 1.58 obscured the effect of acoustic resonance if it existed. For P/d=1.32, acoustic resonance modifies fluidelastic vibration amplitude, increasing the critical flow velocity and delaying the onset of fluidelastic instability. In a post stable regime, a drop in the amplitude of tube vibration is observed with increasing sound pressure level of the acoustic resonance. In terms of the system dynamics, it is shown that acoustic resonance adds positive damping thus reducing the negative fluid damping. To assess the interaction between fluidelastic instability and acoustic resonance for P/d=1.32, two possibilities are examined based on the framework proposed by Price & Paidoussis [1]. The first examines the effect of acoustic resonance on the static fluid forces on a stationary cylinder and the second the effect of acoustic resonance on the time delay. It is found that at a sound pressure level of $\sim 140dB$, acoustic resonance has no significant effect on the static fluid forces. It is also observed that the assumption that fluid forces scale with dynamic head is incorrect. A non-dimensional relationship is found for the drag force but no simple parameterisation is found for the lift force. The effect of acoustic resonance on the time delay between the tube motion and a point in the flow close to the instrumented

cylinder is measured and for some positions acoustic resonance is seen to modify the time delay. It is proposed that acoustic streaming is affecting the time delay process resulting in the drop in fluidelastic vibration amplitude observed.

Acknowledgments

This thesis would be nothing without the many people that assisted and encouraged me. To all those who advised and worked with me, I sincerely thank you in particular my supervisor Doctor Craig Meskell whose help and guidance over the last three years or so has been invaluable. I would also like to thank Professor John Fitzpatrick for the use of his library and the informative discussions we had.

I would also like to thank the administrative and technical staff Joan Gillen, Alan Reid, Tom Haveron, JJ Ryan, Gabriel Nicholson, Sean Doonan, Gerry Byrne, John Gaynor and Paul Normoyle as without their assistance no thesis could be completed.

To all those in the department and I suppose anyone in the vicinity of the department I apologise for the pain caused by the excessive noise, you can rest easy for now. Or at least your ears can. I would particularly like to that all those who worked in the fluids lab, Eoin, John, Francesco, Cathal, Garreth, Meaghan, Orla, Stephen, Bjorn, Petr, Sergio, Julie, Alessandra, Stephen (Gillen) and Shane, you made it an enjoyable place to work and socialise. I wish you all the best in everything you pursue.

Finally, I would like to thank my parents Johnny and Marie and my sisters Pamela and Carol whose knowledge of tube arrays has also come a long way in three years. Words cant express how much their support and encouragement means to me. And of course, many thanks to my friends who were not only great support but provided well needed social distraction when fluid damping and acoustic resonance took it's toll.

"The important thing in science is not so much to obtain new facts as to discover new ways of thinking about them." Sir William Lawrence Bragg

Contents

List of Figures **xii**

List of Tables **xviii**

Nomenclature **xxi**

1 Introduction **1**

1.1 Objectives & Overview 3

2 State of the Art of FIV in Tube Arrays **5**

2.1 Turbulent Buffeting 6

2.2 Vortex Shedding 9

2.3 Acoustic Resonance 13

2.3.1 Forced Acoustics 15

2.4 Fluidelastic Instability 18

2.4.1 Mechanisms 19

2.4.2 Time Delay 21

2.4.3 Models 24

2.4.4 Forces 27

2.4.5 Interaction between Fluidelastic Instability and Vortex Shedding and/or Acoustic Resonance 30

2.5 Summary 33

3 Experimental Facility and Instrumentation **35**

3.1 Experimental Facility 35

3.1.1 Wind Tunnel . . . 35
3.1.2 Instrumented Cylinder . . . 38
3.1.2.1 Flexible Cylinder . . . 38
3.1.2.2 Pressure Tapped Tube . . . 41
3.1.3 Acoustic Excitation . . . 43
3.2 Instrumentation . . . 44
3.2.1 Accelerometer . . . 44
3.2.2 Microphones . . . 44
3.2.3 Pressure Transducers . . . 45
3.2.4 Flow Velocity Measurement . . . 47
3.2.4.1 Pitôt-static Tube . . . 47
3.2.4.2 Hot-wire Anemometry . . . 47
3.2.5 Flow Visualisation . . . 48
3.3 Data Acquisition . . . 49

4 Effect of Acoustic Resonance on Fluidelastic Instability Quantified 51
4.1 Fluidelastic Instability . . . 51
4.2 Tube Response with Acoustic Resonance . . . 56
4.2.1 Fluidelastic Damping with Forced Acoustics . . . 65
4.3 Possible Physical Mechanisms . . . 69
4.4 Summary . . . 72

5 Pressure Distributions & Fluid Forces 73
5.1 Pressure Measurements . . . 73
5.1.1 Validation of the test set up . . . 74
5.1.2 Surface Pressure Measurements in Tube Arrays . . . 75
5.1.2.1 Pressure distribution, tube displaced . . . 82
5.2 Flow Instability . . . 88
5.3 Fluid Forces . . . 94
5.3.1 Drag Force . . . 95
5.3.2 Lift Force . . . 103
5.4 Effect on Fluidelastic Instability . . . 106

6 Interaction between Fluidelastic Instability & Acoustic Resonance Explored **109**

6.1 Effect of acoustic resonance on static fluid forces 109

6.2 Time Delay 113

6.2.1 Analysis technique 114

6.3 Effect of acoustic resonance on the Time Delay 123

7 Conclusion **127**

7.1 Future Work 129

A Terms related to Vortex Shedding **143**

B Pressure Tapped Tube Drawings **147**

C FEA Analysis of Test Section **149**

D Error Analysis **151**

E Pitch Ratio of 1.97 **155**

E.1 Pressure Distribution 155

E.2 Drag Force 158

E.3 Lift Force 161

F Further Analysis of P/d=1.32 and P/d=1.58 **163**

F.1 Pressure Coefficient; P/d=1.32 163

F.2 Pressure Coefficient; P/d=1.58 165

F.3 Drag Force 166

F.4 Lift Force 171

List of Figures

2.1 Standard Tube Array Geometries 6

2.2 Strouhal Number Charts 12

2.3 Schematic of array and velocity vector diagram 22

3.1 Wind Tunnel Schematic 36

3.2 Test Section 37

3.3 Tube Clamping 38

3.4 Flexibly Mounted Tube & Support 39

3.5 Flexibly Mounted Tube with EMD 40

3.6 Electromagnetic damper in situ 40

3.7 Photograph of the Pressure Tapped Tube 42

3.8 Voltage Regulator Circuit 46

3.9 Pressure Transducer and Voltage Regulating Circuitry 46

3.10 Hot-wire Bridge Circuit 48

4.1 P/d=1.32 RMS of tube motion at three levels of structural damping: $\Delta, \delta_{st} = 0.077$; $\nabla, \delta_{st} = 0.098$; $\circ, \delta_{st} = 0.123$ 53

4.2 P/d=1.58 RMS of tube motion at three levels of structural damping: $\Delta, \delta_{st} = 0.017$; $\nabla, \delta_{st} = 0.023$; $\circ, \delta_{st} = 0.030$ 53

4.3 P/d=1.97 RMS of tube motion: $\Delta, \delta_{st} = 0.017$ 54

4.4 Comparison of measured stability thresholds: $\circ$, Austermann & Popp [2], P/d=1.25; ∇, Austermann & Popp [2], P/d=1.375; Δ, Price & Zahn [3], P/d=1.375; ■, present, P/d=1.32; ♦, present, P/d=1.58. 55

4.5 P/d=1.32. Vibration amplitude against speaker power at $U = 8.9m/s$. 56

4.6 P/d=1.58. Sequence of tests from left to right showing vibration amplitude against speaker power at $U = 9m/s$. •, individual test; Δ, average of the five tests 57
4.7 P/d=1.32. Vibration amplitude against against speaker power at $U = 8.9m/s$ at first acoustic mode 58
4.8 SPL against input power to speaker: ∘, 7m/s and Δ, 8.9m/s 60
4.9 Vibration amplitude against input power to speaker: $\diamond, 7m/s$; and $\triangleleft, 8.9m/s$ 60
4.10 Vibration amplitude against input power to speaker: $\Delta, \delta_{st} = 0.077$; $\nabla, \delta_{st} = 0.098$; $\circ, \delta_{st} = 0.123$ 61
4.11 RMS of tube vibration at $\delta_{st} = 0.088$: Δ, without acoustic excitation and ∘, with artificially excited acoustic resonance (speaker power = 32W) 62
4.12 Time trace of tube displacement. Acoustic excitation applied at $t = 0s$ 62
4.13 Change in vibration amplitude against input power to speaker: $\diamond, 7m/s$ and $\triangleleft, 8.9m/s$ 63
4.14 Change in vibration amplitude against input power to speaker: Δ, $\delta_{st} = 0.077$; $\nabla, \delta_{st} = 0.098$; $\circ, \delta_{st} = 0.123$ 64
4.15 Structural damping against input power to speaker 69
4.16 Acoustic particle velocity and pressure curves at the second acoustic mode 70
4.17 RMS of tube vibration at position 2 at $\delta_{st} = 0.088$: Δ, without acoustic excitation and ∘, with artificially excited acoustic resonance (speaker power = 32W) 71

5.1 Schematic of position angle 75
5.2 Distribution of pressure coefficient over the surface of a cylinder: 1) – , potential flow theory; 2) $- \cdot -$, experimental data from the literature ($Re = 8 \times 10^4$), [4]; 3) ▲, experimental data ($Re = 5.6 \times 10^4$), current study 76
5.3 C_P comparison at the three pitch ratios tested: ∘, P/d=1.32, $Re = 8.93 \times 10^4$; △, P/d=1.58, $Re = 8.77 \times 10^4$; ◁, P/d=1.97, $Re = 8.69 \times 10^4$ 77

5.4 P/d=1.32; C_P at $y/d = 0\%$ and $U = 9m/s$ 78
5.5 P/d=1.58; C_P at $y/d = 0\%$ and $U = 11m/s$ 79
5.6 P/d=1.32; C_P at $y/d = 0\%$ for a range of flow velocity 79
5.7 P/d=1.32; C_P at various positions around the cylinder 80
5.8 P/d=158; C_P at $y/d = 0\%$ for a range of flow velocity 81
5.9 P/d=1.58; C_P at various positions around the cylinder 81
5.10 P/d=1.32; Comparison of C_P for $\triangle$, $y/d = +5\%$; *circ*, $y/d = -5\%$; (a) Re=6.7×10^4; (b) Re=1×10^5 83
5.11 P/d=1.32; C_P at various tube displacements, $U = 7m/s$ 84
5.12 P/d=1.58; C_P at various tube displacements, $U = 11m/s$ 86
5.13 Schematic of tube geometry for P/d=1.32 showing the location of local flow velocity measurements 87
5.14 Time resolved pressure signal; $y/d = 0\%$ at $\theta = 230^o$ 88
5.15 Positions of the velocity and pressure measurements 89
5.16 Local velocity signal (v); (a) $y/d = 0\%$ and $\theta = 20^o$ (b) $y/d = 5\%$ and $\theta = 70^o$ 90
5.17 Flow visualisation at $U = 11m/s$ 91
5.18 Time resolved pressure signal; $y/d = 5\%$ at $\theta = 250^o$ 92
5.19 C_P at various displacements illustrating the deviation from the mean as a result of flow instability 93
5.20 Time resolved pressure signal; $y/d = 10\%$ at $\theta = 250^o$ 93
5.21 P/d=1.32; Drag force, y/d=0% 96
5.22 P/d=1.32; Drag coefficient against Reynolds number at various tube displacements 97
5.23 P/d=1.32; Index relating drag coefficient and Reynolds number 98
5.24 P/d=1.58; Drag force: $\triangle$, Test 1; $\circ$, Test 2; (a) y/d=0% and (b) y/d=5% 98
5.25 P/d=1.58; Drag force at $y/d = 0\%$ 99
5.26 P/d=1.58; Index relating drag force and gap velocity; $\circ$, $U_g < 24.5m/s$, $Re < 6.6 \times 10^4$ and Δ, $U_g > 24.5m/s$, $Re > 6.6 \times 10^4$ 100
5.27 P/d=1.58; Drag force at all tube displacements with averaged fitted lines 100

5.28 P/d=1.58; Drag coefficient averaged at each velocity for all tube displacements . . . 101
5.29 P/d = 1.32; Lift coefficient against Reynolds number at various tube displacements . . . 104
5.30 P/d = 1.58; Lift coefficient against Reynolds number at various tube displacements . . . 105
5.31 RMS of tube motion: Δ, P/d=1.32, δ_{st} = 0.123; ∇, P/d=1.58, δ_{st} = 0.030; $\circ$, P/d=1.97, δ_{st} = 0.017 . . . 107
5.32 Further examination of tube motion from Fig. 5.31 . . . 107

6.1 Pressure Distribution around at U=4m/s: –, no acoustics; $-\cdot-$, Frequency=1092Hz (SPL=140dB) . . . 110
6.2 Pressure Distribution around at (a) U=7m/s and (b) U=10m/s: –, no acoustics; $-\cdot-$, Frequency=1092Hz (SPL=140dB) . . . 110
6.3 Lift and drag force against U_g with and without imposed acoustics. $\triangle$, 0W; ∇, 16W; $\circ$, 32W; $\square$, 64W. . . . 111
6.4 Hot-wire positions around the instrumented cylinder . . . 114
6.5 Central Difference . . . 115
6.6 (a) –, Original signal; $-\cdot-$, Differentiated signal (b) Angular position . 116
6.7 First harmonic fit of the tube motion and flow velocity data . . . 117
6.8 $-$, Tube response, and $-\cdot-$, velocity response, showing a time delay between the two traces . . . 118
6.9 Ensemble averaged velocity $\theta = 165^o$, u - dir; $--$ (red), 1st Harmonic fit; and $-\cdot-$ (black), Harmonic fit (inclusive of 3rd harmonic) . . . 119
6.10 Good Fit: $\theta = 165^o$, u-dir and $U = 10m/s$; (a) Energy distribution at each harmonic (b) Auto-correlation . . . 120
6.11 Poor Fit: $\theta = 150^o$, v-dir; (a) Energy distribution at each harmonic ($U = 4m/s$) (b) Auto-correlation ($U = 7m/s$) . . . 120
6.12 Ensemble averaged Velocity data: – (blue), without acoustic excitation and $-\cdot-$ (red), with artificially excited acoustic resonance (speaker power = 64W) . . . 125

6.13 Ensemble averaged Velocity data: – (blue), without acoustic excitation and $-\cdot-$ (red), with artificially excited acoustic resonance (speaker power = 64W) 126

A.1 Vortex Shedding 143
A.2 Jet Instability [5] 144
A.3 Shear layer Instability [6] 144
A.4 Wake instability [7] 145

B.1 Schematic of the Pressure Tapped Tube 147
B.2 Schematic of the Machined Block(1) - The location of the Pressure Taps on the Tube 148

C.1 FEA model showing the pressure distribution for the second acoustic mode of the test section with P/d=1.32 150

E.1 P/d=1.97; $y/d = 0$, C_P at all velocities tested 156
E.2 $P/d = 1.97$; C_P at various tube displacements, $U = 18m/s$ 156
E.3 $P/d = 1.97$; C_P at various positions around the cylinder for $y/d = 0 - 10\%$ and $U = 13m/s$ 157
E.4 $P/d = 1.97$; Drag force against gap velocity at all tube displacements . 158
E.5 $P/d = 1.97$; Drag Force for all tube displacements averaged 159
E.6 $P/d = 1.97$; Index relating drag force and gap velocity 159
E.7 P/d=1.97; Drag Coefficient (averaged for all tube displacements) against Gap Velocity 160
E.8 P/d=1.97; Lift Coefficient against Reynolds number at various tube displacements 161
E.9 P/d=1.97; Lift coefficient against tube displacement at various velocities 162

F.1 $P/d = 1.32$; C_P at various tube displacements, $U = 4m/s$ 163
F.2 Schematic of position angle 164
F.3 $P/d = 1.32$; C_P at various tube displacements, $U = 10m/s$ 164
F.4 $P/d = 1.58$; C_P at various tube displacements, $U = 5m/s$ 165

F.5 $P/d = 1.58$; C_P at various tube displacements, $U = 8m/s$ 165
F.6 $P/d = 1.58$; C_P at various tube displacements, $U = 14m/s$ 166
F.7 $P/d = 1.32$; Drag coefficient at various velocities. Part 1 167
F.8 $P/d = 1.32$; Drag coefficient at various velocities. Part 2 168
F.9 $P/d = 1.32$; Drag Force generation, $U = 4m/s$, $y/d = 1$, 3, 5, 7 and 10% 169
F.10 $P/d = 1.32$; Drag Force generation, $U = 7m/s$, $y/d = 1$, 3, 5, 7 and 10% 169
F.11 $P/d = 1.32$; Drag Force generation, $U = 10m/s$, $y/d = 1$, 3, 5, 7 and 10%170
F.12 $P/d = 1.32$; Lift coefficient at various velocities. Part 1 173
F.13 $P/d = 1.32$; Lift coefficient at various velocities. Part 2 174
F.14 $P/d = 1.32$; Lift Force generation at various displacements: 1, 3, 5, 7 and 10% at (a) $U = 4m/s$, (b) $U = 7m/s$ and (c) $U = 10m/s$ 175
F.15 $P/d = 1.32$; Lift Force generation at various velocities: $U = 2$, 4, 6, 8, and $10m/s$ at (a) $y/d = 1\%$, (b) $y/d = 3\%$, (c) $y/d = 5\%$, (d) $y/d = 7\%$, and (e) $y/d = 10\%$ 176
F.16 $P/d = 1.32$; Lift Force generation at various velocities: $U = 5$, 8, 11 and $14m/s$ at (a) $y/d = 1\%$, (b) $y/d = 3\%$, (c) $y/d = 5\%$, (d) $y/d = 7\%$, and (e) $y/d = 10\%$ 178

List of Tables

4.1 Velocity range for threshold tests 52

4.2 Fluidelastic stability thresholds 55

4.3 Effective Negative Linearised Fluid Damping, c_f, with U=8.9m/s and various levels of Speaker Power 67

5.1 Velocities and Reynolds numbers tested 74

5.2 Tube Displacement chart 82

6.1 Time Delay (ms) at a range of positions in the flow field 121

6.2 Time Delay (ms) at a range of positions in the flow field with and without acoustic resonance. Shading - illustrates the hot-wire positions and velocities where overlap between the individual time delays measured with and without forced acoustics occurs 123

Nomenclature

Symbol	Description
A_M	Constant
B_M	Constant
C_D	Drag Coefficient
C_L	Lift Coefficient
C_P	Pressure Coefficient
C'_P	Fluctuating Pressure Coefficient
D	Drag Force
D^*	Additional Drag Force Contribution resulting from Tube Displacement
ΔD	Change in Drag Force
E	Fluidelastic Force
E_{hw}	Voltage across the wire in Hot-wire Anemometry
L	Lift Force
L^*	Additional Lift Force Contribution resulting from Tube Displacement
ΔL	Change in Lift Force
M	Number of Harmonics
P	Array Pitch
P/d	Pitch Ratio
P_{ref}	$2 \times 10^{-5} Pa$
P_0	Stagnation Pressure ($\theta = 0$)

Symbol	Description
P_θ	Local Mean Static Pressure
$P_{\theta_{max}}$	Stagnation Pressure when the Tube is Displaced
R	Acoustic Resonance Force
Re	Reynolds Number
T	Turbulent Buffeting Force
U	Free stream Flow Velocity
U_c	Critical Flow Velocity
U_g	Gap Flow Velocity
V	Vortex Shedding Force
V_r	Reduced Gap Velocity
APV	Acoustic Particle Velocity
AR	Acoustic Resonance
dB	Decibel
EMS	Electromagnetic Shaker
EMD	Electromagnetic Damper
FEA	Finite Element Analysis
FEI	Fluidelastic Instability
SPL	Sound Pressure Level
St	Strouhal Number
W	Watts (Speaker Power)
a	Radius of the Duct used in Microphone Calibration
c	Constant
c_f	Linear Fluid Damping
c_s	Linear Structural Damping
c_{sp}	Speed of Sound
d	Tube Diameter
$f_{cut-off}$	Cut-off Frequency

Symbol	Description
f_n	Natural Frequency (Hz)
k_f	Linear Fluid Stiffness
$k(u)$	Constant varying with Velocity
k_s	Linear Structural Stiffness
m_f	Fluid Added Mass
m_s	Modal Mass of the Structure
l	Tube length
n	Index (Power)
q	Index (Power - Kings Law)
u	Local Velocity Component - In Flow Direction
v	Local Velocity Component - Cross Flow Direction
v_M	Velocity at M^{th} Harmonic
y	Tube Displacement
$y*$	Normalised Tube Displacement (y/y_{max})
$\dot{y}$	Tube Velocity
$\ddot{y}$	Tube Acceleration
Δy	Change in Tube Displacement
ρ	Density of Air
ζ	Damping ratio
ω	Natural Frequency (rad/s)
δ	Logarithmic Decrement
δ_{st}	Structural Logarithmic Decrement
$\Delta\phi$	Phase Difference
Δt	Time Delay
τ	Delay - Auto Correlation

Chapter 1

Introduction

Arrays of cylinders are common in many engineering structures such as offshore structures (e.g. oil rigs), chimney stacks, bundles of electrical cables or under water piping. They are also found in power generation applications. Many of these power generation plants have as a major component a large heat exchanger which consists of a bank of circular tubes subject to a cross flow. It is the process of the fluid flowing across the tubes that causes the tubes to vibrate. Flow induced vibration (FIV) is broadly recognised under four phenomena; turbulent buffeting, vortex shedding, acoustic resonance and fluidelastic instability (FEI). The first three are reasonably well understood, however, this is not the case for fluidelastic instability. Furthermore, it is has the potential to be the most destructive of the phenomena. Indeed, fluidelastic instability can destroy a unit within a few hundred hours of operation. Paidoussis [8] reported on a large number of cases where catastrophic failures of tube bundles occurred as a result of fluidelastic instability and to a lesser extent the other flow induced vibration mechanisms. The cost of repairs and the technical and financial implications of shutdowns are of concern to the industry. In the case of nuclear plants, such failures can result in a health and environmental hazard.

As the physical mechanism underlying fluidelastic instability is not well understood, the design procedures to avoid fluidelastic instability are based almost entirely on empirical data. As a consequence, and because of the potentially catastrophic nature of fluidelastic instability, the design guidelines tend to be overly conservative. However with rising costs of fuels and increased competition there is a drive for reducing costs. One such approach might be to operate at higher flow velocities, improving

the heat transfer process and hence, improving efficiency, but this requires reducing the overly conservative operating conditions. In nuclear plants similar approaches are also utilised to use resources more efficiently explicitly to prolonging the useful life of nuclear material by a technique known as stretch out. A paper [9] published by Electricity de France at a recent conference detailed the technique. The approach involves reducing the coolant temperature by reducing the fluid pressure but there are operating constraints on the maximum allowable changes in pressure so the coolant flow velocity has also to be increased thus increasing the possibility of fluidelastic instability.

Such is the destructive potential of fluidelastic instability that a considerable research effort into understanding the phenomenon has been undertaken in the past 40 years. Although the phenomenon is still not well understood some progress in understanding it has been made. It has been shown that there are two mechanisms: fluid damping controlled instability and fluid stiffness controlled instability. It is also apparent that there is a time delay between tube motion and the resulting fluid forces but this has yet to be measured directly. However, there is uncertainty as to whether the mechanism of fluidelastic instability is distinct or whether it could interact with vortex shedding or acoustic resonance. There is evidence in the literature that there might be an interaction between the phenomena. Meskell & Fitzpatrick [10] and Price & Zahn [3] have reported on apparent interaction between fluidelastic instability and acoustic resonance. However, the interaction was not quantified nor was the coupling mechanism between the phenomena explored. One of the aims of this study is to investigate the interaction between fluidelastic instability and acoustic resonance. The first step is to quantify the effect and then examine the interaction between the two phenomena. In addition, an attempt to measure the time delay will be undertaken in this study, in the context of exploring the interaction between fluidelastic instability and acoustic resonance.

It is envisaged that a better understanding of the underlying phenomenon will facilitate improved predictive models leading to less conservative designs. It is also thought that if the interaction between fluidelastic instability and acoustic resonance is understood and if a similar finding to the apparent interaction observed by Meskell & Fitz-

patrick [10] occurs, that is, acoustic resonance suppressing fluidelastic instability. The interaction could be used as a suppression technique to facilitate stretch out without the onset of fluidelastic instability and/or higher flow velocities enhancing the heat transfer process.

1.1 Objectives & Overview

Although there has been a considerable research effort in area of fluidelastic instability in the last 40 years there are still many unknowns in this subject. The work described in this study will concentrate on a number of objectives:

- To quantify the interaction between fluidelastic instability and acoustic resonance. This is achieved by artificially exciting acoustic resonance and comparing fluidelastic tube vibration with and without acoustic resonance. In addition, the effect on the fluidelastic stability threshold and fluid damping is also quantified.

- To explore the interaction between fluidelastic instability and acoustic resonance. This is achieved by examining the effect acoustic resonance on the magnitude of the static fluid forces and the phase dependency. The latter requires the time delay to be measured. Measuring the time delay in itself will further contribute to the understanding of fluid damping controlled instability.

In attempting to achieve these principal objectives a number of smaller objectives have also been completed:

1. A comprehensive set of experimental data has been measured to be used for validation of models.

2. A better understanding of the force generation mechanism and quantification of the effect of static displacement of a single cylinder in a rigid normal triangular array.

3. An investigation into the relationship between the fluid forces (lift and drag) and dynamic head.

This thesis is organised as follows.

Chapter two reviews the state of the art, identifying deficiencies in the literature and expanding on the ones that will be addressed in this document.

The objectives contained in this document will be attempted to be satisfied by experimental means. Chapter three details the experimental facility as well as the instrumentation used in this study.

Chapter four quantifies the interaction between fluidelastic instability and acoustic resonance. Quantifying the effect on the tube vibration amplitude, threshold velocity and the system dynamics (damping).

Chapter five presents some baseline tests for the mean pressure distribution and forces on a cylinder in the third row of three normal triangular arrays. These tests are also discussed in conjunction with the fluidelastic instability behaviour.

Chapter six explores two possibilities for the interaction between the two phenomena. The first possibility examines the effect of acoustic resonance on the magnitude of the static fluid forces. The second possibility examines the effect on acoustic resonance on the phase dependency of the fluidelastic force i.e. the effect of acoustic resonance on the time delay between tube motion and the resultant flow reorganisation close to the measurement cylinder (essentially the fluid forces).

Chapter seven summaries the various observations of the study and presents the conclusions drawn. Further work which might be explored in the future is also discussed.

Chapter 2

State of the Art of FIV in Tube Arrays

Flow induced vibrations (FIV) in tube arrays have been subject to much research in the past. There are a number of reviews of the state of art in the literature [11, 12]. Flow induced vibrations is broadly recognised under four phenomena; turbulent buffeting, vortex shedding, acoustic resonance and fluidelastic instability. The first three of the phenomena are reasonably well understood, however, the latter is not so well understood and it is potentially the most destructive of the phenomena. This was only too well illustrated by Paidoussis [8] who reported on the practical cases of the destructive nature of flow induced vibrations and in particular the destructive nature of fluidelastic instability. Such are the implications of flow induced vibrations, they are now considered as a design criterion of nuclear steam generators and heat exchangers.

The tubes arrays studied in the literature vary in pitch and geometry. There are four standard tube array geometries. A schematic of the geometries is shown in Fig. 2.1. Normal square and rotated (parallel) triangular arrays are often referred to as in-line arrays while normal triangular and rotated square are often referred to as staggered arrays. This study is exclusively concerned with normal triangular arrays. However, all array configurations will be considered in the literature survey. Primary focus will be on single phase flow as two phase flow introduces further complexity into an already complex problem. The literature review will examine the phenomena independently and in the case of acoustic resonance, artificial excitation will also be examined. In addition, the apparent interaction between fluidelastic instability and

vortex shedding and acoustic resonance will also be discussed.

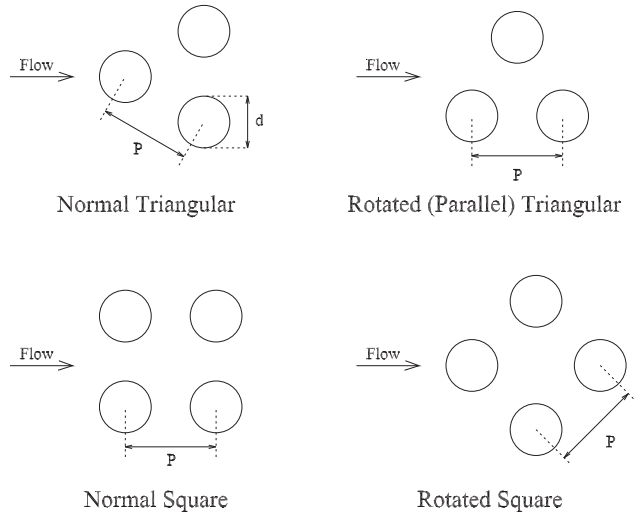

Figure 2.1: Standard Tube Array Geometries

2.1 Turbulent Buffeting

High levels of broadband turbulence are inevitable in tube arrays. In fact it may be desirable for enhanced heat transfer. The turbulence in the flow causes random pressure fluctuations on the cylinders. Hence, each cylinder experiences a random buffeting force and this occurs at all flow velocities. The magnitude of the force is usually small. Nonetheless, because the mechanism is always active, it is important to consider it when designing against fretting wear at the supports and fatigue damage. Longer term, both fretting and fatigue damage will lead to tube failures. Although the mechanism is well understood, prediction of vibration amplitude is poor. The amplitude response is known to scale with some power of velocity. In Paidoussis' [11] review; Gibert *et al.* and Nicolet *et al.* reported that the vibration amplitude scales approximately with $U^{3/2}$ when cylinder response is primarily due to turbulent buffeting. Price *et al.* [13] observed a linear relationship whereas Pettigrew & Gorman [14] documented the velocity squared for liquid flow. In the review of Weaver & Fitzpatrick [12], the authors suggest that a more complex dependency on flow velocity, other than the generally assumed dynamic head, is required to fit the data. One reason for the scatter in available data is because all geometries and pitch ratios are

compared together. This approach would seem to be incorrect as the flow in in-line arrays produces flow lanes and this is not the case for staggered arrays. Furthermore, the flow in both staggered and in-line arrays for differing pitch ratios has also been shown to be different. This can be observed when the pressure distribution around a cylinder within an array is examined. Savkar [15] reported that the fluid forces are dependent on the blockage and/or pitch ratio. The differences in flow for different array geometries and the affect of blockage might help explain why such differences in the amplitude response were reported.

It is well known that the first two rows of a tube array are not typical of a cylinder deep inside a tube array. This is because the flow is evolving in the first two rows. Deeper in the tube array, the tube array acts like a grid and generates high levels of turbulence resulting in a pattern of its own. Such findings have been reported by Zukauskas [16], Zdravkovich & Namork [17, 18] and others. Zdravkovich & Namork [17] reported that the interstitial flow for a staggered array ($P_T = 1.375; P_L = 1.1875$) changed up to the third row and then remained almost unchanged. Grover & Weaver [19] using a rotated triangular array with air cross flow and P/d=1.375 reported that turbulence intensity reached a maximum by the fifth row. Thereafter small changes in the flow occurred. They suggested that five or six tube rows should be adequate for simulating a tube bank [20]. Weaver & El-Kashlan [21] reported similarly. Fitzpatrick & Donaldson [22] reported on the row depth effects in an in-line tube array ($P_T = 1.75$; $P_L = 1.97$) on turbulence and acoustic resonance. The magnitude of turbulence intensity was approximately constant beyond the seventh row. Chen & Jendrzejzcyk [23] reported that local turbulence levels reach a steady state once the flow has passed three to four rows in an in-line array (P/d=1.75). Fitzpatrick *et al.* [24] report on three twenty row in-line arrays ($P_L = 1.97, 1.73$ and 1.73; $P_T = 1.97, 1.97$ and 1.73) where it was found that turbulence structures were still evolving at the fifteenth row but turbulence intensity had generally settled by the tenth row. The differences in the literature regarding the development of turbulence levels throughout the arrays results from the variety of geometries and pitches reported as well as the flow characteristics associated with the Reynolds numbers tested. However, it is clear that in-line and sparser staggered arrays need more rows to develop stationary turbulence.

The effect of incident turbulence on the flow has also been widely reported. Batham [25] found that the presence of a turbulent incident flow had a large effect on the pressure distributions around the widely spaced tubes (P/d=2), but no effect on the narrowly spaced (P/d=1.25) tubes (both where in-line arrays). Price & Paidoussis [26] reported similarly. There are also a few studies that report on the effect of incident turbulence on fluidelastic instability. Southworth & Zdravkovich [27] reported on the vibration response of a single and double row of fully flexible cylinders in-line for a number of pitch ratios. The fluidelastic response was completely changed resulting in an increased critical velocity. Reports by Frankin & Soper [28] are in contraction, with a decrease in critical velocity observed. Chen & Jendrzejczyk [29] indicated that turbulence may either increase or decrease the critical flow velocity for fluidelastic instability, depending on the turbulence characteristics. Rottmann & Popp [30] reported that upstream turbulence stabilised multiple flexible cylinders in the upstream rows of the rotated triangular array (P/d=1.375). This was also found to be the case for a single flexible cylinder in a previous study by Romberg & Popp [31]. Price *et al.* [13, 26] found that turbulence generators had little effect on the onset of fluidelastic instability for rotated square (P/d=2.12) and in-line (P/d=1.5) arrays, respectively. The differences in the reported literature are due to the position of the tube being investigated. In the studies of Price *et al.* the tube position was deep in the array where the other researchers referred to a cylinder in the front rows or upstream rows which are know not be representative of a cylinder deep within a tube array and as pointed out by Price *et al.*, the interstitial flow characteristics beyond the first few rows are governed by the array itself, independent of upstream conditions. Theoretically, Rzentkowski & Lever [32] reported that turbulence changes the limit cycle amplitude not the stability threshold (for the case where there was no hysteresis in the response curve).

2.2 Vortex Shedding

Flow periodicity in the absence of structural motion may result in self-controlled vibrations. The problem can be treated as a simple forced response if the frequency of the flow periodicity is well removed from the natural frequencies of the structure. However, if the flow periodicity coincides with the natural frequency of the structure, resonance occurs. If the response amplitude becomes large, fluid excitation is controlled by the structural displacement. The velocity range this occurs at is known as the "lock-in" region.

Pre 1960's, vortex shedding was assumed to be the major cause of vibration in heat exchangers. Owen [33] argued that discrete vortex shedding could not occur in closely packed arrays and attributes the excitation to a peak in the turbulence spectrum. The work of Fitzpatrick & Donaldson [22] supported Owen's argument. They observed two Strouhal numbers up to the fourth row of an in-line array ($P_T = 1.75$; $P_L = 1.97$). Thereafter differences in the flow structure were observed and the single peak becomes more broadband similar to that suggested by Owen.

Flow visualisation studies were carried out to resolve the issue regarding vortex shedding in tube arrays. Weaver & Abd Rabbo [34] published a flow visualization study of water flow in a fully flexible in-line array (P/d =1.5), which shows periodic vortex shedding. This was somewhat inconclusive as the tubes were vibrating and the photos were not very clear. Several other flow visualisation studies followed for various array geometries. Abd-Rabbo & Weaver [35] observed laminar vortex formation at low Reynolds number for a rotated square array (P/d=1.41). Price *et al.* [36, 37] showed photographs of vortex shedding in a rotate square (P/d=1.5) and parallel triangular (P/d=1.375) arrays, respectively. Weaver *et al.* [38] presented images of vortex shedding in rotated square arrays (P/d=1.21-1.83). More recently, the images of Oengoren & Ziada [5, 39] who investigated both in-line and staggered array configurations subject to water cross flow best illustrate vortex shedding in tube arrays.

The predication of vortex shedding by means of Strouhal number charts has also received considerable attention. However, there was much confusion and scatter in the available data. So much so, in their review in 1988, Weaver & Fitzpatrick [12] dismiss

much of the earlier Strouhal data as unreliable as it was obtained from either tube resonance or acoustic resonance data. They cite this as the reason for the confusion in the stability maps of Fitz-Hugh [40] and Chen [41]. In the interim, much research has been done in relation to Strouhal number charts for vortex shedding for all of the standard array geometries. Weaver *et al.* [42] measured Strouhal numbers in eight arrays at off resonance conditions with two different pitch ratios for all the four standard arrays. Their results along with the data from the literature were plotted for each of the four standard array configurations. Some scatter in the data exists and they suggest that this was due to some Strouhal number data being obtained at resonance. The scatter in the data was also attributed to multiple Strouhal numbers, measurement position dependency and a Reynolds number dependency for some arrays as previously reported by Fitzpatrick *et al.* [24]. Since then, many researchers have reported multiple Strouhal numbers for all standard array configurations and the measurement position dependency of Strouhal periodicities for example Weaver *et al.* [38].

Many researchers focused on one standard array geometry and proceeded to get a better understand of vortex shedding in that geometry. Removing resonant data, Weaver *et al.* [38] showed that Strouhal number data in the literature for rotated square arrays fit reasonably well into two curves as a function of pitch ratio. Their experimental results indicated that the higher Strouhal number was due to vortex shedding in the front row and a lower Strouhal number for vortex shedding in the inner rows the difference in frequency resulting from the difference in local flow and both were caused by wake instability.

Oengoren & Ziada [5, 6, 43, 44] (Buhlmann [6]) have conducted a number of studies on in-line arrays suggesting that there are three different flow instabilities which can generate flow periodicities in in-line arrays; jet instability, wake instability and shear-layer instability (see Appendix A for explanations). For large spacing arrays, both jet and wake instabilities can occur but not simultaneously. Only the wake instability can excite acoustic resonance. For intermediate spacing arrays jet instability occurs. Acoustic resonance can be excited by shear-layer instability but this mode was suppressed at off-resonance conditions. Jet instability dominates for smaller spacing arrays. Again, shear-layer instability was the excitation source of acoustic resonance.

Strouhal number charts for vortex shedding and acoustic resonance are presented in Ziada [45] where the former uses tube diameter and the latter uses streamwise tube spacing as the length scale to be used in the Strouhal number formulation.

Ziada & Oengoren [7] produced Strouhal number charts for parallel triangular arrays (P/d=1.2-4.2) as a function of pitch ratio. Three Strouhal numbers were observed. The highest frequency term which was also the weakest component was found at low Reynolds numbers in closely packed arrays and is caused by shear-layer instability. A Strouhal number associated with vortex shedding from the front row was also observed. The strongest but lowest frequency component was attributed to alternate vortex shedding in the wakes of inner rows and was found to dominate at all rows for higher Reynolds numbers. It was also found that natural vortex shedding phenomenon did not excite acoustic resonance.

Polak & Weaver [46] and Oengoren & Ziada [39] studied vortex shedding phenomenon in normal triangular arrays and observed two different Strouhal numbers that originated from different vortex shedding frequencies in the front and inner rows. Both studies provide charts and empirical formulae to predict Strouhal numbers and cite that the flow structure was dominated by wake instability. The former conducted work on nine pitch ratios (P/d=1.14-2.67). It was observed that the lower frequency component was caused by the second row alternate vortex shedding. The higher frequency velocity fluctuations result from alternating vortex shedding in the first row tubes. The smallest pitch ratio (P/d=1.14) was the only exception where no high frequency component was observed. The Strouhal number charts and formulae presented in [46] originate from Weaver *et al.* [38] and Zukauskas & Katinas [47]. Oengoren & Ziada [48] reported on a range of pitch ratio (P/d=1.61, 2.08*and*3.41). They observed three Strouhal numbers. A high frequency component was observed from alternate vortex shedding in the front rows and a lower frequency component from alternate vortex shedding in the rear rows. The third component resulted from a non-linear interaction between the higher and lower shedding frequency components. The lower frequency component at the rear rows was very weak in the compact arrays. It increased in strength when the spacing was increased, until it dominated the whole array at large spacing ratios, where the high frequency component reduces. It was

also observed that Strouhal number charts based on vortex shedding can be used to predict against acoustic resonance. Figure 2.2 presents Strouhal number charts constructed from empirical formulae of Weaver *et al.* [38], Zukauskas & Katinas [47] and Oengoren & Ziada [48].

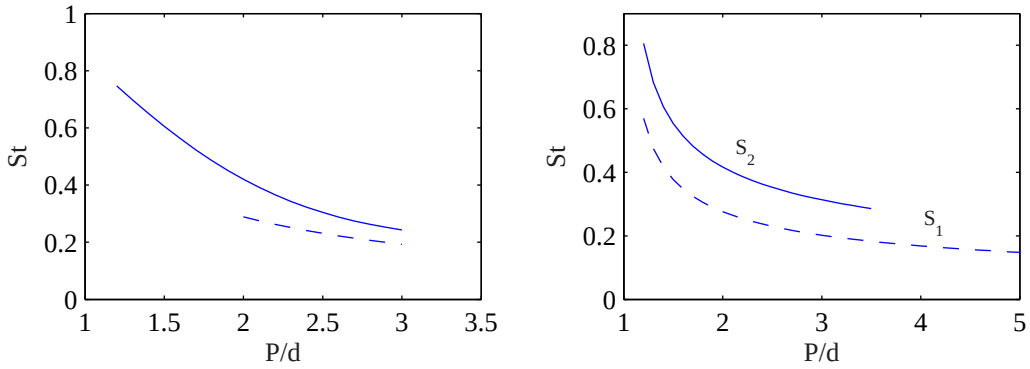

- -, Weaver *et al.* (P/d $\geq$ 2), [38] and –, Zukauskas & Katinas, [47]

Oengoren & Ziada, [48]

Figure 2.2: Strouhal Number Charts

2.3 Acoustic Resonance

Acoustic resonance may occur in tube arrays subject to gas cross flow and is characterised by an acoustic standing wave. The wave propagation is normal to the axes of the tube and the flow direction. Noise levels in excess of 160dB (2000Pa 4.84m/s) have been reported. In addition to the nuisance caused by the excessive noise, such high sound pressure levels can cause structural damage. The frequency of acoustic resonance in a duct containing a tube array was dependent on the number of tubes, as outlined by Parker [49]. Parker refers to an effective speed of sound. In effect, the speed of sound does not change, the distance travelled changes as the sound wave has to travel around the tubes, resulting in the change in frequency.

Most of the papers in the literature that refer specifically to acoustic resonance are related to acoustic damping and the prediction and suppression of the acoustic resonance.

Several damping criteria can be found in the literature to predict whether acoustic resonance will materialise or not. Chen [50] proposed a formula for the damping parameter of in-line arrays which included: Strouhal numbers, pitch ratio and Reynolds number. Fitpatrick [51] pointed out that Chens criterion does not allow for geometric scaling. Fitzpatrick [52] re-worked Grotz & Arnold's criterion [53] and accounted for geometric scaling by introducing the Reynolds number alongside Mach number at resonance and acoustic Strouhal number. A revised version of this criterion was presented by Fitzpatrick & Donaldson [54] improving the data correlation and reducing the scatter in the data. These criteria [50, 52, 54] were only for in-line arrays. Ziada *et al.* [6] outlined an alternative criterion which included a critical Reynolds number (uses critical gap velocity). Like the other criterion, the geometry of the array was included by introducing the pitch ratio. The last parameter was a scaling parameter which accounted for the effective speed of sound (Parker [49]) in the form of a Reynolds number. Using the parameters outlined, two relationships were developed. The first for in-line arrays, plots the criterion against square of longitudinal pitch. The second was for staggered arrays and was plot against L/d where L was the distance between first and third rows and d was tube diameter. The criterion correlated the data reasonably well, however, some scatter still remains.

There has also been much confusion about the excitation source of acoustic resonance. Various researchers include turbulence, vortex shedding and jet instability and combinations of the above. It is now apparent that the different excitation mechanisms result from the different geometries. For staggered arrays, like normal triangular and rotated square arrays it has been shown that vortices generated by wake instability dominate the flow (Weaver *et al.* [38]; Polak & Weaver [46]; Oengoren & Ziada [48]). For normal triangular arrays, Oengoren & Ziada [48] showed that acoustic resonance was excited by the natural flow periodicities. Hence, Strouhal number charts associated with off-resonant conditions can be used to predict acoustic resonance. In contrast, Ziada & Oengoren [44] has shown for in-line arrays, vortices are generated by jet instability and grow in size and strength with row depth and increasing velocity. Using available data from the literature, Fitzpatrick [52] examined the techniques used to predict resonance in in-line arrays. It was concluded that acoustic standing waves can be excited by a combination of vortex shedding, turbulent buffeting and broadband turbulence. Ziada & Oengoren [7] suggest that the acoustic excitation mechanism for parallel triangular arrays was similar to in-line arrays citing alternate vortex shedding caused by shear-layer instability as the excitation mechanism. It is suggested that the Strouhal numbers charts based on natural flow periodicities at off-resonant conditions cannot be used to predict the occurrence of acoustic resonance. Ziada *et al.* [6] attributes this result to the symmetric shedding of vortices at off resonance conditions not being able to excite transverse acoustic modes.

It has also been reported that acoustic resonance can influence flow periodicities. Price & Zahn [3] reported that acoustic resonance organised the flow through a seven row normal triangular tube array with pitch ratio of 1.375. Normally no flow periodicities where found beyond the second row. Coincident with the acoustic resonance ($\sim 120dB$ downstream of array), flow periodicities where observed throughout the whole array at a frequency equal to that of the acoustic tone. A number of researchers have also used artificially excited acoustic resonance to influence vortex shedding and these will be discussed below.

It is also important to note that other flow induced vibration phenomena can be modelled using five or six rows of tubes but this in not the case for acoustic resonance.

Fitzpatrick & Donaldson [55] reported on acoustic resonance in four in-line arrays ($P_L = 1.97$ 1.97 1.5 and 1.3; $P_T = 1.73$ 1.97 1.73 and 1.9). For each configuration the number of rows where increased from one to in excess of twenty rows. It was found that row depth effects were considerable with the acoustic Strouhal number increasing with increasing row depth. After fifteen rows the Strouhal number settles but this was geometry dependent. The acoustic response of a tube array of less than ten rows was different to that of a tube array of more than fifteen rows. Tube pitch ratio has also to be considered. Hence, row depth effects are considerable when studying acoustic resonance and this must considered when relating controlled experiments to that of real world problems.

A number of techniques to suppress acoustic resonance have also been developed. These included, increasing acoustic damping by introducing a liner or using Helmholtz resonators; other researchers have removed cylinders; the most common approach appears to be the introduction of baffles. A comprehensive list of the suppression techniques used can be found in [12, 56]. More recently, work conducted by Eisinger and his colleagues examine the optimum location of baffles. Eisinger & Sullivan [57] show that the decision to locate baffles on the basis of frequency was erroneous. They report that baffles do not change the dominant acoustic frequencies. The introduction of baffles distorts the acoustic waves increasing the resistance of the tube array to acoustic resonance. A general procedure on the effectiveness of baffles based on acoustic particle velocity mode shape functions was also presented. However, Feenstra *et al.* [58] reported that precise spacing of inserted double baffles was not required to suppress the first and second acoustic modes.

2.3.1 Forced Acoustics

Forced acoustics has been widely used in ducts for various bluff bodies e.g. plates, single tubes or tubes in tandem (for example [59, 60, 61, 62, 63, 64, 65]) as well as two studies on tube arrays [66, 67]. There are also papers reporting an apparent interaction between fluidelastic instability and acoustic resonance, these will be discussed later (section 2.4.5) as the resonance was naturally occurring.

Forced acoustics can be applied using two approaches; internal and external excita-

tion. External forced acoustics is more widely used and influences the wake. Sound is applied in the region of the bluff body. Internal forced acoustics influences the boundary layer of the bluff body and sound is introduced on the surface of the bluff body. The current investigation employs external acoustic excitation and as such, will now focus on this method of excitation. With external acoustic excitation the speakers are generally located at the test section wall. Kacker & Hill [65] reported the importance of a break in continuity of the wall through which sound may be introduced as without it, it was not possible to establish a standing acoustic wave in a wind tunnel using an external sound source. The break in continuity of the wall causes it own problems. Therefore, caution must be taken with the setup to avoid separation along the tunnel walls. For example, Hall *et al.* [62] opening in the wind tunnel consisted of perforating the side wall. Welsh *et al.* [68] removed part of the side walls and have speakers on both sides connected in anti-phase. They placed a thin gauze over the removed section of the side walls to prevent adverse flow effects. Positioning of the speakers is important as noted by Welsh *et al.* [68]. The acoustic amplitude reduces exponentially both upstream and downstream requiring speakers to be located close to the bluff body. Furthermore, the positioning of sinks and sources are important in relation to the position of the speaker as trying to excite acoustic resonance with the speakers located at a sink will make excitation difficult. If the sound pressure level is high enough the sound is fedback onto the separating shear layers causing the vortices to be shed at the resonant sound frequency in a coherent manner. The sound pressure level depends on a balance between the rate of conversion from flow energy to acoustic energy and the rate of dissipation. The rate of dissipation is dependent on the number of tubes; hence, the sound pressure level is dependent on the number of tubes in the array. Also, when one sets out to excite the natural acoustic modes of the duct, it is only natural that the correct excitation frequency must be obtained. With an array of cylinders in the duct, the duct behaves differently as mentioned previously, Parker [49] who referred to an effective speed of sound in a tube array. This effectively means a change in the duct natural frequencies. So, to get the natural frequencies of the duct, the measurement must be made in the array. Downstream of the array, the measured frequency is higher than in the array but lower than an empty duct. All of the above

need be considered for acoustic excitation.

For an in-line array (P/d=1.73) Fitzpatrick *et al.* [67] reported that the mean pressure on the surface of a cylinders (thirteenth row) changed substantially when acoustic excitation at the first acoustic mode was applied. At non-resonant conditions, velocity gradients across the array were uniform, however, severe velocity gradients were observed during resonance. For a single cylinder, Peterka & Richardson [59] suggested that the velocity induced by the sound influenced vortex shedding not the sound pressure level. Similar findings where reported by Kacker & Hill [65, 69] for a single cylinder and two cylinders and Blevins [60] for a single cylinder. Feenstra *et al.* [66] reported on acoustic induced vibration for a flexible tube located in the middle row a of a fifteen row array ($P_L = 1.083$; $P_T = 1.57$) at three transverse positions. Acoustic pressure gradient caused tubes to vibrate in the absence of flow. A review of the available literature reveals that forced acoustics have been used in tube arrays but not in conjunction with fluidelastic instability.

2.4 Fluidelastic Instability

Fluidelastic instability produces large amplitude self-excited vibrations at the natural frequency of the structure. It is now recognised as the excitation mechanism with the greatest potential for causing damage in tube arrays. However, this was not always the case. Prior to the 1960s the prevailing thinking was that vortex shedding was the main cause of the vibration problems. It wasn't until 1962 when Roberts described a mechanism of self-excited oscillations (fluidelastic instability) in his PhD thesis. The study was not published until 1966 [70] when it appeared as a monograph. Roberts reported on the vibration of a single and a double row of cylinders and observed tube motions in the in-flow direction with adjacent tubes moving out of phase. The mechanism he described was jet-switching, where the jet between adjacent tubes switched direction in phase with the tube motions. Roberts realised there was a hysteresis in the cylinder drag. Hence, to sustain tube motion, the energy imparted to the structure had to be greater than the energy dissipated by the structure. Roberts suggests that jet switching may occur only if reduced critical velocity, $U_c/f_n d$, is approximately greater than 60. Roberts extended his analysis to develop an expression to calculate the flow velocity to initiate fluidelastic instability. He combined the traditional aeroelastic damping parameter (mass-damping parameter) and critical reduced flow velocity.

Agreement between theory and Roberts own experimental data was quite good. However, Price [71] reported that agreement between Roberts theory and with results available from the literature was poor. This was the case as Roberts assumed cylinder motion to be in the in-flow direction while most of the compared data report motion mainly normal to the in-flow direction. Hence, the analysis was limited to predicting vibration in the in-flow direction.

In 1970, Connors [72] proposed a FEI mechanism independent of jet switching for a single row of tubes with P/d=1.41. Connors predicted the reduced velocity with a similar form to that of Roberts expression:

$$U_c/f_n d = K\delta_r^{0.5} \tag{2.1}$$

where K is dependent on the array geometry. Eqn. 2.1 became widely accepted. Many

researchers have reported various forms of K and the power term in an effort to find the "correct" values and are discussed in Price [73]. Price also discusses the deficiencies of the Connors' model and concludes that emphasis on improving the modelling of fluidelastic instability rather than attempting to modify Connors equation to fit the data should be pursued. It now recognised that the Connors equation has been misused in situations for which it was not intended, notably for tube arrays where it has been shown to underestimate the critical velocity, and for high enough $U_c/f_n d$ where jet switching may occur.

In the following decade, the mechanism of fluidelastic instability reinforced its position as the flow induced vibration mechanism with the potential to be the most destructive mechanism. This was further supported by work published by Paidoussis [8] who reported on practical cases of tube failures due flow induced vibrations. He revisited cases where originally vortex shedding was deemed to have caused the damage, and after reassessing the evidence, attributed the damage to fluidelastic instability. In 1981 Paidoussis [11] reviewed the state of the art of flow induced vibration in tube arrays and concluded that the field was in considerable disarray. Similar conclusions were also formed in the review of Weaver & Fitzpatrick [12].

2.4.1 Mechanisms

In the 1980s research concentrated on obtaining a better understanding of mechanisms underlying fluidelastic instability using both theoretical and experimental approaches with the ultimate goal of better predictive capabilities. The first major break through was that of Chen [74, 75] in 1983. Chen's model employed empirical fluid force coefficients obtained from data provided by Tanaka & Takahara [76]. Agreement between the model and the experimental stability curves was quiet good. This was not surprising as experimentally obtained fluid force coefficients were employed as empirical input into the model. Unfortunately, these coefficients are highly dependent on array type and pitch, hence, the results can not be generalised. Nonetheless, Chen's analysis gave an insight into the fluidelastic mechanism. Chen [74, 75] examined the instability mechanisms and the stability criteria based on previously developed mathematical model. His analysis resulted in the formulation of two instability mechanisms; fluid

damping controlled instability and fluid stiffness controlled instability. The existence of two distinct mechanisms was also later shown by Price & Paidoussis [1]. Experimental validation of the existence of two vibration mechanisms did not occur until the early 90s. Price & Kuran [77] using a rotated square array with P/d = 2.12 reported a minimum of three flexible cylinders for fluidelastic instability to occur. This demonstrated the existence of the fluid stiffness controlled mechanism which requires fluid coupling between adjacent cylinders (multiple degrees of freedom). Prior to this, the available experimental data was inconclusive, neither proving nor disproving the existence of the two mechanisms. This predicament occurred as much of the experimental data was for a single flexible cylinder, proving the existence of one mechanism, fluid damping controlled instability.

Chen [74, 75] and Price & Paidoussis [1] reported that fluidelastic instability was controlled by damping controlled instability mechanism for low mass damping parameter, $m\delta/\rho d^2$, and stiffness controlled for large mass damping parameter. Price & Paidoussis [1] found a boundary between the two regimes at approximately $m\delta/\rho d^2 = 300$. For $m\delta/\rho d^2 < 300$, one flexible cylinder will go unstable at approximately the same onset velocity as a multiple flexible cylinder setup. This was later shown experimentally by Lever and Weaver [78]. Both Chen and Price & Paidoussis reported damping controlled instability was as a result of a negative fluid damping causing instability. This was verified experimentally by Weaver & El-Kashman [79] who reported on parallel triangular array P/d=1.375 and air as the working fluid. Weaver & El-Kashman found that the fluid damping increased linearly until 50% of the stability threshold then approached zero at the onset of instability. Granger *et al.* [80] also reported similar findings for a normal square array with a pitch ratio of 1.44. The phenomenon was characterised by a decreasing cross-flow frequency and a near zero damping ratio. The fluid damping increased first and then decreased towards zero where the onset of fluidelastic instability occurs. More recently, Meskell & Fitzpatrick [10] measured both the linear and non-linear cubic damping and stiffness terms for a normal triangular array with $P/d = 1.32$ and air cross-flow where it was found that amplitude of the limit cycle amplitude was determined by the non-linear damping term.

In the late 1980s Paidoussis & Price [81] attempted to further their findings from a

previous paper [1] and shed light on the mechanisms underlying fluidelastic instability of cylinder arrays in cross flow by means of quasi-steady fluid dynamic framework. They provided links to well-known classical galloping and two degree of freedom wake flutter mechanisms. Furthermore, they reported that classical galloping differs to that (fluid damping controlled mechanism) observed in cylinder arrays and the latter was dependent on the time delay associated with the wake flow adjusting to tube motion.

2.4.2 Time Delay

In addition to the existence of two types of fluidelastic instability mechanisms, it has been suggested that there is a time delay between tube motion and the resulting fluid forces at the root of fluid damping controlled instability. The exact nature of the time delay is unclear and has yet to be measured directly. However, there is some evidence that it exists; Granger & Paidoussis [82] indirectly measured the cause of the time delay using experimental data and a quasi-unsteady model. Abd-Rabbo & Weaver [35] conducted a flow visualisation on rotated square array with pitch ratio 1.41 and water cross-flow. For a single flexible cylinder flow visualisation "revealed clear flow redistribution with a phase lag" because of fluid inertia. Numerous studies have measured fluid stiffness and damping from which the time delay could be inferred e.g. Tanaka & Takahara [76] and Chen & Srikantiah [83].

The governing equation of motion for a single degree freedom cylinder, oscillating in the direction normal to the mean flow only, is;

$$M_s\ddot{y} + c_s\dot{y} + k_s y = E(y, \dot{y}, \ddot{y}, U) \tag{2.2}$$

where E is the dynamic fluidelastic force acting on the tube. Eqn. 2.2 assumes the effects of vortex shedding and turbulent buffeting are ignored, which is not strictly correct but sufficient for a simplified approach. However, the detail of the function on the right is still unknown, however there are a number of models available in the literature for it (review of models [71]). Many of the models decompose E into a number of fluid force coefficients. However, all assume that the fluid forces are dependent on the dynamic head. Hence, the fluidelastic behaviour of a single flexible cylinder could be characterised by two fluid forces (lift and drag). It is also apparent

that the inclusion of a time delay or phase lag is a prerequisite for the models developed, as without the time delay the phenomenon cannot be modelled. The uncertainty as to the origin of the time delay is borne out by the different physical mechanisms for the inclusion of a time delay or phase lag in the models to predict fluidelastic instability as will be discussed below.

Andjelic & Popp [84] have shown the importance of including a time delay in the model and compared their experimental data with the "wavy wall channel model" developed by Lever & Weaver [85]. The time delay proposed in the Lever & Weaver model was obtained from various geometric length scales associated with the array geometry. However, Andjelic & Popp found that the fit between this approach and their experimental data was poor. By modifying the time delay, they obtained a much better fit.

The importance of a time delay as well as the different physical interpretations for the inclusion of a time delay have been discussed above. The next section examines how the time delay associated with fluid damping controlled instability results in a negative fluid damping leading to instability. In this example a quasi-steady analysis[1] is used. The model consists of a single flexible cylinder free to oscillate in the lift direction (y) only with all other cylinders in the array been rigid. The equation of motion of the cylinder in the y direction is

$$M_s\ddot{y} + c_s\dot{y} + k_s y = F_y \tag{2.3}$$

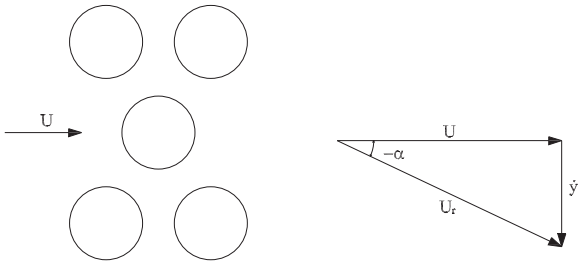

Figure 2.3: Schematic of array and velocity vector diagram

[1]Quasi-steady assumption: the forces acting on the oscillating cylinder are approximately the same as the static forces at each point of the cycle of oscillation, provided that the approach velocity is properly adjusted to take into account the velocity of the cylinder.

F_y may be written as

$$F_y = \frac{1}{2}\rho U_r^2 ld\left(C_L cos(-\alpha) - C_D sin(-\alpha)\right) \tag{2.4}$$

where U_r and α are

$$U_r^2 = [U^2 + \dot{y}^2]^{1/2} \qquad\qquad -\alpha = sin^{-1}(\dot{y}/U_r)$$

C_L and C_D are the static lift and drag coefficients, respectively. Assuming small motions about the equilibrium position the linearised form is

$$C_L = C_{L_0} + \left(\frac{\partial C_L}{\partial y}\right) y \tag{2.5}$$

and similarly for C_D. Substituting C_L and C_D with their linearised form and simplifying the expression results in

$$F_y = \frac{1}{2}\rho U^2 ld\left[\left(\frac{\partial C_L}{\partial y}\right) y - C_{D_0}\left(\frac{\dot{y}}{U}\right)\right] \tag{2.6}$$

Eqn. 2.6 describes the static fluid force on the cylinder. However, this expression does not include the time delay between tube motion and fluid dynamic forces generated thereby. As discussed above there are a number of different physical mechanisms for the inclusion of a time delay. In this example the time delay used is the expression used in Price & Paidoussis [1] $\Delta t = \mu d/U$ ($\mu \sim 1$). Taking the time delay into account and assuming harmonic oscillations, Eqn. 2.6 maybe written as

$$F_y = \frac{1}{2}\rho U^2 ld\left[e^{-i\omega\Delta t}\left(\frac{\partial C_L}{\partial y}\right) y - C_{D_0}\left(\frac{\dot{y}}{U}\right)\right] \tag{2.7}$$

Combining Eqn. 2.3 and 2.7 yields;

$$\ddot{y} + \left[\left(\frac{\delta}{\pi}\right) + \frac{1}{2}\left(\frac{\rho U ld}{m}\right) C_{D_0}\right]\dot{y} + \left[\omega_0^2 - \frac{1}{2}\left(\frac{\rho U^2 ld}{m}\right)\left(\frac{\partial C_L}{\partial y}\right) e^{-i\omega\Delta t}\right] y = 0 \tag{2.8}$$

where ω_0 is the natural frequency (radians) of the cylinder and δ is the logarithmic decrement.

Introducing the time delay term $\Delta t = \mu d/U$ [1], the fluid damping term is now found to be proportional to

$$\left[\left(\frac{\delta}{\pi}\right)\omega_0\omega + \frac{1}{2}\left(\frac{\rho U ld}{m}\right)\omega C_{D_0} + \frac{1}{2}\left(\frac{\rho U^2 ld}{m}\right)\left(\frac{\partial C_L}{\partial y}\right) sin\left(\frac{\mu\omega d}{U}\right)\right] \tag{2.9}$$

If the fluid damping becomes negative, tube oscillations will be amplified. Hence, fluid damping controlled instability occurs.
At the stability threshold $U = U_c$, fluid damping is equal to zero and if $\mu\omega d/U$ is small, the following expression is formed

$$\frac{U_c}{f_0 d} = \left[\frac{4}{-C_{D_0} - \mu d(\partial C_L/\partial y)}\right]\frac{m\delta}{\rho d^2} \tag{2.10}$$

Fluidelastic instability will occur if

$$-C_{D_0} - \mu d(\partial C_L/\partial y) > 0 \tag{2.11}$$

C_{D_0} is generally greater than zero. This implies that instability will only arise if $\partial C_L/\partial y$ is sufficiently large and negative. It is also clear that if there was no time delay, fluidelastic instability would not occur which is in agreement with the literature.

2.4.3 Models

The models discussed in this section use some form of a time delay between tube motion and the resulting fluid forces to be included in their models. This section was not intended to be a compendium of available theoretical models. A comprehensive review of the available theoretical models was conducted by Price [71].

Two earlier models that included a time delay are those of Lever & Weaver [78, 85] and Price & Paidoussis [1]. However, the different authors did not use the same physical arguments to justify the time delay. Both models simulated fluidelastic instability for a single flexible tube vibrating in the lift direction within an otherwise rigid tube array subject to cross-flow. The justification for the use of a single flexible cylinder in an array of rigid cylinders was based on the experiments of Lever & Weaver [78] [2].

Lever & Weavers model does not require static fluid force coefficient data to be measured. Instead, assumptions are made regarding the flow around a single flexible cylinder. The flow is represented by one dimensional and inviscid flow channel

[2]They reported that the essential features of fluidelastic instability in a tube array may be investigated using a single flexible tube in an otherwise fixed array. This was valid for low mass damping parameter and in such cases one flexible cylinder will go unstable at approximately the same velocity as an array of flexible cylinders. They postulated that the motion of the neighbouring tubes was not fundamental to the underlying mechanism which produces the instability. They also reported that a small change in the natural frequency of adjacent tubes in an array can have significant effects on the fluidelastic stability threshold.

streamtubes either side of the cylinder. The form of the streamtube was determined from experimental observation and was fixed for each array geometry. The unsteady fluid forces are caused by a change in the streamtube area as the cylinder vibrates. For attached flow the redistribution in streamtube area is in-phase with the cylinder motion. However, the flow downstream of the cylinder lags behind the cylinder because of fluid inertia, producing a phase-lag between the cylinder motion and the resulting pressure forces on the cylinder. Flow visualisation presented by Abd-Rabbo & Weaver' [35] support the hypothesis of flow redistribution caused by fluid inertia behind the cylinder as the cause of the time delay. Andjelic *et al.* [86] showed that qualitative agreement of the Lever & Weaver model with experimental data was reasonable but the quantitative agreement was poor. Andjelic *et al.* showed that the poor agreement was related to the time delay as modifying it resulted in better agreement. They also suggested the theory requires modification so that it can be used in closely packed normal triangular tube arrays and supported their findings with flow visualisation images. Yetisir & Weaver [87] modified the Lever & Weaver model introducing a decay function in the area perturbation. The introduction of the decay function was considered to be an improvement in the ability of the model to represent the underlying mechanisms of fluidelastic instability, caused a deterioration in agreement between the theory and experiments. They also agreed with the findings of Andjelic *et al.* reiterating the importance of the time delay and the poor agreement of the model for complex geometry. Rzentkowski & Lever [32] utilised the non-linearised one dimensional flow equations from the Lever & Weaver model and noted that the formulation of a new theory for a more rigorous treatment of the underlying fluid dynamics was beyond the scope of their study. Hence, the validity of such a model is questionable especially for more complex geometries where one dimensional flow is unreasonable.

Price & Paidoussis [1] in contrast makes use of a quasi-steady analysis with a frequency dependent term. The fluid forces (lift and drag) are assumed to be identical to those measured with the tube at rest in the same location. Although the analysis was quasi-steady, the resulting fluid damping and stiffness matrices contain frequency dependent terms resulting from the introduction of a time delay effect. In their previous study [88] the frequency dependent term was obtained by following a similar

approach to Den Hartog's for his analysis of galloping instability of overhead power transmission lines. The derivation of the frequency dependent term was not strictly correct and the authors now favoured a different approach. The formulation of the time delay was based on the work of Simpson & Fowler [89]. The origin of the time delay was twofold. Firstly, there was a time delay between the fluid particles leaving an upstream row of cylinders and arriving at a downstream row cylinders. Secondly, a flow retardation effect as the flow approaches the cylinder. Because the flow slows down as it approaches the cylinder, the resulting fluid flow arrives at the cylinder at some interval of time later than it would have done had the flow velocity been constant.

Quantitative agreement between the model and experimental data was poor, underestimating the experimental results by approximately 50% but qualitative agreement was better with the shape of the curves for critical velocity showing better agreement.

Both Lever & Weaver and Price & Paidoussis' analysis observed multiple stability regions. It is doubtful that they will occur in practice due to non-linear effects and this would be in agreement with the literature in general. However, careful experiments by Chen & Jendrzejczyk [90] (tube row), Andjelic *et al.* [86] and Parrondo *et al.* [91] have shown multiple stability boundaries exist. More recently Paidoussis *et al.* [92] questioned the existence of multiple stability regions. Their argument was only in "highly specialised and precisely controlled experiments" could multiple instability regions occur like the experimental studies cited above. It was concluded that multiple boundaries can exist but in reality they are extremely rare. So, the general consensus is that the lowest critical velocity should be used, since once the tube goes unstable it will remain so due to non-linearities.

Granger & Paidoussis [82] proposed an improvement to quasi-steady analysis utilising the concept of a memory effect (time delay function) in the flow rather than a constant time lag used in previous models. When compared to experimental data the model proved to be an improvement on the earlier models. This was not surprising as the model required more experimentally determined coefficients. However, the formulation of the time delay between structural motion and the fluid force was quite interesting. The memory effect was as a result of the change in velocity of the cylinder. This change generates a thin layer of vortices on the cylinder surface, diffused to the

boundary layer and convected downstream by the mean flow. This process leads to an unsteady perturbation in the velocity and the pressure fields in the region around the cylinder, which decays continuously with time as the vortices are convected downstream. Eventually a new steady state is reached when motion-induced vorticity has been transported sufficiently far from the cylinder, so that its influence on the pressure at the cylinder surface becomes negligible. The resulting transient lift coefficient was similar to that obtained by Wagner (*Wagner Function*) using unsteady aerodynamic theory for aerofoils. However, the apparent success of the model does not give any better indication to the underlying mechanisms in fluidelastic instability. Meskell [93] used the hypothesis proposed by Granger & Paidoussis [82] that damping controlled fluidelastic instability was due to the generation and convection of vorticity. A simple wake model was used as the basis of the work combined with the memory function proposed by Granger & Paidoussis [82]. The distinct difference was that Meskell [93] determined the memory function without empirical data and in doing so strengthened the case for vorticity transport as the primary mechanism for damping controlled fluidelastic instability. Today, Granger & Paidoussis' work is widely accepted as the most comprehensive justification for the inclusion of a time delay (memory effect) to-date. However, this is merely conjectural as the time delay associated with fluidelastic instability has yet to be measured directly.

2.4.4 Forces

It is clear from the previous sections that the key to obtaining good simulations of the vibrational behaviour of cylinder arrays lies in the ability to predict the unsteady fluid forces related to the tube motion.

There are two methods used to measure motion dependent fluid forces: the direct and indirect method. The indirect method calculates the forces from measured tube responses such as accelerations and displacements as the calculation of fluid force coefficients directly is difficult. Granger *et al.* [80] used an indirect method to obtain the fluidelastic forces. Using a time domain signal processing method developed in Granger [94], fluidelastic forces are derived from the estimated modal characteristics of the fluid-structure system from structural response data without any excitation

measurement. Meskell & Fitzpatrick [10] used a similar approach, the main differences being the post processing and the range of the recorded amplitude response. The former measured small perturbations from the equilibrium position, while the latter used large vibration amplitude not close to the equilibrium position.

Several researchers have measured the motion dependent fluid forces directly. Teh & Goyder [95] measured fluid forces on a single flexible cylinder which was free to oscillate in the lift or drag direction in a rigid tube array. These fluid forces were related to the oscillating tube only; therefore, they can be used for fluid damping controlled instability only. Chen *et al.* [96] measured all fluid force coefficients in a tube row. In earlier studies only a portion of motion dependent fluid forces were measured. For a long time the most extensive measurements of motion dependent fluid forces were by Tanaka & Takahara [76], and Tanaka *et al.* [97], who measured motion-dependent fluid forces for tube rows and square arrays with pitch ratios of 1.33 and 1.42. More recently, Chen & Srikantiah [83] experimentally measured fluid forces for a tube row with P/d=1.35, normal triangular array with P/d=1.5 and two in-line arrays with P/d=1.42 and 1.46. Motion dependent fluid forces are measured directly and the method was based on unsteady flow theory. Forces were measured on a minimum of four tubes simultaneously. Added mass, fluid damping and stiffness terms were obtained. Then the response of the tube array could be predicted based on unsteady flow theory.

Measured fluid forces can be used in predictive models. Although it is accepted that an analysis based on the unsteady fluid dynamic forces (for example Tanaka & Takahara [76]) will probably be more accurate than one of a quasi-steady approach. However using such a framework and/or obtaining unsteady fluid forces whilst it gives information on the fluid stiffness and damping, and added mass, it does not elucidate the underlying fluid dynamics in fluidelastic instability. It is generally accepted that a simplified model such as a quasi-steady analysis with fewer empirical inputs is more favourable in the helping to understand the physical origin of the mechanism. Such models as explained above, measure the fluid force coefficients on a static body and used them in a dynamic analysis. Hence, the fluidelastic behaviour of a single flexible cylinder could be characterised by two fluid forces (lift and drag) with all

models assuming that the fluid forces are dependent on the dynamic head. One approach used, that of Price & Paidoussis [1], used a quasi-steady fluidelastic analysis for a single flexible cylinder in a rigid array. Although the analysis was quasi-steady, it includes a frequency dependent term which arises due to flow retardation around the front stagnation region of the cylinder. This model was improved upon by the quasi-unsteady model of Granger & Paidoussis [82] which accounts for the unsteady mechanisms by the inclusion of a memory effect of the flow rather than a fixed time delay. However, the pressure field was the same as that of the quasi-steady analysis and the unsteadiness is due to the flow reorganisation. The model requires the fluid force acting on the cylinder when the tube is displaced. There are two approaches for measuring forces directly. The most common approach utilised is force measurement using load cell type arrangements. The other less common approach is measurement of surface pressure on the cylinder and integrating over the surface of the cylinder to calculate the fluid forces. The former method does not give an indication into the force generation mechanism whereas the latter does.

Achenbach [98], Zdravkovich & Namork [17, 99], Zukauskas [16] are some of the papers in the literature that have measured the surface pressure measurements in staggered arrays. However, the pressure distributions were measured for only a few Reynolds numbers. Although in some of the papers the pressure distribution are presented for a number of rows. Furthermore, to the best of the authors knowledge, there appears to be no comprehensive studies of the pressure field around a statically displaced cylinder within a tube array available. Batham [25] presented a limited study of the pressure distribution around a statically displaced cylinder in an array. The configuration used was a ten row in-line array with pitch ratio of 1.25. It was reported that the first three rows were displaced by 0.25mm which corresponds 0.5% tube displacement and that the pressure distribution "completely changed". However no detailed results were presented. In addition, it was reported the mean pressure distribution around a tube in the seventh row was insensitive to small movements in the tube itself. Zdravkovich & Namork [99] moved the second row of a three row array. This resulted in the geometry changing from a staggered arrangement at one extreme to an in-line arrangement at the other extreme with two intermediate geometries in

between. No data was presented on the displacement of a single cylinder within an otherwise fixed array. There is literature available for the static displacements of cylinders within an array and groups of cylinders where the fluid force coefficients are measured using a load cell e.g. Price & Paidoussis [100]. Romberg & Popp [101] measured the fluid forces (obtained using surface pressure measurements) on a oscillating cylinder in a rigid array. Measurements were also made along the length of the cylinder. No pressure distributions were presented; however, the results presented show when the tube was unstable due to fluid damping controlled instability, the correlation length of the forces acting on the length of the cylinder increases to large values. While there is information on the fluid force coefficients in the literature, there is no indication of the force generation mechanism. Furthermore, there appears to be no comprehensive studies of the pressure field around a statically displaced cylinder within a tube array available. In addition, all models assume that the fluid force coefficients scale proportionally to dynamic head. It is not clear this assumption is correct. Firstly, a cylinder in a tube array is subject to an increased blockage and higher levels of turbulence and it has been reported (for example Zukauskas *et al.* [102]) that the critical conditions occur at lower Reynolds numbers. The wake of the cylinder is also affected as is the position of flow impingement especially in in-line arrays or sparse staggered arrays. Furthermore, Weaver & Fitzpatrick [12] suggest that a more complex relationship between velocity and fluid forces may exist and cite the work of Price *et al.* [13] who reported that turbulence response amplitude increased approximately linearly with flow velocity.

2.4.5 Interaction between Fluidelastic Instability and Vortex Shedding and/or Acoustic Resonance

It has also been reported that the flow induced vibration phenomena can co-exist. However, there are also suggestions that there can be an interaction between the phenomena. A number of papers can be found in the literature where an apparent interaction between fluidelastic instability and vortex shedding may exist. Granger & Paidoussis [82] suggest that the fluid structure phenomenon underling fluidelastic instability for a fully flexible tube array, requires updating. They suggest that for

low mass damping parameter, fluid damping controlled instability should consider the effect of vortex shedding. Results in support of this argument are presented by Granger *et al.* [80]. They reported on a flexibly mounted tube in the front-row (rather than central row tubes) in an in-line array (P/d=1.44), interacting with periodic vortex shedding influencing fluid damping controlled instability resulting in instability occurring prematurely. However, the authors concede that their conclusion was conjectural. Nevertheless, similar findings were reported by Price & Paidoussis [26] who reported on a single flexible cylinder in an in-line array (P/d=1.5) in air. They found that the onset of fluidelastic instability and a Strouhal peak of 0.055 were coincident. The authors hypothesised that the vortex shedding merely triggered FEI to occur at a slightly lower velocity than it would otherwise have done. Furthermore, Price *et al.* [37] observed the flow visualisation of a single flexible tube free to oscillate in the cross flow direction in a parallel triangular array, (P/d =1.375). They suggests that for low mass damping the resulting instability may be a combined fluidelastic instability and vortex shedding, thus supporting Granger & Paidoussis' view on FEI mechanisms. Weaver & Yeung [103] reported on various array types with a pitch ratio of 1.5 with water as the working fluid. For in-line arrays (parallel and square) vorticity resonance occurred simultaneously with fluidelastic instability. The coincidence had the effect of obscuring the critical velocity. However, the authors do not make reference to an interaction between the phenomena, rather a simultaneous occurrence which merely made separation difficult. In these studies, the vortex shedding frequency and the structural natural frequency are comparable. Thus, resonance with a flow periodicity and FEI may sometimes occur almost coincidentally (i.e. at the same onset flow velocity). In this situation, it is not clear whether the two vibration excitation mechanisms remain distinct or if there is an interaction between the two phenomena.

In addition to the interaction between fluidelastic instability and vortex shedding, an apparent interaction between fluidelastic instability and acoustic resonance has also been reported. As discussed above, as the array of cylinders is enclosed within a duct, the system may also experience acoustic resonance in addition to fluidelastic instability, the frequency of which may be several orders of magnitude greater than the fundamental frequency of the structure. Thus, it might be expected that these

two phenomena would be independent. This perspective has been widely accepted in relation to the interaction between fluidelastic instability and acoustic resonance as there is such a large separation in the frequency of the phenomena. However, Price & Zahn [3] reported on the fluidelastic behaviour of a single flexible tube in a normal triangular tube array with pitch ratio of 1.375 in air. The flexible tube was free to oscillate in both the lift and drag directions. They reported an interaction between fluidelastic instability ($\sim 7Hz$) and acoustic resonance ($733Hz$). When the flexible tube was mounted in the first row, fluidelastic instability was apparently triggered by acoustic resonance. The acoustic resonance was also noted to have organised the flow throughout the tube array. The authors also note that acoustic resonance sometimes had a minor effect on the cylinder vibration amplitude. When the flexible tube was positioned in rows 2-7, there was typically a change in the vibration amplitude coincident with acoustic resonance. More recently, Meskell & Fitzpatrick [10] reported on the fluidelastic behaviour of a centrally located tube with a natural frequency of 6.6Hz in a normal triangular tube array with pitch ratio of 1.32. The flexible tube was free to oscillate in the lift direction only. They reported that fluidelastic instability was suppressed when the free stream flow velocity reached 9m/s. This was accompanied by an acoustic resonance at 1050Hz corresponding to the second transverse mode of the duct. It is not clear how these two phenomena with this large separation in frequency could interact. It is possible that the acoustic resonance is interfering with the time delay mechanism associated with fluidelastic instability. Granger & Paidoussis [82] described a memory effect (cause of the time delay) due to the diffusion-convection of vorticity from the surface of the cylinder. It is possible that acoustic resonance could interact with this process modifying the time delay mechanism, hence the fluidelastic vibration amplitude. At present this hypothesis is merely conjectural as in both articles [3, 10] where an apparent interaction between fluidelastic instability and acoustic resonance was observed the authors note that the coupling mechanism was uncertain and further work was necessary.

2.5 Summary

There has been much work on the subject of flow induced vibrations in tube arrays. This results from the potentially catastrophic effect it can have on heat exchangers in power generation and process applications. It is also recognised that there are four flow induced vibration mechanisms. Turbulent buffeting is reasonably well understood but some questions remain regarding the relationship between amplitude response and flow velocity. Likewise, vortex shedding and acoustic resonance are reasonably well understood. Much research has been focused on the development of Strouhal number charts for vortex shedding. It was found that excitation source of vortex shedding was dependent on the array configuration. Furthermore, the array pitch was also an important parameter in the Strouhal number charts, with different curves for small, intermediate and large array pitches for some array geometries. The acoustic excitation mechanism, was shown to be related to naturally occurring flow periodicities in normal triangular and rotated square arrays. This was not the case for normal square and parallel triangular arrays. A number of damping criteria for the occurrence of acoustic resonance and methods for suppression of acoustic resonance are also available in the literature.

Fluidelastic instability is not so well understood. As a result, design guidelines tend to be overly conservative, this is partly due to the scatter in the data and the doubt as to what parameters to use. While there is still considerable uncertainty, much progress has been made. For instance, the identification of two type of mechanisms; fluid damping and stiffness controlled instability. The former, requires only a single degree of freedom, while the latter requires multiple degrees of freedom. Stiffness controlled instability overcomes structural damping of the coupled modes by means of fluid coupling between adjacent cylinders whereas damping controlled instability results from negative fluid damping. Some evidence also exists that there is a time delay between tube displacement and the resulting fluid forces. However, this time delay has yet to be measured directly. In addition, predication of fluid forces is difficult but a number of models have been employed to predict the onset of fluidelastic instability, which formulate a better understanding of the underlying mechanism. The empirical

input to these models varies but all models assume that fluid forces scale with dynamic head. However, the validity of this assumption is not clear. Hence, there is a need for some rudimentary experimental data (surface pressure and force measurements) for validation of models and some of the assumptions made in those models.

It is also unclear as to whether the phenomenon of fluidelastic instability can interact with vortex shedding and acoustic resonance. Some evidence exists that there may be an apparent interaction between vortex shedding and fluidelastic instability. In this case the frequencies of the phenomena are similar and therefore is reasonable to suggest that an interaction my occur. However, an apparent interaction between acoustic resonance and fluidelastic instability has also been reported. In this case the frequencies of the two phenomena are very distinct with over two orders of magnitude difference. It is therefore difficult to comprehend the interaction. Nonetheless, the apparent interaction has been reported but this has not been verified and the nature of the interaction is uncertain.

Chapter 3

Experimental Facility and Instrumentation

This chapter describes the experimental facility and the measurement techniques employed in this investigation. An explanation of the experimental facility and its constituent parts, as well as the instrumentation and the calibration processes associated are discussed. Finally, the data acquisition will be described.

3.1 Experimental Facility

The experimental facility consists of a wind tunnel with the tube array under investigation installed in the test section. All tubes in the array are rigid except for one which will be referred to as the instrumented tube. For the vibration tests, the instrumented tube was flexibly mounted and free to oscillate in one direction only. Vibration was monitored using an accelerometer. For the force measurement tests, the instrumented tube has thirty six pressure taps at the mid-span around the circumference of the cylinder. The cylinder can be statically displaced in the both the lift and drag directions. Two speakers mounted on the side walls of the test section were used to artificially excite acoustic resonance.

3.1.1 Wind Tunnel

The wind tunnel used in this investigation was an open loop draw down wind tunnel with air as the working fluid. The wind tunnel was 6.2m long and consists of a number of sections; intake, diffuser, fan/motor and the test section. These will be discussed

below. The wind tunnel was already present in the lab and its design and construction followed well established guidelines. For more details on the design criteria see Meskell [104]. A schematic of the wind tunnel is shown in Fig. 3.1.

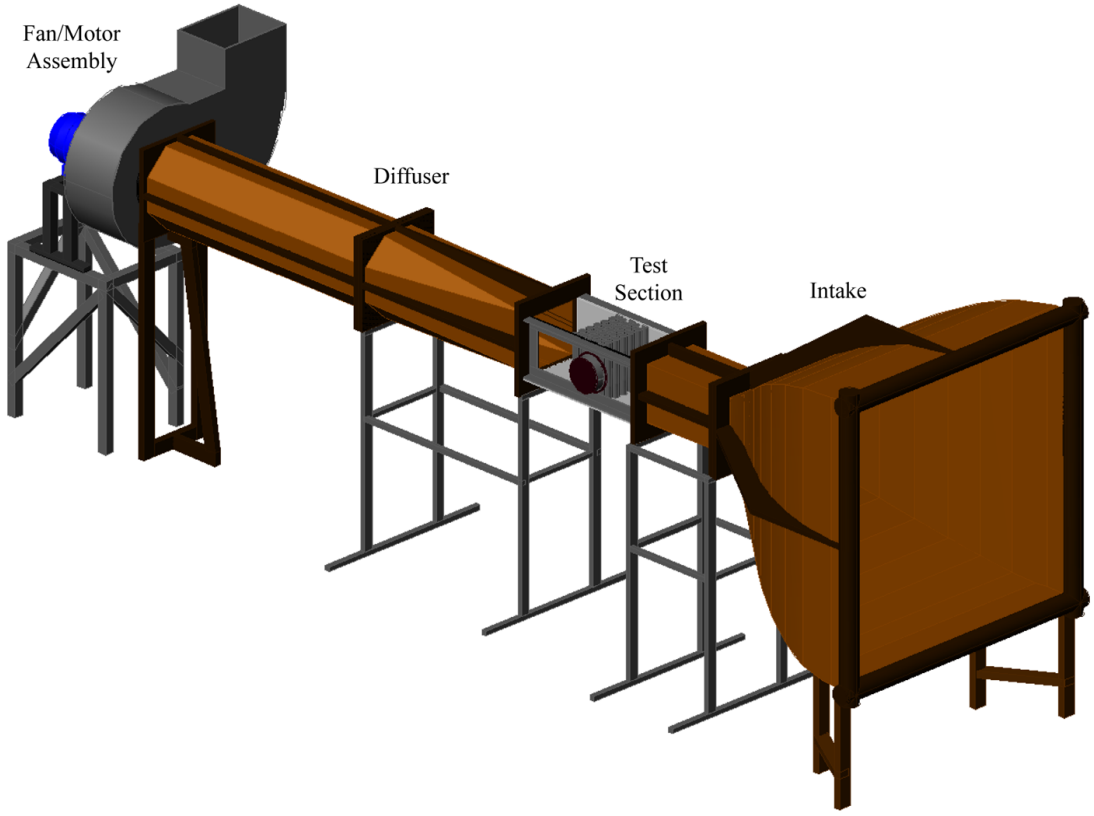

Figure 3.1: Wind Tunnel Schematic

The intake opening was 1500mm square, contracting down to a working section of 300mm square using a contraction ratio of 25:1. This ensured low flow velocities at the inlet and good turbulence characteristics in the test section. The intake is connected to the test section discussed below. The diffuser section is connected to the other end of the test section and was constructed in two parts. The first section provided a transition from a square cross section of the test section to an octagonal cross section. The second section is a straight octagonal duct. A flexible plastic seal connects the diffuser section to circular inlet of the fan. The flexible seal eliminates a possible transmission path for vibrations from the fan/motor assembly to the test section.

The flow in the wind tunnel was provided by a Chemsys centrifugal fan driven by a WEG 7.5kW three phase AC motor. An Allen-Bradley Power Flex 40 AC speed controller controls the motor speed by changing the nominal operating frequency of 50Hz. The frequency ranged from 5-50Hz depending on the load on the motor. A frequency resolution of 0.01Hz can be achieved, facilitating accurate control of motor and hence, the flow velocity. The flow velocity measured in the test section with no blockage ranged from 2.5m/s to 30m/s. The advantage of controlling the flow velocity using the speed controller over that of a baffle plate at the exhaust of the fan was smooth non pulsating flow for the whole range of velocities tested.

The test section dimensions are 300mm $\times$ 300mm cross section with a length of 750mm. A photograph and a schematic of the test section are shown in Fig. 3.2. The test section consists of an exterior frame made of 50mm aluminium angle. This frame supports the walls of the test section which are made from 10mm thick Perspex thus enabling optical access. The top and bottom of the test section are removable. Hence, this setup facilitates various tube array configurations to be tested. For each array configuration ϕ38mm diameter holes were milled from perspex plates to locate the rigid tubes in the correct position. Three tube arrays were investigated in this study. The configurations under test were three five row normal triangular arrays with pitch ratios of; 1.32, 1.58 and 1.97.

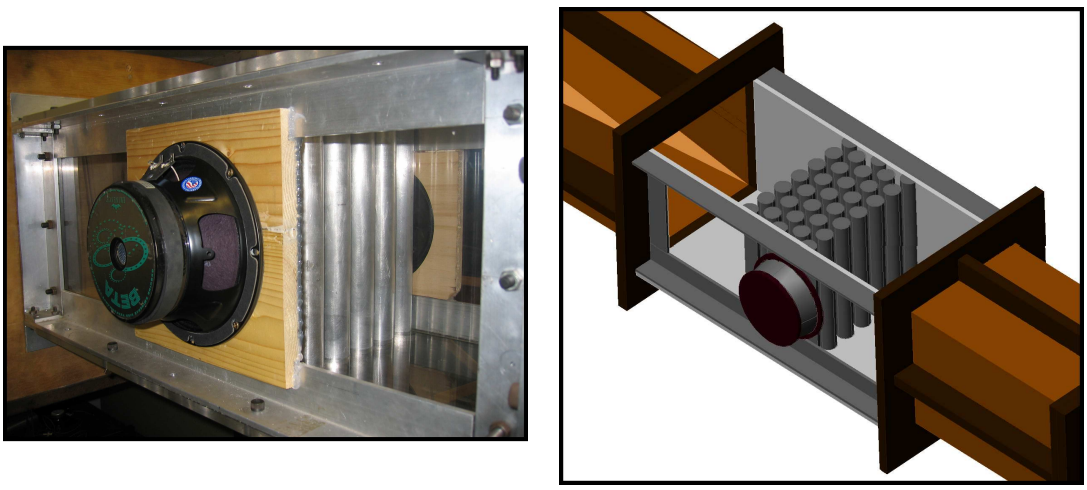

Figure 3.2: Test Section

The tubes in the array are constructed of ϕ38mm diameter aluminium and are 310mm in length. The tubes are fixed vertically to the floor and ceiling of the wind tunnel by clamping an o-ring with the end of the tube and a washer. This compresses the o-ring which grips the perspex securely as illustrated in Fig. 3.3. In addition, the set up is such that any of the rigid cylinders can be replaced with an instrumented cylinder at any position in the array.

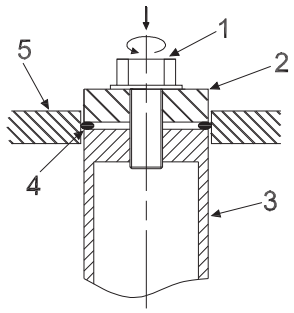

No.	Description
1	Locking Bolt
2	Washer
3	Rigid Tube
4	Rubber O-ring
5	Test Section Ceiling

Figure 3.3: Tube Clamping

3.1.2 Instrumented Cylinder

In this study, both tube vibration measurements and surface pressure measurements were made with and without acoustic excitation in the duct. This was achieved by replacing one of the rigid cylinders in the array with an instrumented cylinder. There where two different instrumented cylinders used in this study to satisfy the testing criteria. These will be discussed in greater detail in the following paragraphs.

3.1.2.1 Flexible Cylinder

The fluidelastic behaviour was characterised using the instrumented cylinder which was *flexibly mounted* as fluidelastic forces on a static body do not exist. *Flexibly mounted* refers to the tube being rigid in construction. However, the tube was mounted on a flexible cantilevered support outside and isolated from the wind tunnel, consisting of two aluminium beams (3mm $\times$ 50mm $\times$ 500mm) 80mm apart in a parallel configuration (see Fig. 3.4). This arrangement is different to many of the studies found in the literature which uses piano wires. The reason for the cantilever setup was to facilitate

vibration in one direction only. Two beams were used to prevent torsional effects. A sketch illustrating the top of the mounting scheme for the flexible tube can be seen in Fig. 3.5. Also shown is the accelerometer mounted on the tube support which was used to measure the tube oscillation.

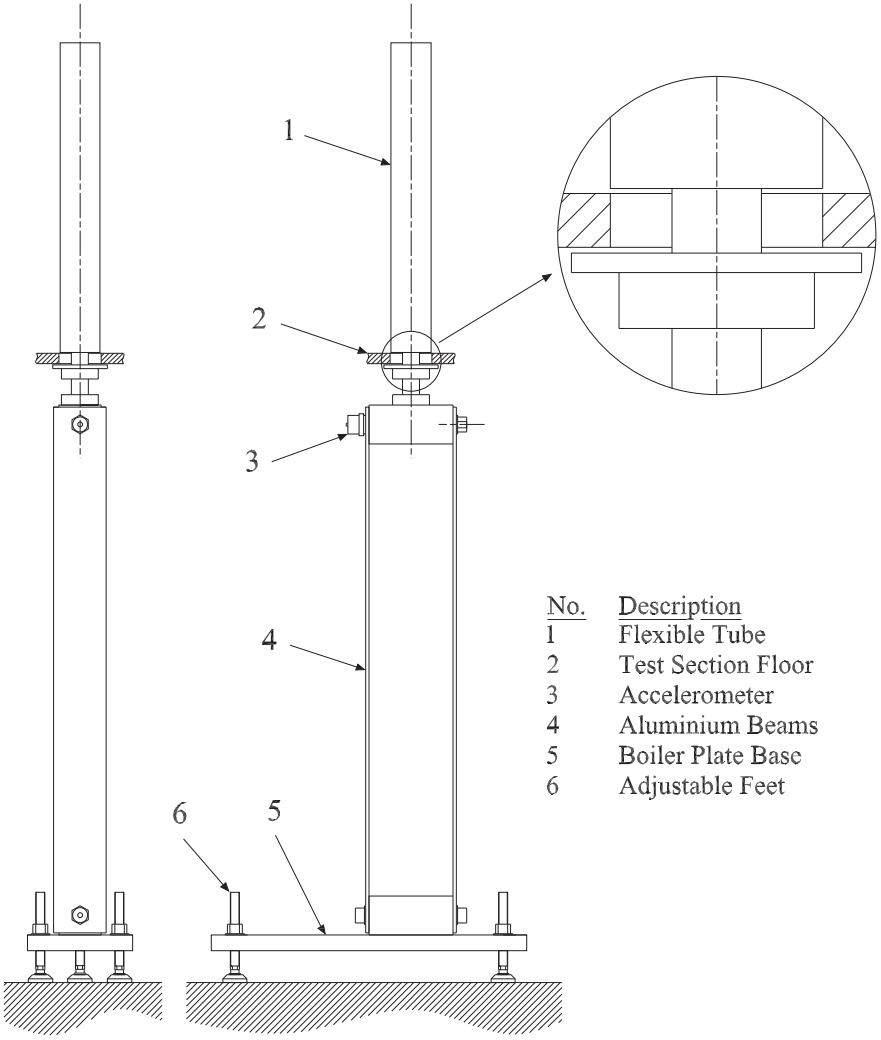

Figure 3.4: Flexibly Mounted Tube & Support

The structural viscous damping was controlled by a simple non contact electromagnetic damper (EMD) shown in Figs. 3.5 and 3.6. The device consists of a coil, a permanent magnet and a range of variable resistors. The coil was attached to the flexibly mounted tube twin beam support as illustrated and sits in a narrow annular gap between the pole caps of the permanent magnetic (similar to a speaker). The coil was connected to a variable resistor to make a closed system. The level of damping

was set by modifying the resistance in the circuit. The advantage of this setup was that there was no mechanical connection between the magnet and the coil so there was no change in structural stiffness, [104].

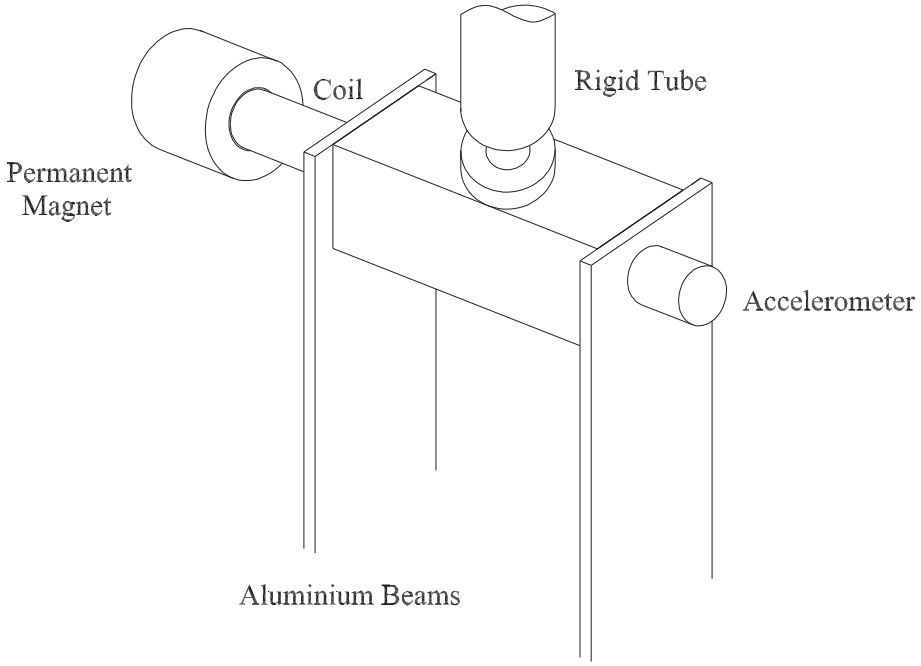

Figure 3.5: Flexibly Mounted Tube with EMD

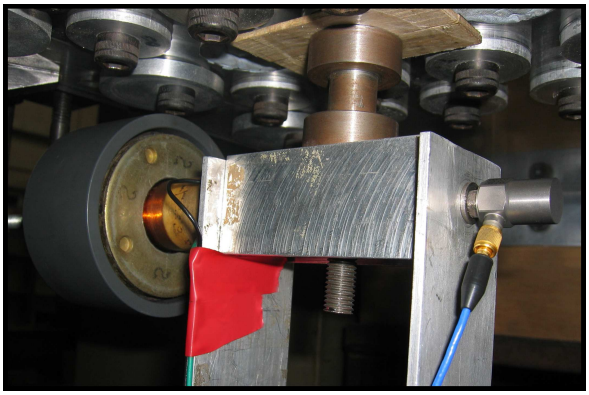

Figure 3.6: Electromagnetic damper in situ

The electromagnetic damper system was also used as electromagnetic shaker (EMS) by applying a voltage across the coil. The resulting electrical current reacts with the steady magnetic field to provide a force on the structure. This force is approximately proportional to the instantaneous current in the coil. This excitation mechanism was used in the forced vibration tests.

3.1.2.2 Pressure Tapped Tube

In order to investigate the fluid forces on a rigid cylinder, an instrumented tube with 36 surface pressure taps with a diameter of 1mm and circumferentially space (i.e. not along the tube axis) at 10^o intervals located along the center span of the tube was constructed.

The center of the cylinder where the pressure taps are located was constructed from solid brass. Holes ϕ1.59mm were drilled to a depth of 20mm. Thirty six equispaced holes at 10^o intervals were then drilled around the circumference. The holes were ϕ1mm and drilled in the direction towards the origin (center - axial direction) until the ϕ1.59mm holes drilled in axial direction were reached. A ϕ1.59mm outer diameter brass tubing was fit into the axially drilled holes and air tightness was secured by brazing the connection. Two hollow brass tubes were fitted either side of the machined block. A solid cap and base were push fit. Photographs of the various assembly stages can be seen in Fig. 3.7. Schematics of the pressure tapped tube are contained in Appendix B. The base extended outside of the wind tunnel where it was clamped. The length of the cylinder assembly within the test section was 299mm with a diameter of ϕ38mm. Beyond that the diameter was reduced to facilitate static displacement of the cylinder with the otherwise rigid array. The cylinder was mounted on a bidirectional traverse located outside the wind tunnel. Each pressure tapping was monitored with a Senotec 24 PC Series differential pressure transducer with the reference vented to atmosphere. In effect the gauge pressure was measured. The instrumented tube was connected to the pressure transducers with short lengths of 2mm internal diameter silicon tubing.

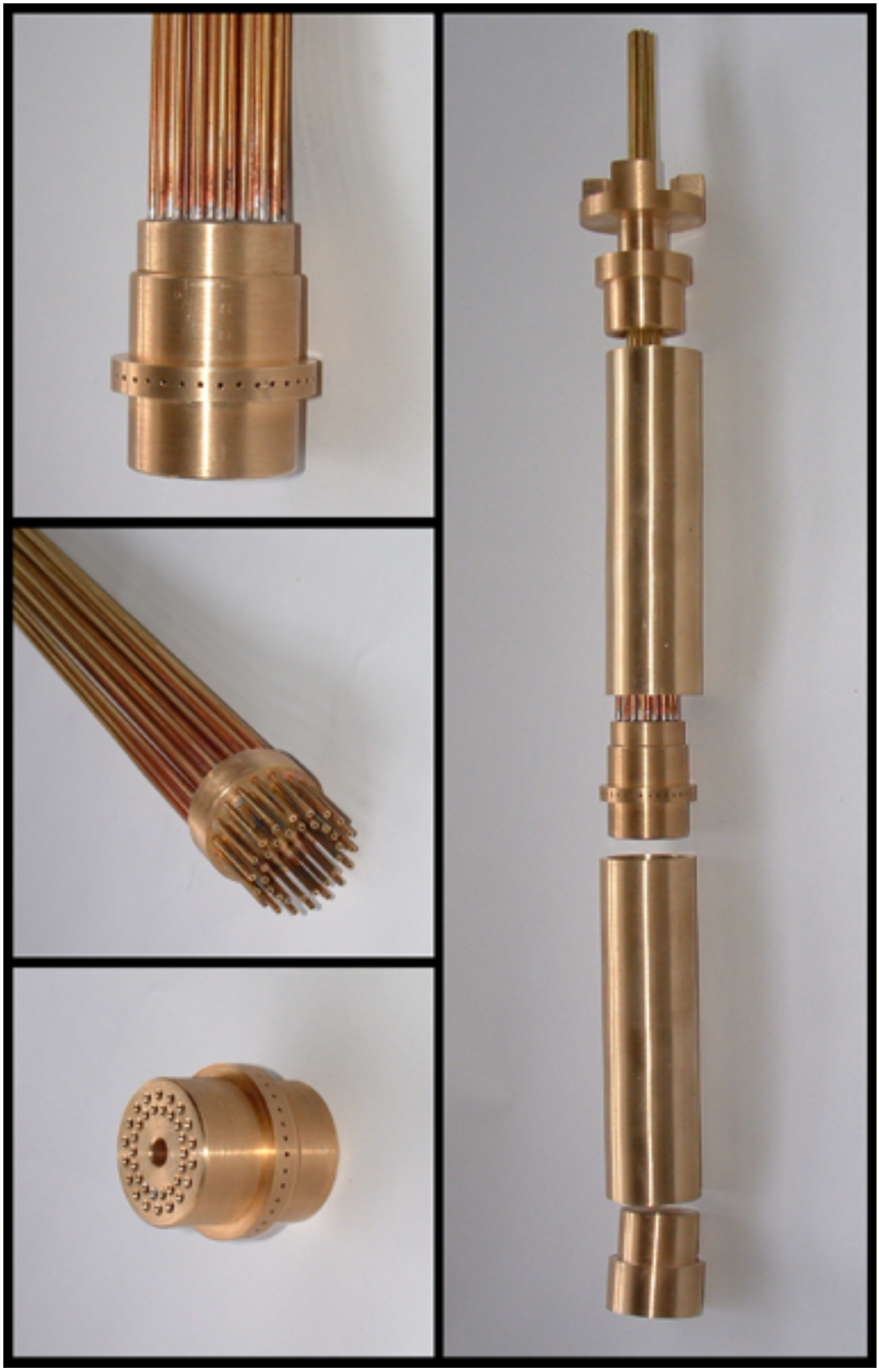

Figure 3.7: Photograph of the Pressure Tapped Tube

3.1.3 Acoustic Excitation

Artificial excitation of acoustic resonance in the tube array was achieved using two 225W speakers (Eminence Beta 8) located on both side walls of the test section as shown in Fig. 3.2. Welsh *et al.* [68] reported that the positioning of the speakers was important as the magnitude falls off exponentially upstream and downstream of the source. A finite element analysis of the tube array was conducted to identify the nodes and anti-nodes of the acoustic modes and hence establish the optimal position of the speakers (Appendix C). Furthermore, Kacker & Hill [65] reported of the importance of a break in continuity of the wall through which sound may be introduced in establishing a standing acoustic wave in a wind tunnel using an external sound source. The wind tunnel walls were modified with the insertion of ϕ6mm diameter holes. The speakers were driven by a HP35665A dynamic signal analyzer via USA 370 amplifier. To excite the first acoustic mode, the speakers were wired in phase and excited at a frequency of 592Hz. To excite the second acoustic mode the speakers were wired in anti-phase and excited at a frequency of 1092Hz (P/d=1.32).

3.2 Instrumentation

Pressure measurements (both steady and fluctuating), vibration amplitude as well as flow velocity measurements were conducted in this study. The instruments used to measure these quantities are described below. The error of uncertainty in the measurement techniques is discussed in Appendix D

3.2.1 Accelerometer

An accelerometer was mounted to the twin beam structure to measure the acceleration response of the flexibly mounted cylinder. Acceleration was measured using PCB quartz shear accelerometer (PCB 353B03) with a useful range of $0.2 - 7000Hz$ (based on a maximum 5% variation in sensitivity) with no external charge amplifier required as it was built in. The accelerometer was powered using a PCB power supply (PCB 441A101) and a sensor signal conditioner (PCB 441B104) both of which were contained in a two slot chassis (PCB 441A42). The calibration of the accelerometer was taken from the calibration data card that was issued by manufacturer with the accelerometer and this was verified with a single frequency calibration using a *Brüel* and Kj*a*er exciter Type 4294.

3.2.2 Microphones

The sound pressure level (SPL) was measured using G.R.A.S Type 40BH $\frac{1}{4}$ High Pressure Microphones with a SPL upper limit of 194dB with 3 percent distortion. The microphones were connected to a Preamplifier Type 26AC via a Power module Type 12AN (both G.R.A.S) and used to make sound pressure measurements on the wind tunnel walls (as the acoustic pressure was a maximum at this position).

Four microphones were used in this study. Since phase and magnitude information were important in this case, it was important to measure the transfer function between a reference microphone and the other microphones to quantify the differences in magnitude and phase sensitivity.

Calibration was achieved using the concept that in a cylindrical duct plane waves propagate below a certain cut-off frequency (Eqn. 3.1). If two microphones are lo-

cated in the same plane along the duct they are exposed to the same pressure wave distribution for frequencies below the cut-off frequency.

$$f_{cut-off} = \frac{1.84 c_{sp}}{2\pi a} \simeq 4kHz \tag{3.1}$$

where c_{sp} is the speed of sound and a is radius of the duct. The duct used for calibration had a cut-off frequency of ∼4kHz. A calibration transfer function between the microphones was obtained. This transfer function was then incorporated in the data processing stage. The sensitivity of the microphones was obtained using a *Brüel* and Kj*ae*r Sound Level Calibrator Type 4231 at a frequency of 1000Hz and pressure of 1Pa (94dB).

3.2.3 Pressure Transducers

The pressure transducers are differential pressure transducers (Senotec 24 PC Series) with one of the ports vented to atmosphere. In effect the gauge pressure was measured. The pressure transducers are based on a four active element piezo resistive bridge construction. An input voltage was supplied and when a change in pressure occurs, a change in the output voltage results. Using a conversion factor, the pressure can be determined from the output voltage signal. The amplitude of the signal was small and was of the order of millivolts. Hence, the signal was susceptible to noise. This was an issue when supplying the operating voltage of 10V. A mains DC supply would be ideal. However, even very expensive sources contain 50Hz noise and as the measurement is of the order of millivolts, the 50Hz noise swamps the output voltage signal. The other alternative was a real DC source like a battery. This would only be susceptible to radiated noise. The drawback with the battery was that the supply voltage changes over time and when current was drawn (when a pressure was applied). These effects would result in a change in pressure transducer response to a given applied pressure. The solution chosen was to use a voltage regulator circuit. Figure 3.8 shows a schematic of the circuit used. It consists of a voltage regulator IC, input and output terminals and two capacitors. The capacitors are employed to decouple the applied voltage to the pressure transducer and are positioned before and after the voltage regulator IC. This arrangement was supplied by a voltage in the range 12-24V to produce a

constant voltage of 10V to supply the pressure transducer. The outputs from the pressure transducers are connected to a BNC terminal. The components are mounted on a printed circuit board. Twelve pressure transducers are housed in a metal casing to shield the instrumentation from external noise sources. The casing was grounded with respect to the data acquisition ground. Holes were drilled in the casing to allow one port of the transducer to connect to the instrumented cylinder using a short length of silicon tubing. Note all pressure transducers have individual power sources to prevent cross talk between the measured signals.

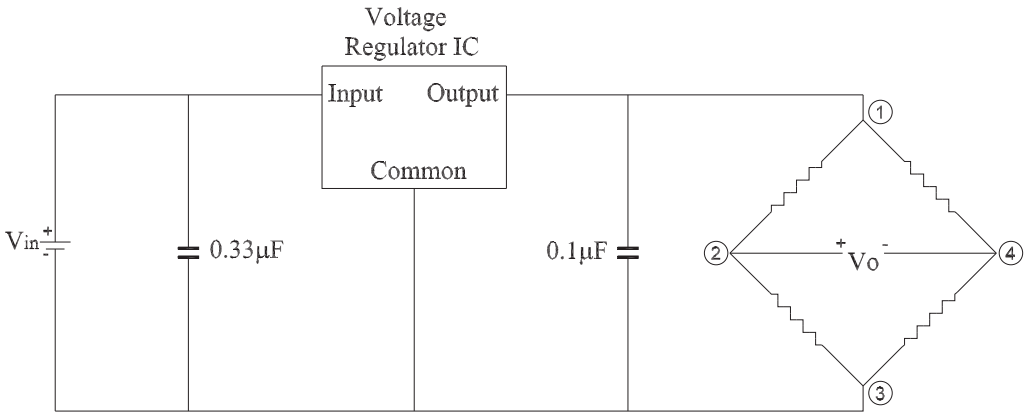

Figure 3.8: Voltage Regulator Circuit

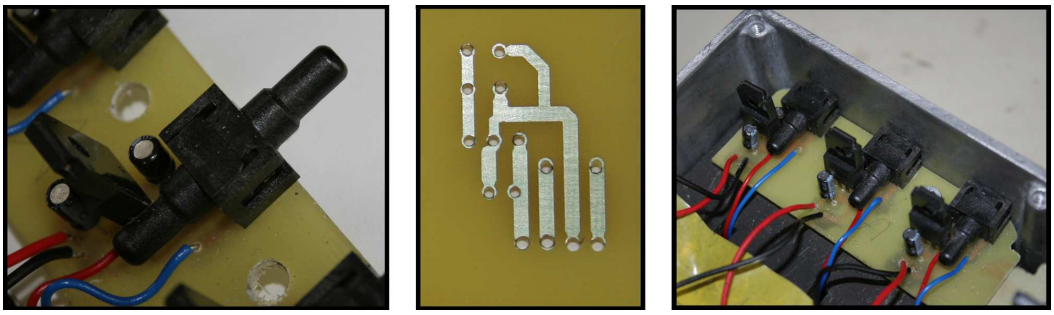

Figure 3.9: Pressure Transducer and Voltage Regulating Circuitry

The signal from the pressure transducer was acquired at a sample frequency of 64Hz and the signal was averaged to give a mean value. From the viewpoint of calibration, as no dynamic measurements or high frequency sample rates were used only a simple calibration procedure was necessary. A known force was applied to a pressure transducer (will now be referred to as the reference pressure transducer). From this, the

sensitivity of the pressure transducer was obtained, hence, a relationship between the output voltage from the pressure transducer at a known pressure. The other pressure transducers were then calibrated with respect to the reference pressure transducer.

3.2.4 Flow Velocity Measurement

Two approaches were employed to measure flow velocity. A pitôt-static was used to calculate the free stream flow velocity, while local flow velocity measurements in the tube array were conducted using hot-wire anemometry.

3.2.4.1 Pitôt-static Tube

A pitôt-static tube installed upstream of the tube array connected to a Furness Control micromanometer (model FC015) measured the free stream flow velocity in the test section. For a clean test section the velocity ranged from $2.5m/s$ to $30m/s$. With the installation of the arrays; P/d =1.32, 1.58 and 1.97 the maximum flow velocity reduces to $10m/s$ and $14m/s$ and $18m/s$ respectively, as a result of blockage. The difference in maximum flow velocity associated with the arrays was related to pressure drop and hence the compactness of the arrays. Hence, the more compact array ($P/d = 1.32$) has a lower maximum free stream flow velocity. As discussed above, the flow velocity was controlled by the motor speed controller.

3.2.4.2 Hot-wire Anemometry

Hot-wire anemometry is used to measure fluid flow in gas flows. The hot-wire anemometer used in this setup was a DISA 55M01 system with a 55M10 Constant-Temperature Anemometer standard bridge.

It works on the principle that the probes resistance is proportional to the temperature of the hot-wire. The bridge circuit is shown in Fig. 3.10. Air flowing past the wire has a cooling effect on the wire. The servo amplifier tries to keep the probe resistance constant. This is achieved by modifying the voltage across the wire. Hence, a relationship between voltage across the wire and flow velocity can be obtained. The hot-wire was calibrated by measuring the voltage across the wire, E_{hw}, for a known velocity, u, flowing normal to the wire. This was done for a flow velocity range from

0-42m/s. A third order polynomial curve was fit to the data.

$$u = 2.322E_{hw}^3 - 19.75E_{hw}^2 + 58.12E_{hw} - 58.76 \tag{3.2}$$

Hot-wire anemometers, while extremely delicate, have extremely high frequency-response and fine spatial resolution compared to other measurement methods. However, they are fragile and can only be used in clean gas flows. Also, as the probe is physically in the flow, the method is intrusive.

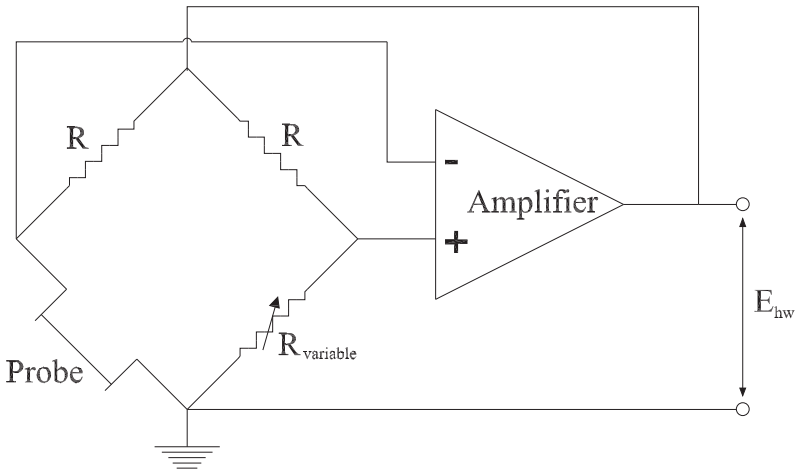

Figure 3.10: Hot-wire Bridge Circuit

3.2.5 Flow Visualisation

A single lens reflex (SLR) camera (Canon EOS 20D) with a 8.2 MP CMOS sensor and a variable focus length lens (24-50mm) was used to capture flow visualisation images. This setup facilitated high resolution images at shutter speeds up to 1/6400 of a second and a maximum of five frames per second. A CCD (Charge Coupled Device) camera was also tried. Although the CCD camera facilitated a higher frame rate, the image resolution was much poorer. The flow was seeded using an Antari Z1000 series fog generator with a typical particle size of 1 to 50μm and the flow was illuminated using a photography 100W modelling lamp with a reflector to disperse the light.

3.3 Data Acquisition

The data was recorded on a National Instruments mainframe (NI PXI-1002) which housed an 8 channel acquisition card (NI PXI-4472B) and an 8 channel analog output card (NI PXI-6713) connected to a (TBX-68) termination accessory. The hardware was connected to a desktop PC via PCI card. The PC controlled the mainframe using LabView software. This system was capable of 8 differential voltage inputs simultaneously sampled using a 24bit analogue to digital conversion (ADC). The system had the ability for AC or DC coupling depending on the measurement type. The hardware had in-built programmable low pass filters to ensure that the anti-aliasing was adhered to. The acquired data was stored on the PC, ready for post processing.

Chapter 4

Effect of Acoustic Resonance on Fluidelastic Instability Quantified

4.1 Fluidelastic Instability

As noted in chapter 2, there are a number of mechanisms which can cause flow induced vibrations in tube arrays. The mechanism with the greatest potential to cause damage is fluidelastic instability. Fluidelastic instability produces large amplitude vibrations at (or close to) the natural frequency of the structure. In this study, unless otherwise stated, the type of fluidelastic instability referred to is fluid damping controlled instability. These large amplitude vibrations occur when a critical flow velocity is exceeded at which point the fluid damping goes negative. Tests were conducted to investigate the fluidelastic instability threshold. The fluidelastic behaviour was characterised using the instrumented cylinder which was *flexibly mounted* as described in chapter 3. Tests were conducted for a cylinder in the third row of three five row normal triangular tube arrays with pitch ratios of 1.32, 1.58 and 1.97. Tests were conducted for three levels of structural damping for the pitch ratios of 1.32 and 1.58 and one level of damping for the pitch ratio of 1.97. As described in section 3.1.2.1 the viscous structural damping was modified by setting the resistance in the electromagnetic damper circuit. For the different array pitches, different values of structural damping were used so that the stability thresholds lay within the wind tunnel velocity range. In general, the level of structural damping used increased with decreasing pitch ratio. Table 4.1 shows the velocity range tested for the respective pitch ratios.

P/d	Velocity, U (m/s) min	max
1.32	2	8.9
1.58	3	13
1.97	4	18

Table 4.1: Velocity range for threshold tests

At each flow velocity the tube was given time to establish a steady motion. Tube acceleration was then measured for 600 seconds at a sample frequency of 64Hz to acquire a steady RMS value of vibration amplitude. With anti-aliasing filters the dynamic range was 0-29Hz. Within this frequency range only the first mode was measured with the higher frequency modes not included. From the tube acceleration data, an estimate of the tube displacement was extracted. Dividing the tube acceleration by the square of the tubes natural frequency in terms of radians yields an estimate of the tube displacement. This approach is valid as the tube was lightly damped, so it can be assumed that the system vibrates close to the natural frequency of the structure. Hence, high levels of vibration at the natural frequency will ensue and the other low magnitude frequency components can be ignored. This was further supported by the fact that the dynamic measurement range was 0-29Hz and within that frequency range there was only one structural mode of 6.6Hz (or 41.47 rad/s).

Figures 4.1, 4.2 and 4.3 show the RMS of non-dimensional tube displacement, y/d, as a function of free stream flow velocity for pitch ratios of 1.32, 1.58 and 1.97, respectively. For P/d=1.32 at low flow velocities, small vibration amplitudes ($y/d < 1\%$) are observed, which can be attributed to turbulent buffeting. As the flow velocity was increased, fluidelastic instability was apparent and was characterised by the rapid increase in vibration amplitude. The change in slope of the vibration amplitude curve has been used as a practical definition of threshold velocity, U_c (e.g. Austermann & Popp [2]). The alternative definition of critical velocity based on amplitude levels (rather than amplitude gradients) proposed by Yeung & Weaver [105] was also satisfied. The critical velocity was shown to be dependent on structural damping similar to reports in the literature. These tests illustrate that fluidelastic instability was present in this tube array at the structural damping levels tested.

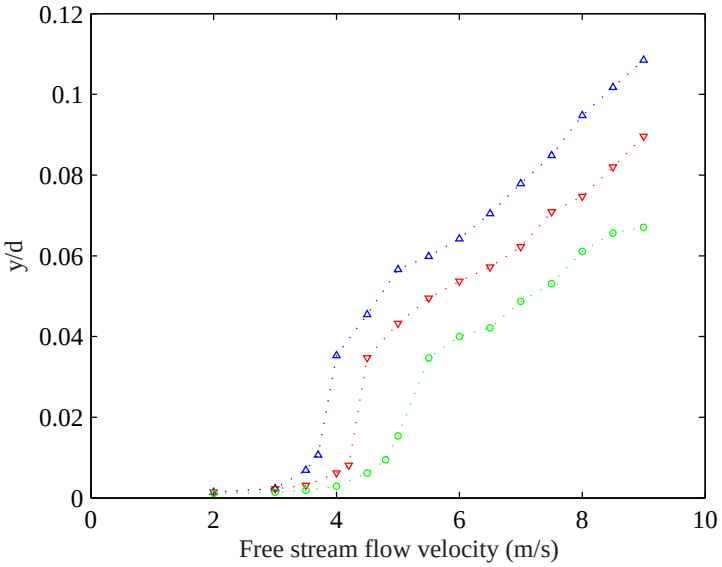

Figure 4.1: P/d=1.32 RMS of tube motion at three levels of structural damping: $\Delta, \delta_{st} = 0.077$; $\nabla, \delta_{st} = 0.098$; $\circ, \delta_{st} = 0.123$

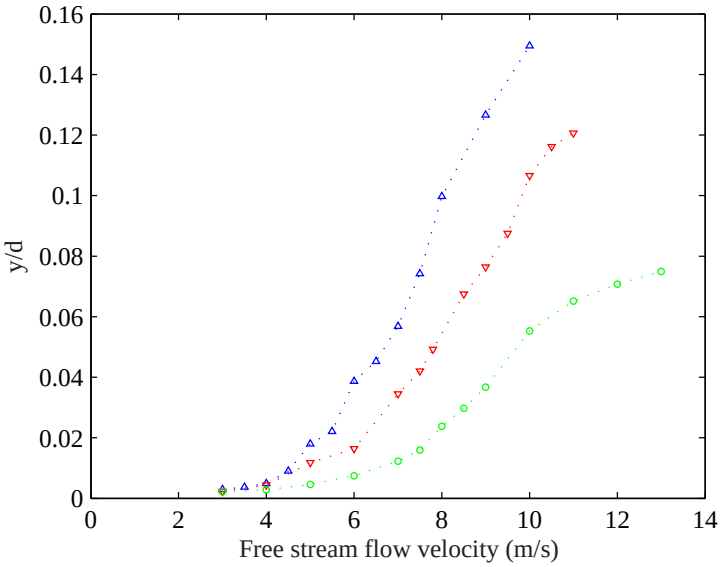

Figure 4.2: P/d=1.58 RMS of tube motion at three levels of structural damping: $\Delta, \delta_{st} = 0.017$; $\nabla, \delta_{st} = 0.023$; $\circ, \delta_{st} = 0.030$

For P/d=1.58 at low velocities the vibration amplitude was small and again attributed turbulent buffeting. In this case, as the flow velocity was increased the change in vibration amplitude was not as rapid as that observed for P/d=1.32. The change was more gradual but nonetheless there was a change in slope. Again, both criteria outlined above for the determination of the critical velocity are satisfied implying

that fluidelastic instability occurs. However, there are differences in the post-stable fluidelastic behaviour between the two arrays and this is discussed in section 5.4.

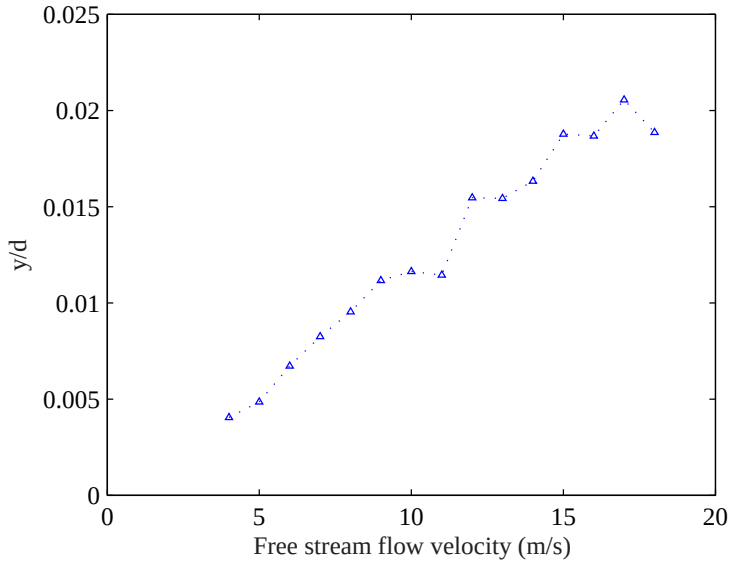

Figure 4.3: P/d=1.97 RMS of tube motion: $\Delta, \delta_{st} = 0.017$

For the pitch ratio of 1.97, only one level of damping is presented and this was the lowest level that could be achieved with this setup. It was observed that the vibration amplitude generally increased as the flow velocity increased. Unlike P/d=1.32 and 1.58 no rapid change in vibration was observed. Hence, the observed vibration was attributed to turbulent buffeting. Furthermore, the two criteria were also not satisfied implying fluidelastic instability does not occur for the velocity range tested.

Two criteria for determining the critical velocity, U_c, are mentioned above. The criterion proposed by Austermann & Popp [2] was used in this study. The tube response against flow velocity was idealised with two straight lines above and below the critical velocity. The critical velocity was obtained from the point of intersection of the two lines. This process was done for both logarithmic and linear scaling of the tube response plots where good agreement between the two approaches was found. Irrespective of the method chosen to determine the critical velocity, using the tube response against velocity to determine U_c is problematic as there is always going to be an element of subjectivity when obtaining U_c especially where the change in tube response is more gradual in less dense arrays. For the arrays where fluidelastic in-

Pitch Ratio (P/d)	1.32	1.32	1.32	1.58	1.58	1.58
Logarithmic decrement, δ_{st}	0.077	0.098	0.123	0.017	0.023	0.030
Critical velocity, U_c (m/s)	3.6	4.2	4.7	5.3	6.0	6.9
Reduced velocity, $U_c/(f_n d)$	14.4	16.7	18.7	21.1	23.9	27.5
Reduced gap velocity, V_r	68.6	79.5	89.0	40.3	45.6	52.5

Table 4.2: Fluidelastic stability thresholds

stability was apparent (P/d=1.32 and 1.58), the values obtained for the critical flow velocity are summarised in Table 4.2. The values obtained for U_c are also found to be consistent with reports in the literature. Figure 4.4 plots the stability threshold in terms of reduced gap velocity[1] and mass damping parameter together with data from Austermann & Popp [2] and Price & Zahn [3]. These two sources were chosen as they have a similar set up to the current experiments (a single flexible cylinder in a normal triangular array and air as the working fluid). It can be seen that the current results compare favourably with the data available from these studies.

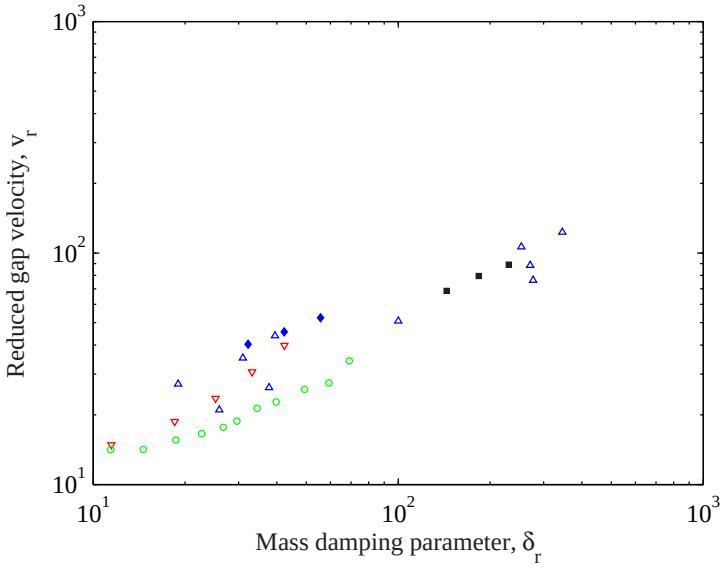

Figure 4.4: Comparison of measured stability thresholds: ○, Austermann & Popp [2], P/d=1.25; ∇, Austermann & Popp [2], P/d=1.375; Δ, Price & Zahn [3], P/d=1.375; ■, present, P/d=1.32; ♦, present, P/d=1.58.

[1]In an attempt to compare data from different array geometries and pitch ratios, Chen [106] proposed the reduced gap velocity and has now become a common way to present such data.

$$V_r = \left(\frac{P}{P-d}\right)\left(\frac{U}{f_n d}\right)\left(\frac{1}{2.105(P/d-0.9)}\right)$$

4.2 Tube Response with Acoustic Resonance

Price & Zahn [3] and Meskell & Fitzpatrick [10] reported an apparent interaction between fluidelastic instability and acoustic resonance. In order to examine the interaction between the two phenomena and determine if the apparent interaction between the phenomena was a coincidence (i.e. by chance) or otherwise, the duct acoustics were artificially excited using speakers to excite the second acoustic mode of the duct in this setup at a frequency of 1092Hz (P/d=1.32) at various loudness levels.

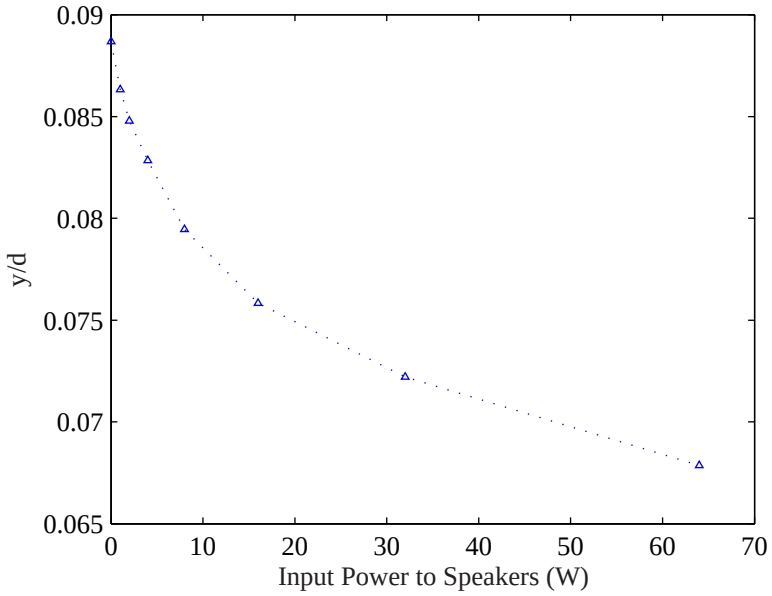

Figure 4.5: P/d=1.32. Vibration amplitude against speaker power at $U = 8.9m/s$

It was observed that a single flexible cylinder went unstable due to fluidelastic instability for the pitch ratios of 1.32 and 1.58. Hence, initial testing examined the effect of acoustic resonance at the second acoustic mode for the two pitch ratios. The preliminary tests examined the tube response at a given velocity (where the tube response was classified to be in a post-stable regime) with and without forced acoustics. The speaker power range[2]: 0, 1, 2, 4, 8, 16, 32 and 64W were used for the levels of damping shown in Table 4.2. For P/d=1.32 a velocity of 8.9m/s was used. Figure 4.5 shows the effect of acoustic resonance plotting non-dimensional tube vibration amplitude, y/d, as a function of speaker input power at $\delta_{st} = 0.098$. The

[2]The reason for using speaker power rather than sound pressure level is discussed later in this section.

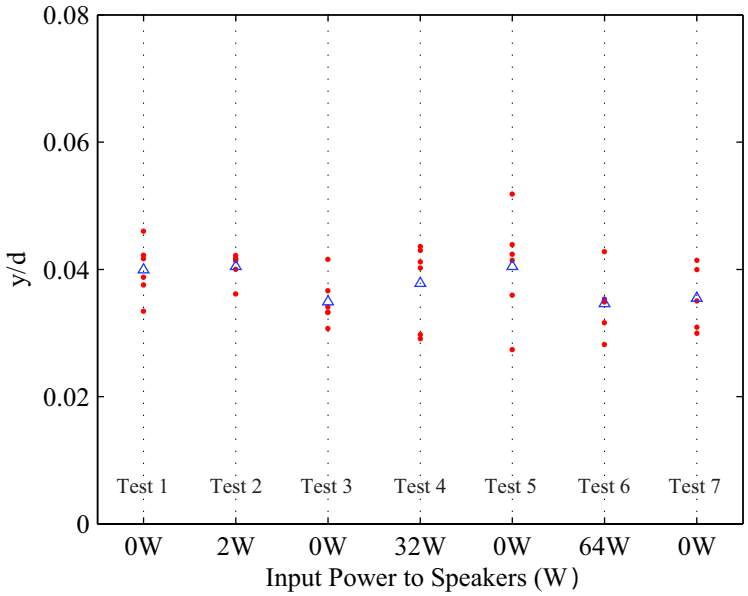

Figure 4.6: P/d=1.58. Sequence of tests from left to right showing vibration amplitude against speaker power at $U = 9m/s$. •, individual test; Δ, average of the five tests

results show that there was a drop in the tube vibration amplitude with increased speaker input power. For P/d=1.58, Fig. 4.6 shows a sequence of tests conducted at $\delta_{st} = 0.030$ and $U = 9m/s$. The test sequence (1-7) moves from left to right with the input power to the speaker varying accordingly (l to r: 0, 2, 0, 32, 0, 64, 0W). The tests were repeated five times. It was observed that the acoustic resonance had no significant effect on the vibration amplitude. The amplitude varied from test to test independently of whether forced acoustics was applied or not. This was also shown to be the case at $U = 11m/s$ for the same level of damping and also for $U = 7m/s$ and $9m/s$ at $\delta_{st} = 0.017$. This suggests a fundamental difference in the fluidelastic behaviour between the two arrays tested. However, it is likely that the effect of acoustic resonance could also have been obscured by the fact that for pitch ratio of 1.58 well established limit cycles did not exist and this will be discussed in section 5.4.

Preliminary tests were also conducted at the first acoustic mode of 592Hz, this resulted in small changes in the tube response but no coherent trend emerged with increasing speaker power. It is likely that the first acoustic mode affected the tube response but was not interacting with fluidelastic instability. Firstly, the variation of the tube response with forced acoustics was larger than would be expected with

randomness from one test to the next allowing for variations due to turbulent buffeting. At a speaker input power of 64W the corresponding sound pressure level at the first acoustic mode was $\sim 160dB$, 20dB in excess of maximum level observed for the same input power for the second acoustic mode. So, the pressure and acoustic particle velocity were of the order of $4.84m/s$ and $2000Pa$, respectively, which correspond to an order of magnitude greater than the values observed for the second acoustic mode. In this instance, it is thought the acoustic standing wave changes the velocity gradient across the array resulting in a modified pressure distribution on the cylinder as was illustrated by Fitzpatrick *et al.* [67] and this results in the increased spread in the tube vibration response. Given that the first acoustic mode was not interfering with fluidelastic instability, no further examination at this mode will be considered.

It was shown above that acoustic resonance at the second acoustic mode had an effect on fluidelastic instability in the pitch ratio of 1.32 but no effect on the pitch ratio of 1.58. Hence, the tests discussed below are related to the interaction between fluidelastic instability and acoustic resonance at the second acoustic mode for P/d=1.32.

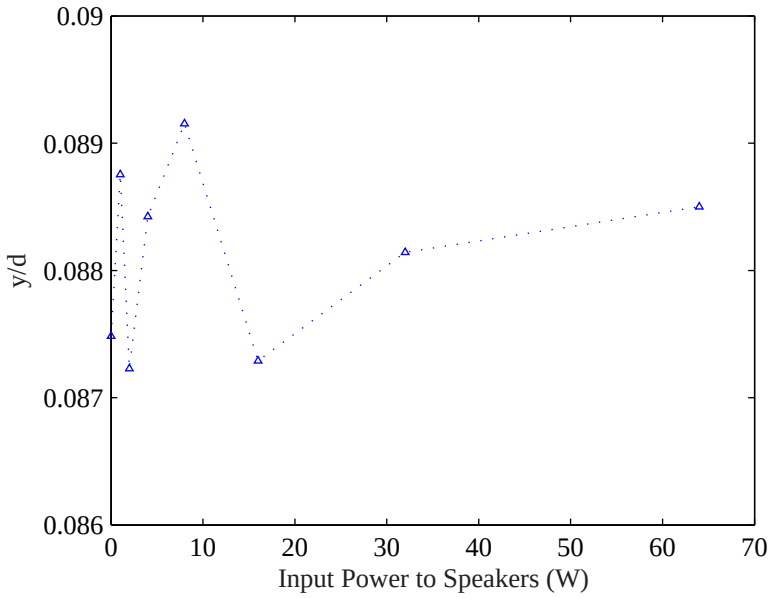

Figure 4.7: P/d=1.32. Vibration amplitude against against speaker power at $U = 8.9m/s$ at first acoustic mode

The first series of tests discussed examine the effect of acoustic resonance on fluidelastic instability in terms of the change in RMS level of tube vibration and this was carried out by modifying three independent variables

- Speaker Power
- Flow Velocity
- Structural Damping

The test procedure was similar to that of the fluidelastic threshold tests. Tests were conducted at a structural damping level of $\delta_{st} = 0.098$ and for a range of speaker power (0, 1, 2, 4, 8, 16, 32 and 64W). The tests were repeated for two free stream flow velocities, 7m/s and 8.9m/s. The sound pressure level of the acoustic resonance was controlled indirectly by the speaker input power. Figure 4.8 shows the relationship between speaker power and measured sound pressure level in the tube array for the two free stream velocities under test. For a given speaker power input, small differences in the sound pressure level are observed at the two flow velocities. This was attributed to the broadband noise generated by turbulent buffeting and was illustrated when no imposed acoustics was applied where clear differences between the sound pressure level at 7m/s and 8.9m/s were observed. It was for this reason that speaker power rather than sound pressure level was used as an independent variable. However, it was clear that as the speak power was increased, there was an increase in sound pressure level, thus an increase in speaker power can also be considered as an increase in sound pressure level.

Figure 4.9 shows non-dimensional tube vibration amplitude, y/d, as a function of speaker input power. The results show that at both free stream flow velocities there was a drop in the tube vibration amplitude with increased speaker input power. Similar findings were also observed when the flow velocity was fixed at 8.9m/s and the level of structural damping was modified, as illustrated in Fig. 4.10. It was apparent from both Fig. 4.9 and 4.10 that the effect of acoustic resonance on fluidelastic instability was not only dependent on sound pressure level but also the free stream flow velocity and the level of structural damping.

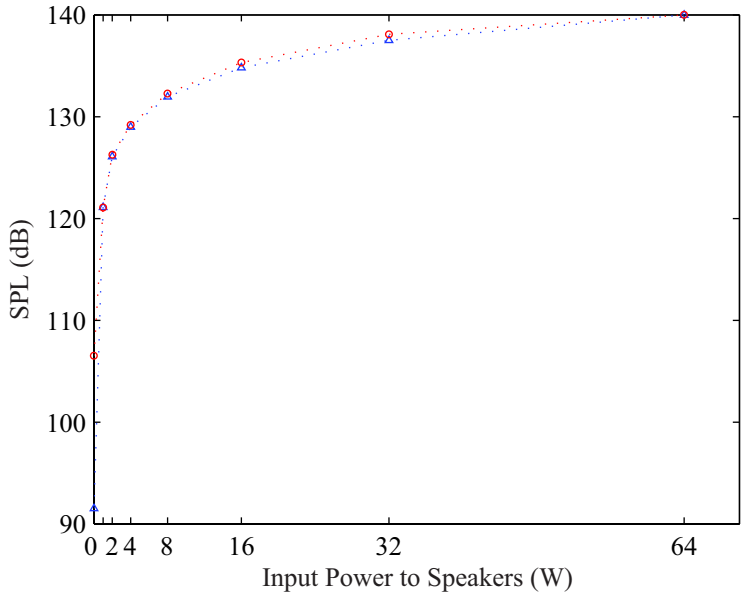

Figure 4.8: SPL against input power to speaker: ∘, 7m/s and Δ, 8.9m/s

Figure 4.11 shows the effect of acoustic resonance on the fluidelastic stability threshold ($\delta_{st} = 0.088$). The critical velocity was increased from 3.8m/s to 4.3m/s when subject to artificially excited acoustic resonance (speaker power = 32W). Furthermore, reductions in the vibration amplitude as a result of the acoustic resonance are shown at all velocities in the critical and post-stable regimes.

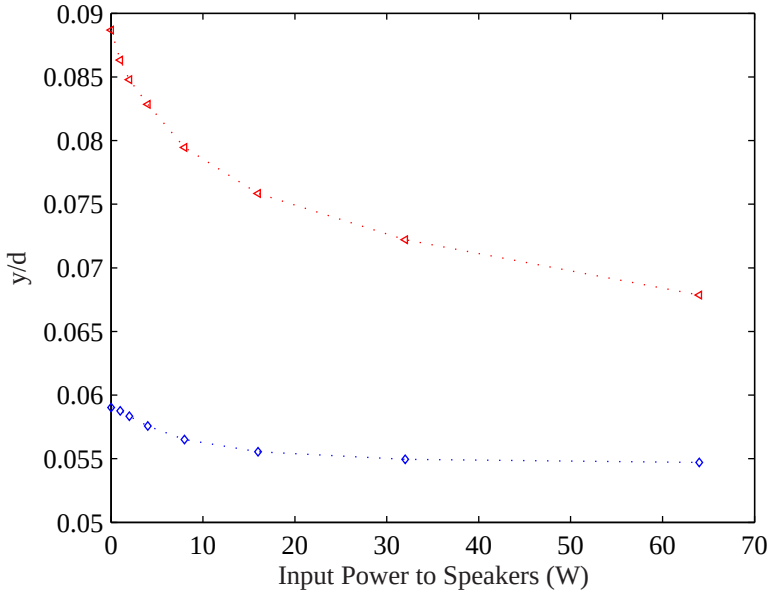

Figure 4.9: Vibration amplitude against input power to speaker: $\diamond, 7m/s$; and $\triangleleft, 8.9m/s$

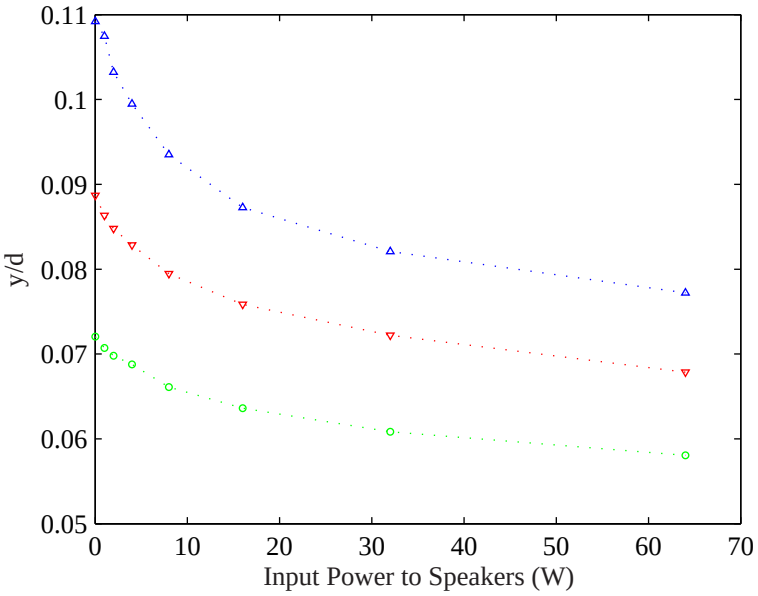

Figure 4.10: Vibration amplitude against input power to speaker: $\Delta, \delta_{st} = 0.077$; $\nabla, \delta_{st} = 0.098$; $\circ, \delta_{st} = 0.123$

Figure 4.12 shows a time trace of tube displacement at $\delta_{st} = 0.088$ and a flow velocity of 4.5m/s with and without acoustic excitation. At $t = 0s$ acoustic excitation was applied with a speaker power of 64W. It was seen that the effect of acoustic resonance was to reduce the vibration amplitude by more than 50% from an average amplitude of 1.76mm to 0.82mm. It was also clear that there is a transition period between the two regimes. This can be attributed to three transient effects: firstly, the speaker power does not reach a maximum instantaneously; secondly, it take time for the acoustic resonance to establish fully, and thirdly, the tube was already vibrating at a higher level and time was required for the amplitude to decay to the new state.

As well as illustrating the effect of sound pressure level on fluidelastic instability amplitude, Fig. 4.9 also shows a dependence on free stream flow velocity. This is more clearly seen in Fig. 4.13 which plots the change compared to no acoustics (as a result of acoustic resonance) in RMS level of non-dimensional tube displacement, $\Delta y/d$. The higher flow velocity (8.9m/s), shows the greatest reduction in vibration amplitude with the largest reduction observed being ∼25% in comparisons to ∼8% for tests conducted with a flow velocity of 7m/s. At the level of structural damping used in this case the fluidelastic stability threshold without acoustic excitation was $U_c = 4.2m/s$, so at both

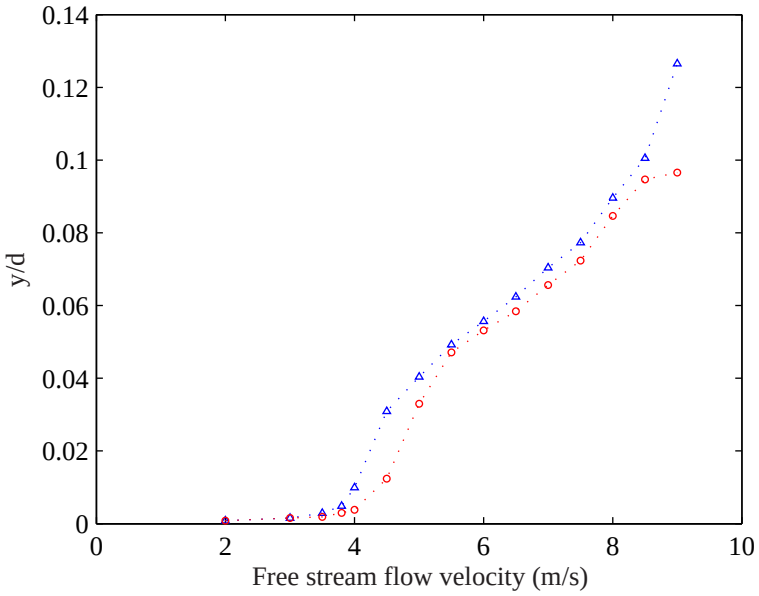

Figure 4.11: RMS of tube vibration at $\delta_{st} = 0.088$: Δ, without acoustic excitation and $\circ$, with artificially excited acoustic resonance (speaker power = 32W)

flow velocities the tube motion was in a post-critical regime. It seems that the effect of the acoustic resonance on the limit-cycle amplitude is related to the tube vibration amplitude as well as the cross flow velocity but the nature of this is uncertain as at lower velocities closer to the critical velocity the change in vibration amplitude was also large (see Fig. 4.11).

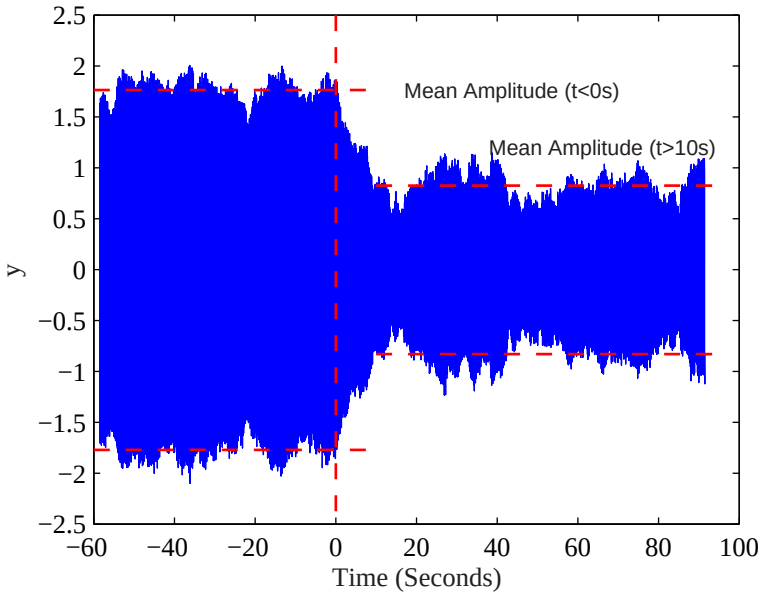

Figure 4.12: Time trace of tube displacement. Acoustic excitation applied at $t = 0s$

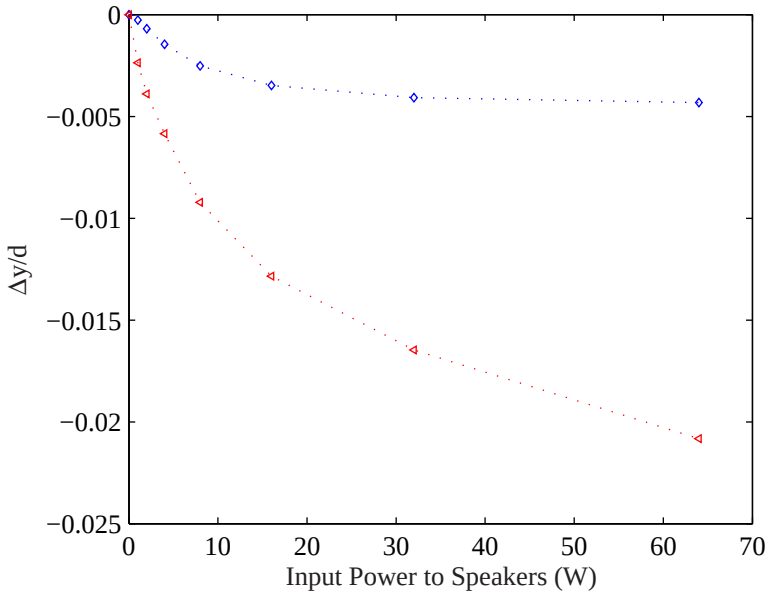

Figure 4.13: Change in vibration amplitude against input power to speaker: $\diamond, 7m/s$ and $\triangleleft, 8.9m/s$

Figure 4.14 plots the change in RMS level of non-dimensional tube displacement, $\Delta y/d$, for three levels of structural damping (δ_{st} = 0.077, 0.098, 0.123). The lower the structural damping, the more responsive the fluidelastic mechanism was to the artificially excited acoustic resonance. This finding could intuitively be explained by superposition of the independent damping mechanisms (i.e. additional energy dissipation by the sound field). However, as will be shown below, this does not explain all the experimental observations.

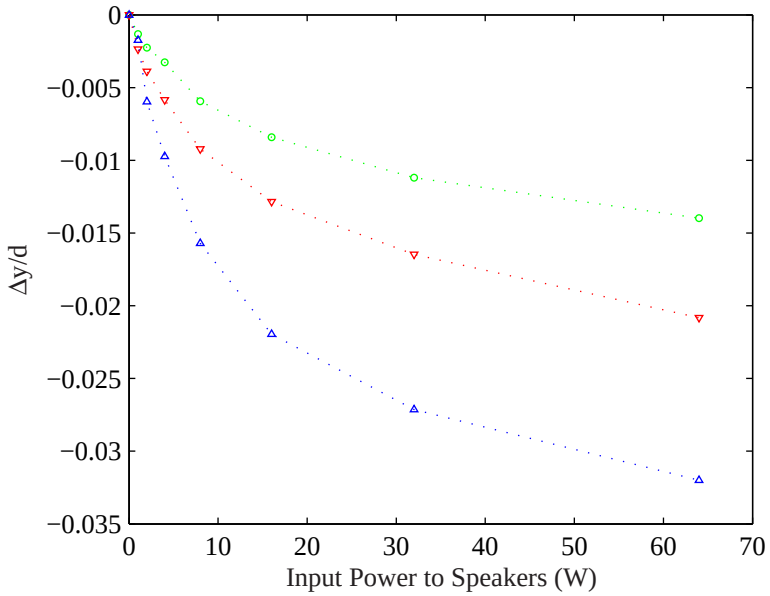

Figure 4.14: Change in vibration amplitude against input power to speaker: Δ, $\delta_{st} = 0.077$; $\nabla, \delta_{st} = 0.098$; $\circ, \delta_{st} = 0.123$

4.2.1 Fluidelastic Damping with Forced Acoustics

In this section the effect of acoustic resonance on effective total fluidelastic damping is examined. A series of free decay tests were conducted in which the flexible tube was given an initial displacement of 11mm and released from rest. Tests were conducted at a flow velocity of 8.9m/s and various structural damping levels. The data acquisition was triggered by the tube acceleration so it was possible to perform ensemble averaging in the time domain. For each condition (speaker power and structural damping level), 20 records, each with 8s of data at a sample rate of 2048Hz were obtained and averaged. This follows the same procedure outlined by Meskell & Fitzpatrick [10].

Identification Technique

The equation of motion for the tube under fluid loading is

$$m_s\ddot{y}_i + c_s\dot{y}_i + k_s y_i = E(y_i, \dot{y}_i, \ddot{y}_i, U) + A_i(U,t) + V_i(U,t) + T_i(t) \tag{4.1}$$

where y_i is the displacement of the tube in test i, c_s is the structural damping in quiescent air; k_s is the structural stiffness; $E(y_i, \dot{y}_i, \ddot{y}_i, U)$ is the fluidelastic force which is dependent on the flow velocity and tube displacement; $A_i(U,t)$ is the fluid force due to acoustic resonance at the acoustic resonance frequency and the acoustic interaction with fluidelastic instability is embedded in $E(y_i, \dot{y}_i, \ddot{y}_i, U)$; $V_i(U,t)$ is the fluid force due to vortex shedding and $T_i(t)$ is the turbulent excitation in test i.

The total response was decomposed into the sum of the various excitation responses: fluidelastic excitation, acoustic resonance, vortex shedding and turbulent buffeting,

$$y_i(t) = y_E(t) + y_A(t) + y_V(t) + y_T(t) \tag{4.2}$$

where $y_E(t)$, $y_A(t)$, $y_V(t)$ and $y_T(t)$ are defined by

$$m_s\ddot{y}_E + c_s\dot{y}_E + k_s y_E = E(y_E, \dot{y}_E, \ddot{y}_E, U) \tag{4.3}$$

$$m_s\ddot{y}_A + c_s\dot{y}_A + k_s y_A = A_i(U,t) \tag{4.4}$$

$$m_s\ddot{y}_V + c_s\dot{y}_V + k_s y_V = V_i(U,t) \tag{4.5}$$

$$m_s\ddot{y}_T + c_s\dot{y}_T + k_s y_T = T_i(t) \tag{4.6}$$

This assumes that there is no interaction between the excitation mechanisms which is not strictly correct as fluidelastic excitation depends on tube motion which will inherently be influenced by the other phenomena, hence, an interaction between the phenomena will exist. However, if the tube motion is large, this interaction will be small due to the small contribution of the other phenomena. If n tests are conducted with the same initial conditions, one would expect $y_E(t)$ to be identical for each test. Neither acoustic resonance nor vortex shedding responses were phase locked to the free decay motion, so when averaged each of the effects will sum towards zero. In addition, the turbulent response will vary randomly from one test to the next. Thus if the ensemble is averaged, only the fluidelastic force with the effect of the acoustic interaction embedded will remain

$$y(t) = \frac{1}{n}\sum_{i=1}^{n} y_i(t) \approx \frac{1}{n}\sum_{i=1}^{n} y_E(t) \tag{4.7}$$

The equation of motion associated with the ensemble average response is

$$m_s\ddot{y} + c_s\dot{y} + k_s y = E(y, \dot{y}, \ddot{y}, U) \tag{4.8}$$

Since the fluid in this study was air, the added fluid mass, m_f, can be assumed to be negligible, and as it is generally assumed that the fluidelastic excitation does not depend on tube acceleration. Hence, the equation of motion for the system assuming $E(y, \dot{y}, U)$ is linear, becomes

$$m_s\ddot{y} + (c_s + c_f(U))\dot{y} + (k_s + k_f(U))y = 0 \tag{4.9}$$

where the subscript f denotes the fluid parameters. It must be noted that E is non-linear in tube motion. However, the non-linearity is very weak and therefore it is still valid to take E as effectively linear when a comparison is being made at a given level of structural damping.

Effective Negative Linearised Fluid Damping

Using Eqn. 4.9 to describe the ensemble data, the effective linear fluid and structural damping can be obtained. The results are summarised in Table 4.3. The structural damping values were obtained by tests conducted in quiescent fluid and are shown along the top of the table. The left column details the various acoustic conditions. Conditions (a), (b) and (c) correspond to a speaker power of 0, 8 and 64W, respectively. The body of the table presents the total level of effective negative linear fluid damping (i.e. the structural component has been removed). For the three test cases shown in Table 4.3, there are differences in the effective linearised fluid damping for each of the three different structural damping levels. It might be expected that this data should collapse to a single value as the linear fluid damping is independent of structural damping [10]. This is clearly not the case. In this study, the effective linear fluid damping has been measured and the non-linear damping was implicitly accounted for in this effective linearised damping. This does not compromise the validity of the comparison of the damping values for increasing speaker power at a given level of structural damping as the initial value of displacement in the free decay tests was constant. However, it should be noted that if the values of linearised damping where used to predict the fluidelastic threshold the critical velocity obtained would be overestimated.

		Structural Damping, δ_{st}		
Condition	Speaker Power (W)	0.205	0.138	0.124
a	0	-0.112	-0.088	-0.080
b	8	-0.095	-0.076	-0.073
c	64	-0.088	-0.072	-0.070

Table 4.3: Effective Negative Linearised Fluid Damping, c_f, with U=8.9m/s and various levels of Speaker Power

When the flexible tube was subject to fluid flow, negative fluid damping was observed as has been widely reported in the literature. This is illustrated by condition (a) which shows the effect free stream flow velocity with no acoustic input. Conditions (b) and (c) highlight the effect of acoustic resonance on the effective linearised fluid damping. Condition (b) introduces acoustic resonance at a sound pressure level of $\sim$130dB

(speaker power = 8W) measured at the test section wall. The drop in fluid damping was further augmented when the sound pressure level was increased to ∼140dB (speaker power = 64W) as shown by condition (*c*). Conditions (*b*) and (*c*) demonstrate that the effect of the acoustic resonance on fluid damping was to reduce the magnitude (negative) increasing overall damping. Therefore, the acoustic resonance adds additional damping. Furthermore, the extent of the reduction in the effective linearised fluid damping seen in Table 4.3 was related to the sound pressure level. As the sound pressure level increases, the magnitude of the linearised effective fluid damping is reduced. These results are shown across the board irrespective of the initial structural damping level. However, it was not clear from the test results presented in Table 4.3 whether the additional damping will also occur in quiescent fluid.

4.3 Possible Physical Mechanisms

It is difficult to envisage the physics of a true interaction between fluidelastic instability and acoustic resonance given that the phenomenon of fluidelastic instability typically occurs at a frequency of approximately $6.6Hz$ while the acoustic resonance frequency is two orders of magnitude larger, at 1092Hz. This sections examines alternatives to an interaction between the two phenomena which could explain the observations reported.

In the previous section it was shown that acoustic resonance adds positive damping, it is not clear whether this would also occur in quiescent fluid. It might be argued that the acoustics provides an additional damping force which was simply superimposed on the structural damping and flow-induced damping and was independent of fluid flow. In order to resolve this issue, a series of tests were conducted without flow. Figure 4.15 shows three levels of structural damping plotted against input power to the speakers. For all three levels of damping tested, there are slight variations in the damping parameter, with a maximum deviation of 2% from the mean value. These variations are consistent with random experimental error. It has been shown that the sound field does not provide an additional damping force independently of the flow, implying that superposition of independent phenomena can be excluded.

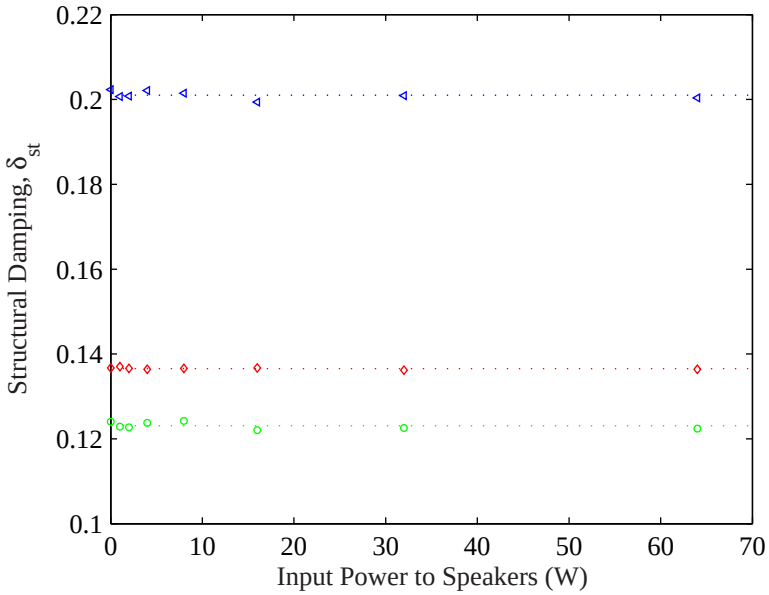

Figure 4.15: Structural damping against input power to speaker

Acoustic resonance can cause a change in the pressure drop across the array, hence a change in mean flow velocity. Such findings have been reported by Blevins & Bressler [107] and Feenstra *et al.* [58]. In these studies, the acoustic resonance with a sound pressure level in excess of 160dB modified the load on the wind tunnel fan, changing the free stream flow velocity and hence the amplitude of vibration. However, throughout the current tests the free stream flow velocity was monitored and no change was recorded with acoustic resonance. So, although reports in the literature have shown acoustic resonance may effect the free stream flow velocity, this did not occur in the present study. The reason for this is due to the low sound pressure level of 140dB observed here relative to the studies in the literature.

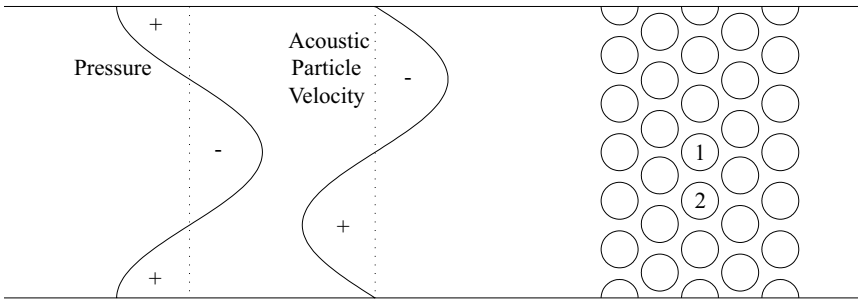

Figure 4.16: Acoustic particle velocity and pressure curves at the second acoustic mode

The effect of acoustic particle velocity was also examined as it was thought it may affect the local fluid mechanics in the vicinity of the flexible cylinder. This was done by relocating the flexible cylinder position. At position 1, the acoustic particle velocity was a minimum as shown in Fig. 4.16 and there was an interaction between fluidelastic instability and acoustic resonance. When the tube was moved to position 2, where the acoustic particle velocity was higher, the effect of acoustic resonance on fluidelastic instability was still observable. This is illustrated in Fig. 4.17 which plots the stability threshold with and without acoustic resonance. The behaviour of the flexible cylinder when subject to acoustic resonance was similar at both position 1 and 2. This suggests that the effect of acoustic particle velocity was small, as different magnitudes of acoustic particle velocity did not result in a change in the behaviour of the interaction between fluidelastic instability and acoustic resonance. It was therefore

concluded that acoustic particle velocity was not the cause of the observed interaction between the two phenomena. However, as will be shown later this does not mean that the effect of acoustic particle velocity was zero. In fact at sufficient levels of sound pressure levels the corresponding acoustic particle velocity can be of the same order of magnitude as the bulk flow thus altering the local flow field and the pressure distribution on the cylinder.

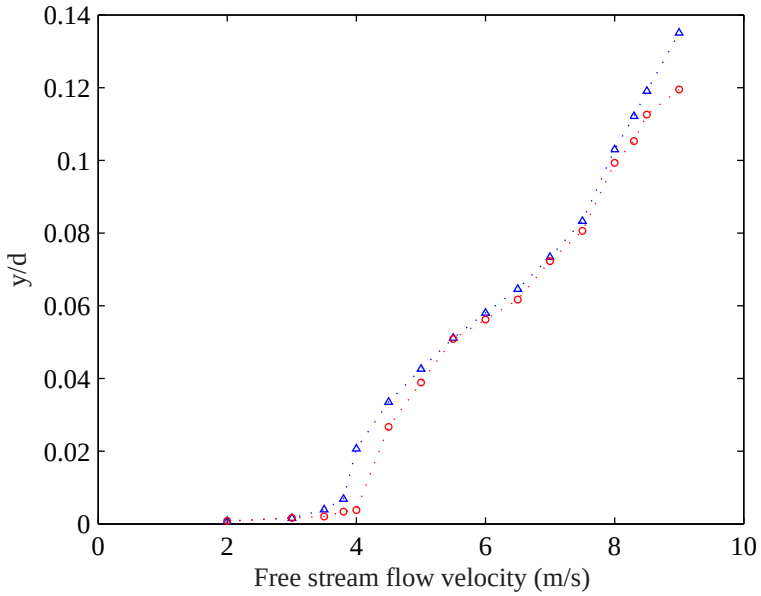

Figure 4.17: RMS of tube vibration at position 2 at $\delta_{st} = 0.088$: Δ, without acoustic excitation and $\circ$, with artificially excited acoustic resonance (speaker power = 32W)

It has also been reported that acoustic resonance can organise the flow in a tube array (for example Price & Zahn [3]). Granger & Paidoussis [82] and others have reported an apparent interaction between fluidelastic instability and vortex shedding as was discussed in section 2.4.5. It is conceivable that acoustic resonance was interacting with vortex shedding which then modifies the fluidelastic behaviour. However, in the current study no evidence of Strouhal dependency or lock-in phenomenon was observed, suggesting that vortex shedding does not play a significant role.

4.4 Summary

These tests have captured and quantified the effect of acoustic resonance. However, it is not clear as to how the mechanism of fluidelastic instability at approximately 6.6Hz can interact with acoustic resonance at a frequency of over two orders magnitude larger at 1092Hz. A number of probable causes for the interaction were examined and have been categorically discounted by experimental tests. Although the interaction has been clearly demonstrated, it is not apparent what the physical mechanisms at work might be. In an attempt to better understand the interaction between fluidelastic instability and acoustic resonance for P/d=1.32 two possibilities are examined which are based on the framework proposed by Price & Paidoussis [1] to model fluidelastic instability. Section 6.1 will examine the effect of acoustic resonance on the static fluid forces on a static cylinder. Whilst section 6.3 will examine the effect of acoustic resonance on the time delay between tube motion and the resultant flow reorganisation close to the measurement cylinder.

Chapter 5

Pressure Distributions & Fluid Forces

Reviewing the literature reveals that there is no comprehensive database on the surface pressure distribution around a cylinder within an array. There are a number of papers presented but the range of tests were small. It would be useful to have such a database for the validation of models. It is also apparent that there are no comprehensive studies available on the surface pressure distribution around a statically displaced cylinder within a tube array and hence the formulation of the fluid forces as a result of a static tube displacement. Since the pressure distribution around the cylinder results from the local flow structure around the tube, these measurements provide information about the actual flow conditions, which are of importance for the physical understanding of the flow and may explain the behavioural differences in fluidelastic instability for the pitch ratios of 1.32 and 1.58. More importantly, a detailed pressure survey is a prerequisite for section 6.1 which examines the effect of acoustic resonance on the surface pressure distribution around a cylinder.

5.1 Pressure Measurements

A series of tests were conducted to measure the mean pressure distribution around a cylinder in the third row of three five row normal triangular tube arrays with pitch ratios of 1.32, 1.58 and 1.97. Measurements were conducted for a range of free stream flow velocities. Table 5.1 presents the free stream velocities (U) investigated and the respective gap velocities (U_g) and Reynolds numbers (Re). Note the Reynolds numbers

presented are based on the gap velocities and the tube diameter. The mean pressure distribution and resulting fluid forces were also measured for a tube statically displaced within the array and these tests are outlined later.

	P/d=1.32		P/d=1.58		P/d=1.97	
$U\ (m/s)$	$U_g\ (m/s)$	Re ($\times 10^4$)	U_g	Re ($\times 10^4$)	U_g	Re ($\times 10^4$)
2	8.3	2.23	-	-	-	-
3	12.5	3.34	8.2	2.19	-	-
4	16.7	4.46	10.9	2.92	8.1	2.17
5	20.8	5.58	13.6	3.65	10.1	2.72
6	25.0	6.70	16.4	4.38	12.2	3.26
7	29.2	7.82	19.1	5.12	14.2	3.80
8	33.3	8.93	21.8	5.85	16.2	4.35
9	37.5	10.05	24.5	6.58	18.2	4.89
10	41.7	11.16	27.3	7.31	20.3	5.43
11	-	-	30.0	8.04	22.3	5.98
12	-	-	32.7	8.77	24.3	6.52
13	-	-	35.4	9.50	26.4	7.06
14	-	-	38.2	10.23	28.4	7.60
15	-	-	-	-	30.4	8.15
16	-	-	-	-	32.4	8.69
17	-	-	-	-	34.5	9.23
18	-	-	-	-	36.5	9.78

Table 5.1: Velocities and Reynolds numbers tested

5.1.1 Validation of the test set up

In the first instance the experimental setup was validated by measuring the mean pressure distribution around an isolated cylinder and comparing the results with those in the literature. The measurements were acquired at a sample frequency of 64Hz and for 120 seconds. The data acquisition allowed eight channels to be measured simultaneously. Hence, five runs were required to achieve one complete pressure distribution around the cylinder. The pressure distribution was non-dimensionalised and the results presented in terms of the mean pressure coefficient. The pressure coefficient, C_P, was defined as

$$C_P = 1 - \frac{P_0 - P_\theta}{\frac{1}{2}\rho U_g^2} \tag{5.1}$$

where P_0 refers to the mean pressure at the front stagnation point ($\theta = 0$), P_θ refers to the local mean static pressure at a given angular distance (also referred to as position angle) and is defined as the positive clockwise angle starting from the front of the cylinder (see Fig. 5.1), U_g is the gap velocity ($U_g = U(\frac{P}{P-d})$) and ρ is the fluid density. The pressure coefficient was expressed in this way as taking the free stream static pressure as the reference pressure was not relevant as the mean static pressure varies throughout the array.

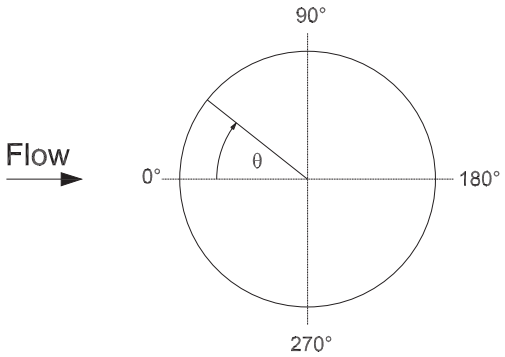

Figure 5.1: Schematic of position angle

The mean pressure coefficient at a Reynolds numbers of 5.6 $\times 10^4$ for an isolated cylinder is shown in Fig. 5.2. The curve compares well with data in the literature. However, small differences are observed which are attributed to the lower Reynolds number tested in this study. Also surface finish and flow conditions are reported to be important parameters which could contribute to the slight differences observed. Nonetheless the comparison with the results from the literature was reasonable, demonstrating the integrity of the setup.

5.1.2 Surface Pressure Measurements in Tube Arrays

Once it was established that the set up to be used provided qualitative agreement with results in the literature, measurements of the surface pressure on a cylinder in the third row of three five row normal triangular tube arrays with pitch ratios of 1.32, 1.58 and 1.97 were undertaken. Measurements of the surface pressure distribution around a cylinder in staggered arrays have previously been conducted by a number of researchers (for example [16, 17, 98, 99]). The pressure distributions are generally measured for

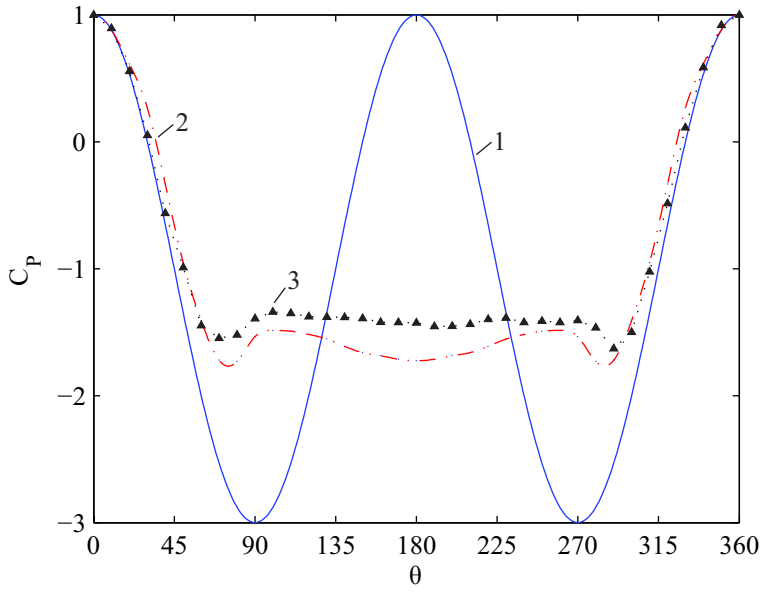

Figure 5.2: Distribution of pressure coefficient over the surface of a cylinder: 1) – , potential flow theory; 2) $- \cdot -$, experimental data from the literature ($Re = 8 \times 10^4$), [4]; 3) ▲, experimental data ($Re = 5.6 \times 10^4$), current study

only a few Reynolds numbers whereas the current study presents a more comprehensive data set with a minimum of nine Reynolds number in each of the arrays investigated. Some of the investigations reported in the literature present pressure distributions for a number of rows. Row dependence has not been investigated as the pressure distribution data was acquired in conjunction with the vibration measurements also made in the third row. However, the effect of a static tube displacement for a single cylinder in the lift direction within an otherwise rigid array is presented and will be discussed later.

Examining the mean pressure distribution in the third row of the three arrays collectively it was clear that there are considerable differences dependent on the array pitch as illustrated in Fig. 5.3. The losses increase with increasing pitch ratio. It was also apparent that neighbouring cylinders in the more compact array has a larger effect as shown by the deceleration in the flow passing through the inter-row gap. The pressure reaches a minimum at the minimum gap ($\pm 90^o$) for P/d=1.32 but this occurs a little earlier ($80^o - 90^o$) for P/d=1.58 and earlier again ($70^o - 80^o$) for P/d=1.97. For all three arrays the pressure distribution was different to that observed for a single cylinder at a similar Reynolds number. The pressure variation at the rear of the

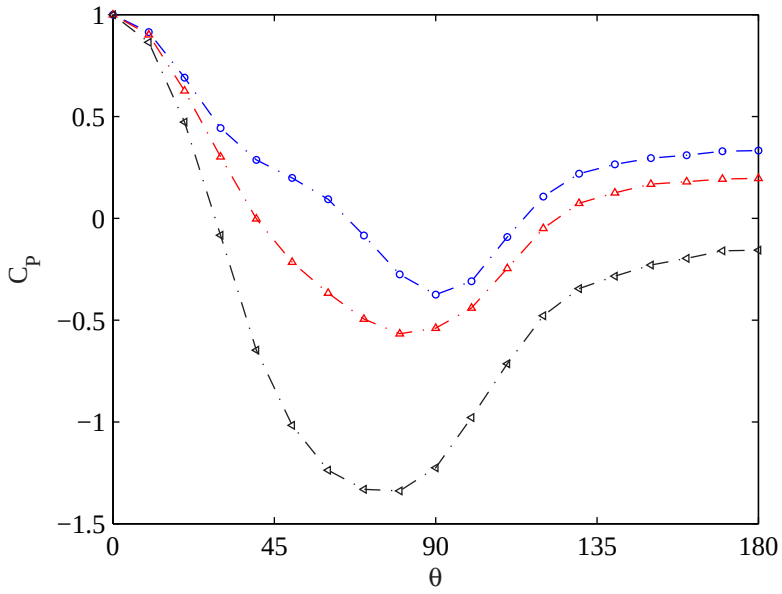

Figure 5.3: C_P comparison at the three pitch ratios tested: ∘, P/d=1.32, $Re = 8.93 \times 10^4$; △, P/d=1.58, $Re = 8.77 \times 10^4$; ◁, P/d=1.97, $Re = 8.69 \times 10^4$

cylinder was small resulting in a small recovery in energy. This indicates boundary layer separation from the tube surface and the existence of a turbulent vortical wake.

Examining the pressure distribution around the whole cylinder it was seen that there was slight asymmetry for P/d=1.32. This was attributed to a rotational offset in the position angle. This resulted in a non zero lift force when the tube was un-displaced ($y/d = 0\%$). However, the offset was quantified and accounted for in the calculation of the lift and drag forces and will be discussed later in this chapter. For P/d=1.58 the pressure distribution was not well behaved showing large asymmetry, in this case the large asymmetry was attributed to flow instability and will be discussed in section 5.2. The pitch ratio of 1.97 showed asymmetry in the pressure distribution the form of which varied with flow velocity. This resulted in a peculiar effect with the lift force fluctuating about zero at lower Reynolds numbers and a net force generated at higher Reynolds numbers. This was not attributed to a rotational offset and can only be explained by a flow induced phenomena. Examining the time resolved pressure signal showed no flow instability. Flow visualisation was attempted to further understand the nature of the flow but proved to be unsuccessful. It was observed that different magnitudes of fluctuations were found on both sides of the cylinder suggesting differences in the

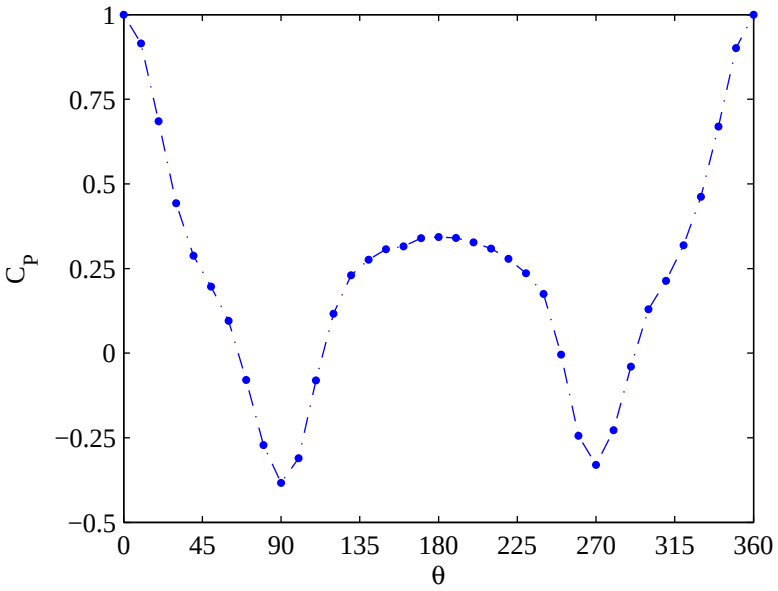

Figure 5.4: P/d=1.32; C_P at $y/d = 0\%$ and $U = 9m/s$

wake of the leeward cylinder. Further experiments are required to better understand the pitch ratio of 1.97. However, it was shown previously that a cylinder in the third row of this array (P/d=1.97) did not go unstable due to fluidelastic instability. As the primary focus of this work was to examine the effect of acoustic resonance on fluidelastic instability, this pitch ratio will not be discussed further. For completeness, data for this pitch ratio can be found in Appendix E.

The effect of Reynolds number was also apparent in all three arrays. For $P/d = 1.32$ there was a Reynolds number dependency at lower Reynolds number and at higher Reynolds numbers C_P collapses reasonably well. Examining C_P at range of positions around the cylinder (see Fig. 5.7) reveals that at the front of the cylinder at higher Reynolds numbers C_P becomes a constant indicating that the pressure in these regions scales proportionally to dynamic head. At the rear and side of the cylinder C_P does not collapse as well, illustrating that the scaling between the pressure in these regions with dynamic head is not as good. For P/d=1.58 the pressure distribution was found to be evolving at all Reynolds numbers tested. Again examining C_P against flow velocity (see Fig. 5.9) on this occasion there is clearly not a relationship between the pressure and dynamic head. It is thought that the poor relationship between pressure and dynamic head for this array was caused by the flow instability.

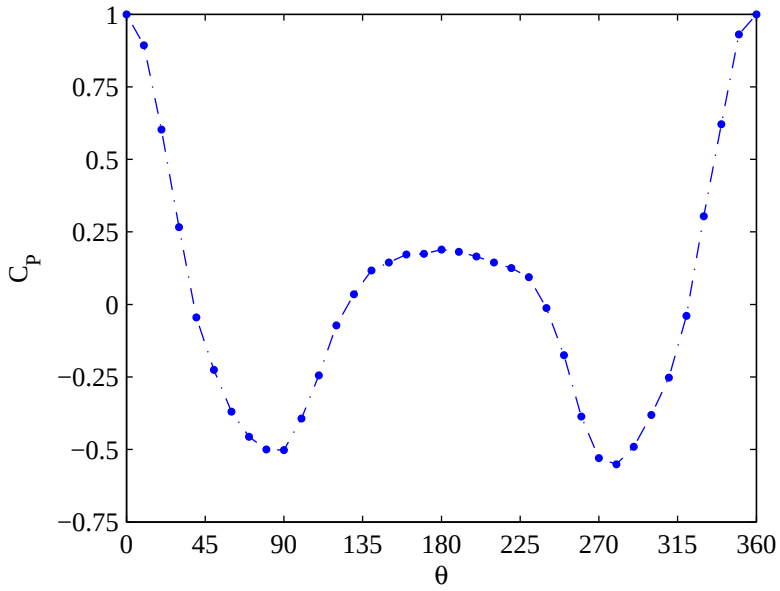

Figure 5.5: P/d=1.58; C_P at $y/d = 0\%$ and $U = 11m/s$

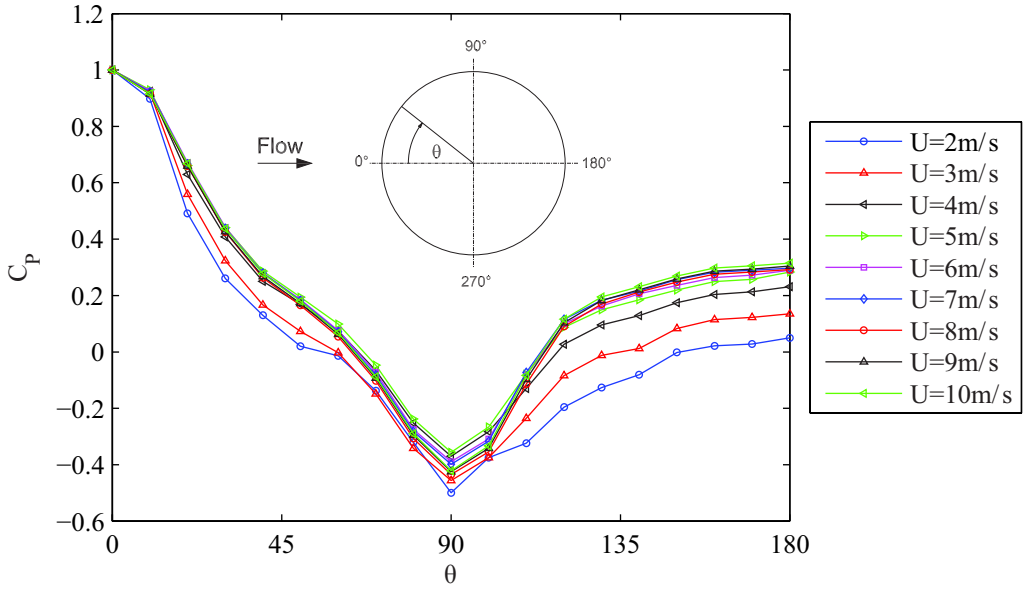

Figure 5.6: P/d=1.32; C_P at $y/d = 0\%$ for a range of flow velocity

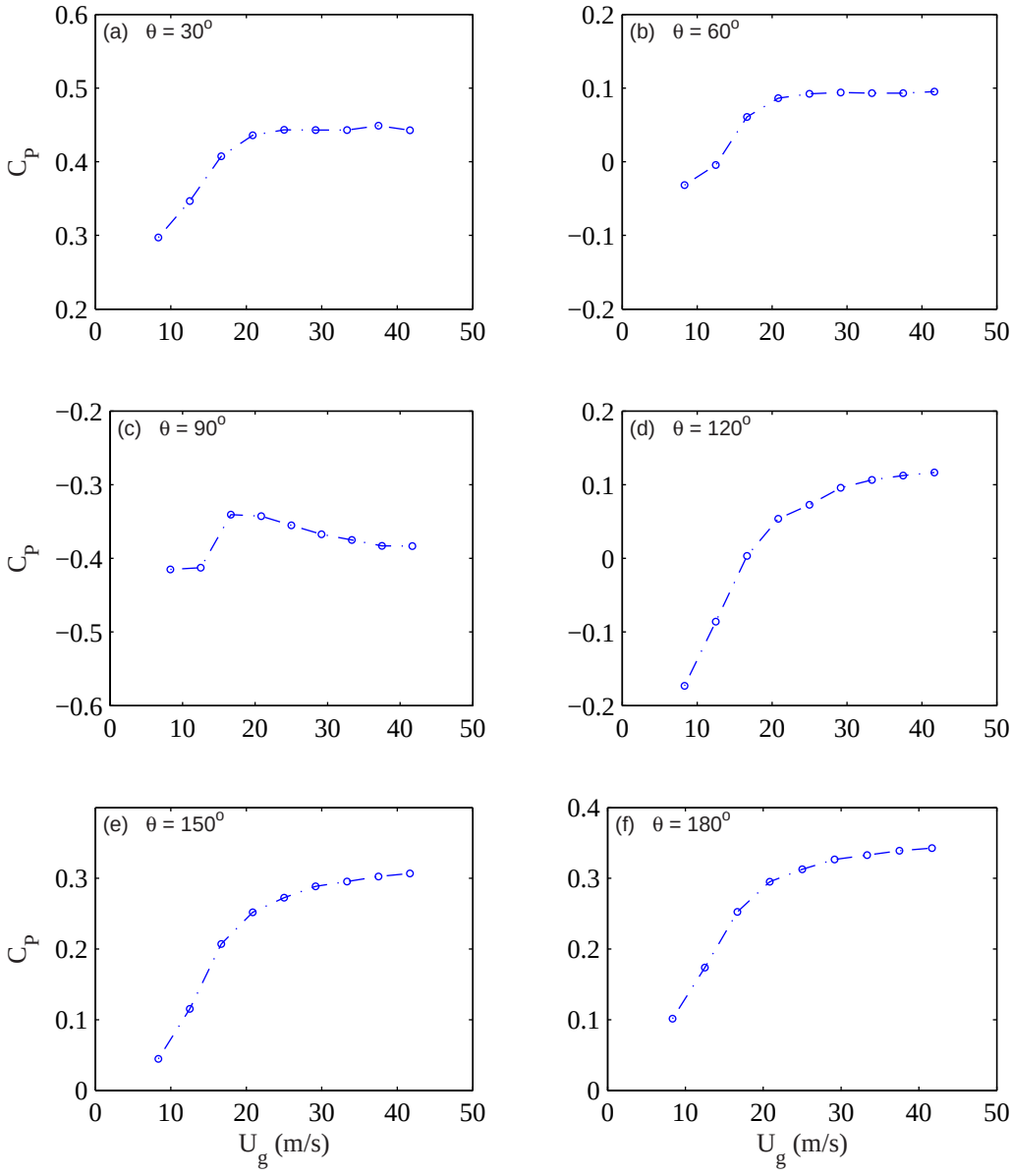

Figure 5.7: P/d=1.32; C_P at various positions around the cylinder

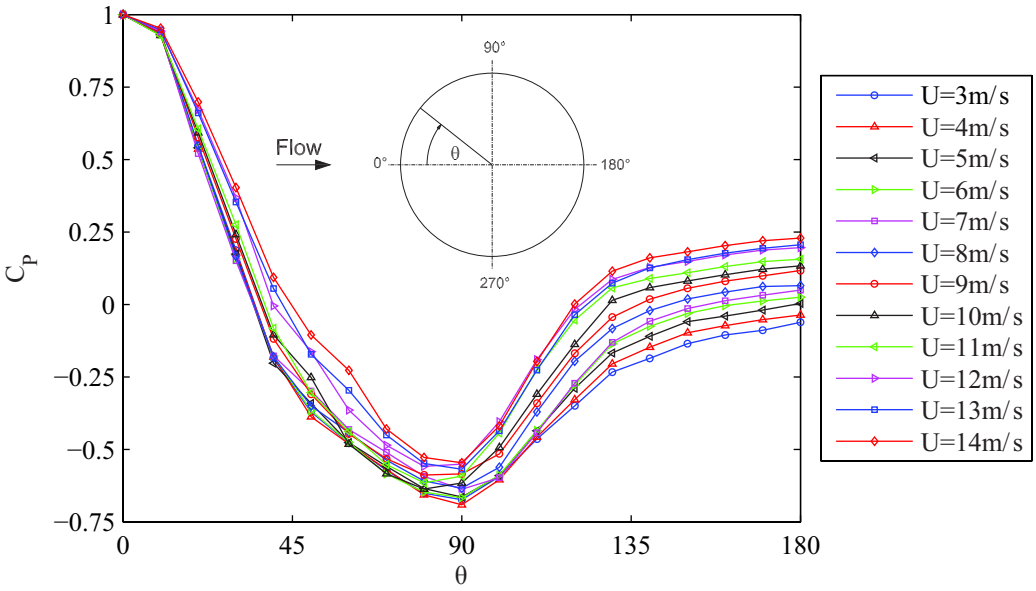

Figure 5.8: P/d=158; C_P at $y/d = 0\%$ for a range of flow velocity

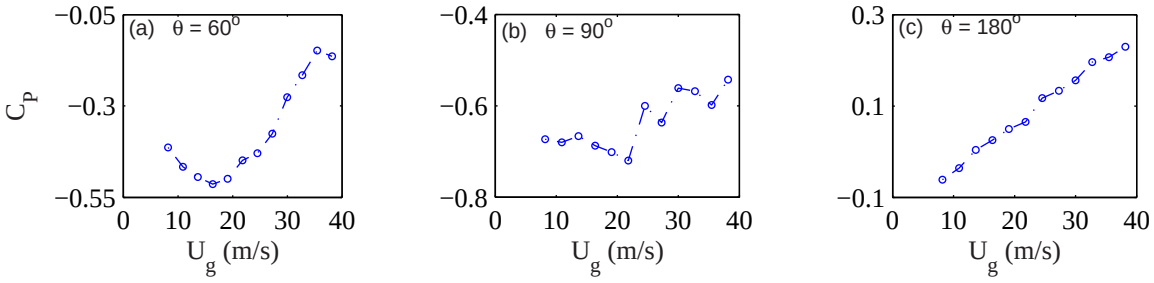

Figure 5.9: P/d=1.58; C_P at various positions around the cylinder

5.1.2.1 Pressure distribution, tube displaced

Static tube displacements tests were also conducted for all arrays and are outlined in Table 5.2. The displacements are quantified in terms of the tube displacement, y, divided by tube diameter, d, resulting in the displacement presented in terms of percentage of tube diameter, (y/d). For each displacement the velocity range investigated was detailed in Table 5.1.

y/d (%)	1.32	1.58	1.97
0	✓	✓	✓
1	✓	✓	✓
2	✓	✓	✓
3	✓	✓	✓
4	✓	✓	✓
5	✓	✓	✓
6	✓	-	-
7	✓	✓	✓
8	✓	-	-
9	✓	-	-
10	✓	✓	✓
-1	-	✓	-
-2	-	✓	-
-3	-	✓	-
-4	-	✓	-
-5	✓	✓	✓
-6	-	-	-
-7	-	✓	-
-8	-	-	-
-9	-	-	-
-10	-	✓	-

Table 5.2: Tube Displacement chart

At all pitch ratios the stagnation point was found to move in the direction opposite to the tube displacement. The change became less pronounced with increasing pitch ratio. The implication of the stagnation point shifting was that the position of the pressure tapping where the total available energy was a maximum was also shifting. In order to retain the integrity of the non-dimensional pressure coefficient and thus facilitate the direct comparison at different displacements, the reference pressure P_0 at $\theta = 0^o$ must be replaced with $P_{\theta max}$ where θmax is the position of the largest

amount of available energy (maximum pressure) which varied depending on tube displacement and the pitch ratio used. The approach of moving the reference pressure better reproduces the trends that emerge from pressure data but now in terms of a non-dimensional pressure coefficient. However, in the pitch ratio of 1.58 the adverse effects from the flow instability where also observed at the reference pressure position. As a consequence using the pressure coefficient would not have yielded reliable results. So, in this section the pressure distribution rather than the pressure coefficient is used to present the results for the pitch ratio of 1.58.

Before examining the effect of tube displacement for the range of displacements, preliminary tests were conducted to determine if positive and negative displacement was important. Figure 5.10 presents the displacement of ±5% for two Reynolds numbers. The data obtained from $y/d = -5\%$ was transposed and plotted with the data obtained from $y/d = +5\%$. For both Reynolds numbers the data collapses reasonably well especially at the front and rear of the cylinder. At the top and bottom of the cylinder the scatter was increased slightly. This results from the asymmetry quantified in the previous section. Nonetheless, the data collapses well and it is therefore acceptable to examine the displacement of the cylinder in the positively defined direction only.

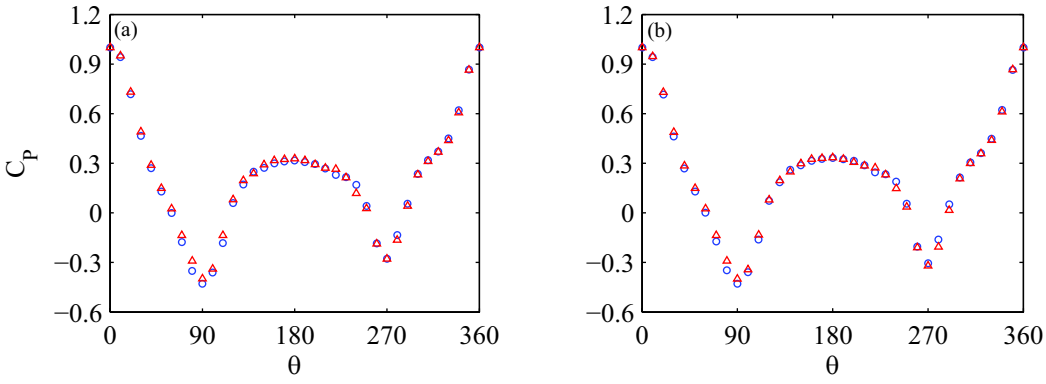

Figure 5.10: P/d=1.32; Comparison of C_P for △, $y/d = +5\%$; *circ*, $y/d = -5\%$; (a) Re=6.7×10^4; (b) Re=1×10^5

Figures 5.11 and 5.12 plot the surface pressure distribution around a cylinder in the third row for a number of static tube displacements for the pitch ratios of 1.32 and 1.58, respectively. Some general trends emerged that are applicable to all pitch ratios.

The stagnation point moved in the direction opposite to the tube displacement. In the densest array geometry (P/d=1.32) tested, the rate at which the stagnation point moves with tube displacement was related to Reynolds number. The shift in stagnation point increased with decreasing Reynolds number. As the array pitch increases the shift in stagnation point reduces. For P/d=1.58 the occurrence of jet switching makes it difficult to categorically report a Reynolds number effect with respect to the shift in the stagnation point.

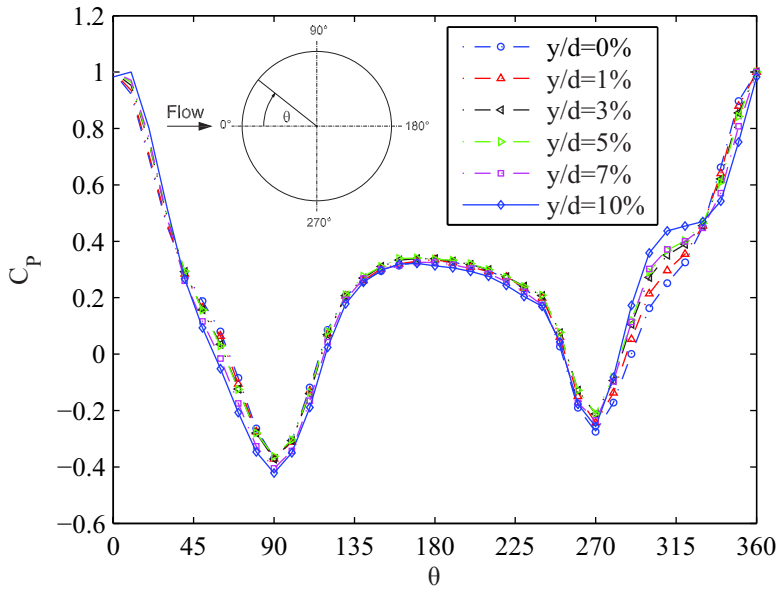

Figure 5.11: P/d=1.32; C_P at various tube displacements, $U = 7m/s$

As detailed previously the most significant changes as a result of tube displacement occurred in the more compact arrays which is not surprising as the geometry was the most restrictive in the more compact arrays. The largest change in pressure coefficient was observed in the region of the minimum gap between the cylinders both in the row $(90^o, 270^o)$ and inter-row $(30^o, 330^o)$ gaps. This was as a result of the change in the flow velocity in those regions caused by the change in the blockage. For P/d=1.58 the largest changes occurred at the minimum gap and to a lesser extent at the inter-row gap. Furthermore, the occurrence of jet switching sometimes obscured the effect of the tube displacement as well as effecting the reference pressure used in C_P.

For all array pitches, on the side of the cylinder were tube displacement resulted in increased blockage $(330^o - 360^o)$, there was a drop in pressure with tube displacement.

The contrary was true on the far side of the cylinder. For P/d=1.32 this trend continues until the minimum inter-cylinder gap. As the flow exits the minimum inter-cylinder gap position on the front side of the cylinder (the regions $30^o - 60^o$ and $330^o - 300^o$) it might be expected that a similar flow regime exists. However, the pressure drop observed in the region $330^o - 360^o$ dramatically changes to a pressure recovery and the increase in pressure on the opposite side of the cylinder changes to a pressure drop in the region $30^o - 60^o$. Similar trends emerged for $P/d = 1.58$ for the regions $0^o - 30^o$ and $330^o - 360^o$. There was a drop in pressure on the side of the cylinder with increasing blockage and an increase on the opposite side. For $P/d = 1.32$ the inter-row gap was the pivot point for a change in the flow behaviour on both sides of the cylinder. For P/d=1.58 the inter-row gap only becomes apparent on the side of the cylinder where the gap between neighbouring cylinders was reduced (blockage increased) when the tube was displaced. In this case the transformation region was larger and the change was more gradual. For tube displacements up to 5% there was a long transformation period from approximately $320-290^o$. At the larger displacements $> 5\%$ the transformation occurs as far forward as $\theta = 320^o$ and the pressure recovery was larger. On the opposite side of the cylinder (minimum gap increases) a slight increase in pressure occurs as far back as $60 - 70^o$ from the front of the cylinder was observed.

In an attempt to further understand the pressure data, local flow velocity measurements were made with a single hot-wire probe (see Fig. 5.13 for locations). For $P/d = 1.32$ at $\theta = 270^o$ when the blockage increases with displacement there was an increase in pressure with tube displacement, the flow velocity in this region decreases. This is different to what might be expected; that is, as the gap between neighbouring cylinders reduces the velocity would increase but this does not occur. This would imply that the flow redistribution occurs after the inter-row gap. In fact at position x_1 in Fig. 5.13, the magnitude of velocity measured reduces as the tube was displaced supporting the argument of flow redistribution. This was observed at all the Reynolds numbers tested. On the opposite side of the cylinder the drop in pressure would be accompanied by an increase in velocity in a potential flow but this was not the case implying that non-recoverable pressure losses are occurring in this region. One pos-

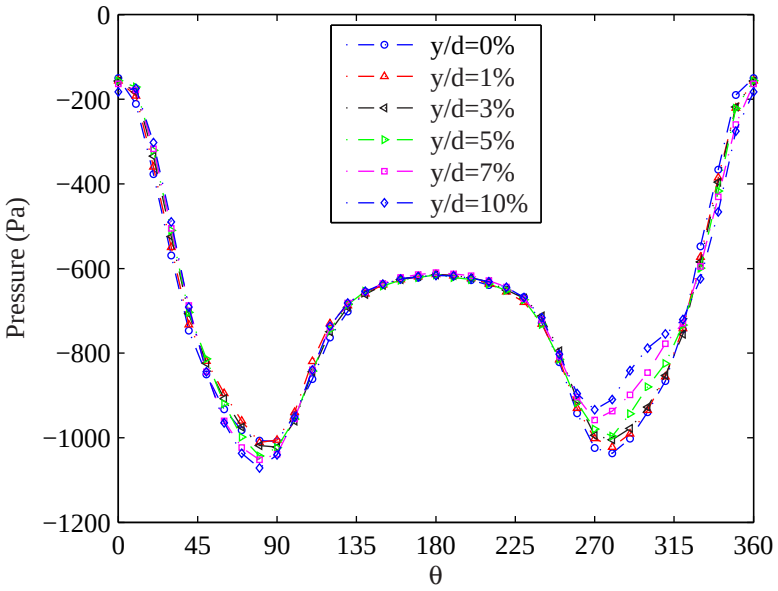

Figure 5.12: P/d=1.58; C_P at various tube displacements, $U = 11m/s$

sible explanation for the non-recoverable pressure losses was the fact that at position x_2, flow velocity increases with reducing blockage on that side of the cylinder. Hence, the mixing effect of the merging streamtubes was greater resulting in additional losses of the non-recoverable type.

As the position angle moves towards $\theta = 110^o$ the trend showing a drop in pressure continues. On the opposite side of the cylinder the pressure recovery continues. At the rear of the cylinder, the pressure increases slightly but the rate at which the pressure increases varies from position to position resulting in the non-symmetric pressure distribution in this region. This is not surprising as there are considerable differences between the distribution at the front and sides of the cylinder as a result of tube displacement and if the distribution remained symmetric at the rear it would suggest that the differences observed at front of the cylinder were not significant which is known not to be the case. Furthermore, the asymmetry at the rear of the cylinder lends weight to the argument that the mass flow rate does not split equally either side of the cylinder when the tube was displaced. Hence, at the rear of the cylinder the flow velocity changes on either side accordingly thus resulting in a smooth transition as the flow merges at the back of the cylinder. This is supported by the lack of an no additional increase in the C'_P at the rear of the cylinder when the tube was displaced.

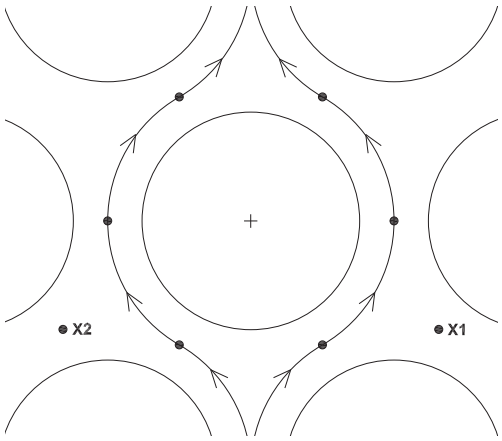

Figure 5.13: Schematic of tube geometry for P/d=1.32 showing the location of local flow velocity measurements

For P/d=1.58, at the minimum pressure ($80^o - 90^o$) a variation in the pressure exists but it appears to fluctuate about a mean value for displacements up to 5%. As the displacement was increased to 7 and 10%, there was a pressure drop at all Reynolds numbers. At the highest Reynolds number tested ($U = 14m/s$) where it was observed that effect of the flow instability was less significant, the variation in pressure was considerably smaller suggesting the larger variation at the other Reynolds numbers was augmented by the flow instability. Irrespective of Reynolds number, the mean pressure at $\theta = 270^o - 280^o$ was found to increase with tube displacement with the largest change in pressure observed in this region. Although at times the trend was broken as a result of the flow instability.

As the position angle tends towards the rear of the cylinder there was a pressure drop after the minimum row gap on the side of reduced blockage. The opposite trend emerges on the far side of the cylinder. This was quite pronounced at some Reynolds numbers. It was likely that this results from the flow instability where generally changes would occur but not to such an exaggerated extent. Further back at the rear of the cylinder, at the lower Reynolds numbers there was an increase in the pressure with increasing displacement similar to that observed for the pitch ratio of 1.32. As the Reynolds number was increased the rate of increase in pressure recovery reduces. At the higher Reynolds numbers ($> 6.6 \times 10^4$) the pressure distribution becomes self-similar. At a comparable Reynolds number a change in the drag force behaviour was also observed suggesting a change in the flow regime and this will be discussed later.

5.2 Flow Instability

The mean pressure distribution for the pitch ratio of 1.58 showed significant asymmetry. When tests were repeated the pressure distribution changed (most noticeably in the region of the minimum gap between neighbouring cylinders) suggesting that the asymmetry distribution was due to flow instability. Similar observations have been reported previously in the literature (for example Zdravkovich & Stonebanks [108], Zdravkovich [109] and others). Further investigation demonstrates that flow instability was the cause. Examination of the time resolved pressure signals (Fig. 5.14), shows that there was significant variation in the pressure. At some positions where the asymmetry was more pronounced, there appeared to be a bi-stable flow regime (jet switching). Further experiments were conducted to examine both the local velocity field and the pressure field. In addition, some rudimentary flow visualisation was performed to further support the findings from both the pressure and velocity data.

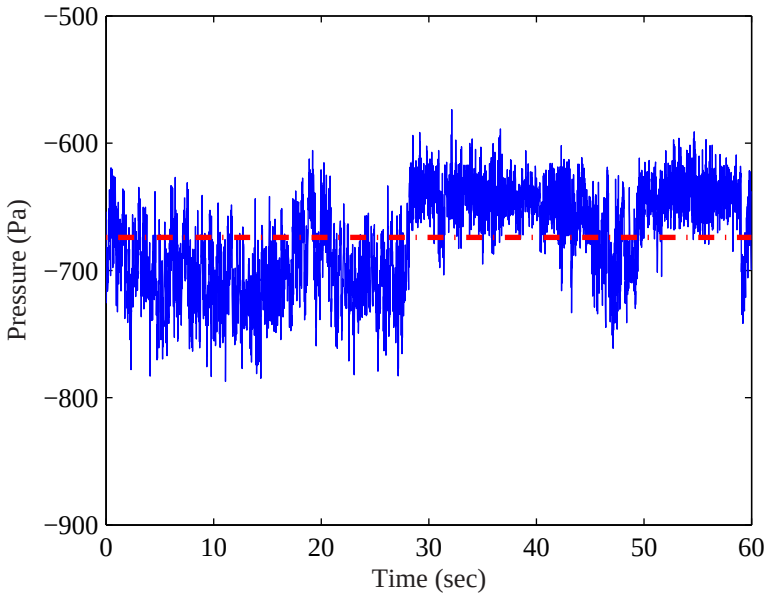

Figure 5.14: Time resolved pressure signal; $y/d = 0\%$ at $\theta = 230^o$

The local flow velocity was measured using a hot-wire probe. Measurements were made at $\theta = 20^o, 70^o, 110^o$ and 160^o and are shown in Fig. 5.15. Two velocity components (u and v) were measured separately (single hot-wire probe used). Seven pressure measurements on surface of the cylinder were also simultaneously acquired. The po-

sition of the pressure measurements (shown in Fig. 5.15) were based on the analysis of earlier experimental results and the positions chosen were some of those positions most affected by the flow instability. For these tests the pressure measurements were used as a control to determine if jet switching occurred or not.

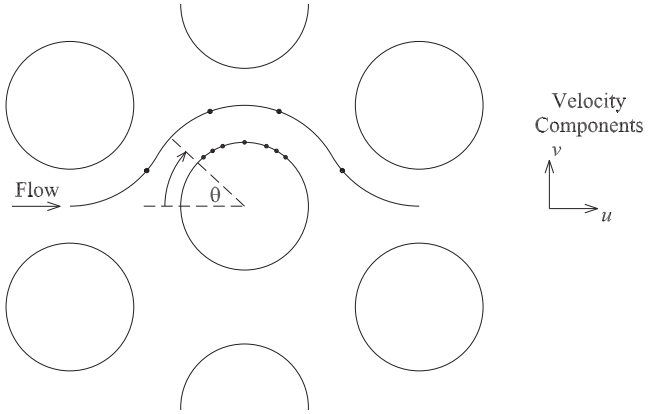

Figure 5.15: Positions of the velocity and pressure measurements

Evidence of jet switching was also found in the local flow velocity. The position and the component of the velocity measurement were important. The first three positions showed variability in the velocity signals consistent with jet switching. An example of the variability is shown in Fig. 5.16 which shows the cross flow local velocity component (v) at $\theta = 20^o$. At $\theta = 20^o$ flow instability was observed normal to the mean flow direction whereas at $\theta = 70^o$ and 110^o flow instability was observed in the mean flow direction whilst no effect was observed at $\theta = 160^o$. This outcome is not unreasonable and is now considered. The measurement positions are on a bisecting line between the measurement cylinder and its neighbouring cylinders as shown in Fig. 5.15. As the flow approaches the cylinder, flow was forced around the cylinder, so a substantial portion of the fluid was flowing in the cross flow direction. Hence, if jet switching was occurring this would explain why the cross flow component at $\theta = 20^o$ sees an effect. As the flow moves around the cylinder the bulk of the fluid motion was in the mean flow direction, hence at $\theta = 70^o$ and 110^o if jet switching is observed, it will be in the in flow velocity component. As the fluid travels back the flow separates and wake region develops with various flow structures enveloped some of which the flow direction is opposite to the mean flow. Thus, changes as a result of jet switching are obscured by the highly turbulent nature of the fluid in this region. This is why no

effect of jet switching was observed at $\theta = 160^o$.

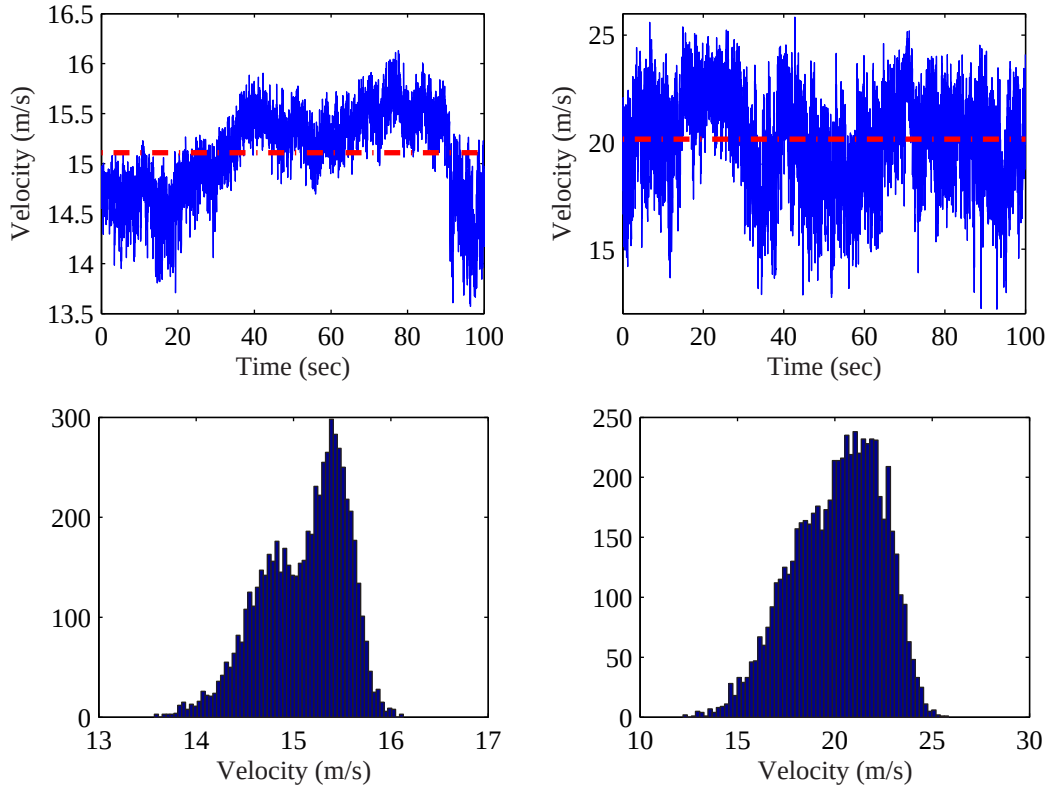

Figure 5.16: Local velocity signal (v); (a) $y/d = 0\%$ and $\theta = 20^o$ (b) $y/d = 5\%$ and $\theta = 70^o$

Jet switching was also captured using flow visualisation. The setup was quite rudimentary, it included a single reflex camera and the flow was illuminated using a photographic lamp (see chapter 3 for details). The flow was seeded using a fog generator. The seeding diffused rapidly because of the highly turbulent nature of a tube array at these Reynolds numbers. The seeding was introduced discretely in front of the instrumented cylinder. The flow visualisation was performed for free stream velocities ranging from 7 - 11m/s as this velocity region showed the most pronounced flow instability. The drawback of measuring at these velocities was that the seeding was convecting and dispersing more quickly, increasing the difficulty in capturing images. Figure 5.17 shows the jet switching observed at a flow velocity of 11m/s. The flow is moving from left to right. In Fig. 5.17(a) the seeding stream moves over the bottom half of the cylinder. The image in Fig. 5.17(b) was captured in the same sequence ($\triangle t \sim 0.2s$). In this case the seeding stream travels around the top of the cylinder.

The occurrence estimate time separation of the flow changing path was not regular as was seen in the pressure and velocity measurements presented above.

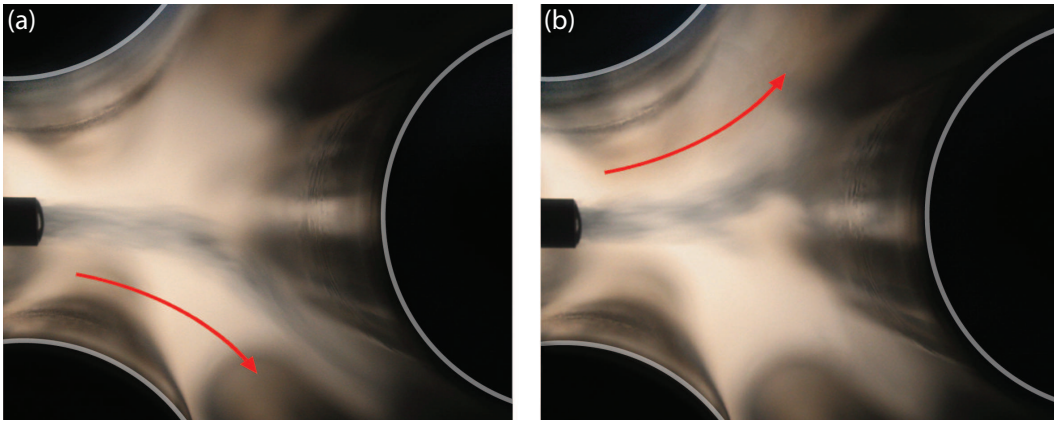

Figure 5.17: Flow visualisation at $U = 11m/s$

Of the studies in the literature that observed flow instability, the array geometry either side of the measurement cylinder was symmetric, as was also the case above. In this situation it is understandable that bi-stable jet switching may occur as the fluid has an equal chance of flowing either side of the measurement cylinder. In the present study, the measurement tube was also displaced in some tests with the tube statically displaced up to $y/d = 10\%$. Most interestingly, the jet switching also occurred even when symmetry was broken (i.e. for non-zero tube displacement) and at all displacements ($y/d = 1 - 10\%$) tested. Figure 5.19 shows the pressure coefficient distribution around a cylinder (P/d=1.58) with the deviation from the mean. Figure 5.18 clearly shows jet switching at $y/d = 5\%$ at a free stream velocity of $11m/s$ and at $\theta = 250^o$. At the largest tube displacement tested jet switching was also observed as shown in Fig. 5.20. The effect of the jet switching was also borne out in the lift force at all tube displacements and is discussed in section 5.3.2. As jet switching was also observed at the largest displacement of $y/d = 10\%$, this might suggest a strong coanda effect in the leeward cylinders. Flow visualisation did not reveal anything to verify this observation but this was not surprising as the jet switching observed using flow visualisation was difficult to capture. It would also appear that the nature of the flow instability changes somewhat at the larger displacements. Examining the pressure distribution with the spread imposed shows that the spread was increased on

the front face of the cylinder (see Fig. 5.19). Examination of the temporal pressure signal as shown in Fig. 5.20 reveals bi-stable flow (jet switching) occurs in this region. As the nature of the fluid in a coanda effect is for the fluid to follow the curvature of the body the fluid is flowing around. It is not unreasonable to suggest that fluid was following the curvature of the leeward cylinders and detaching at some point. When the displacement was small the detached fluid impinges in the region $40-70^o$ and $290-320^o$ and as the displacement is increased this moves towards $\theta = 350^o$. Nonetheless, this was the first time that jet switching has been observed when symmetry was broke. The effect of the jet switching on the vibration behaviour of the single flexible cylinder at the same position will be discussed later.

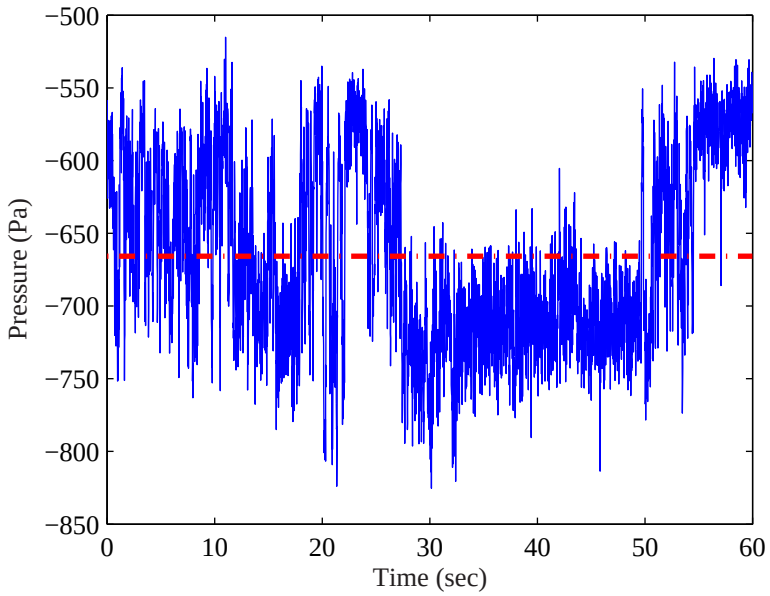

Figure 5.18: Time resolved pressure signal; $y/d = 5\%$ at $\theta = 250^o$

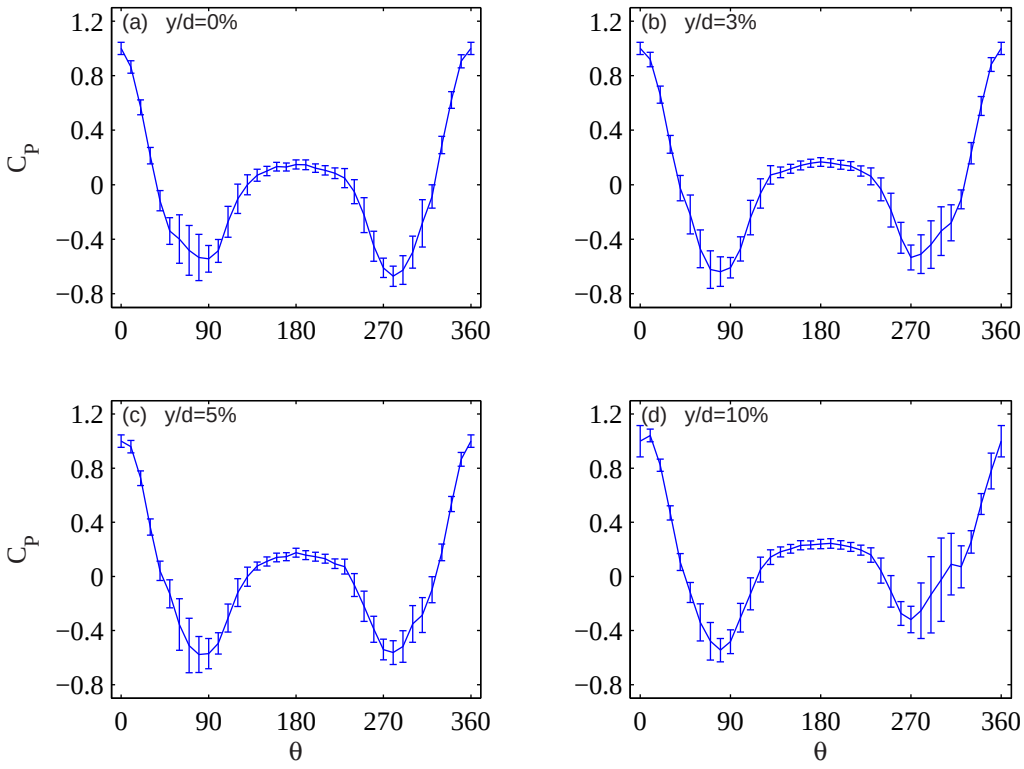

Figure 5.19: C_P at various displacements illustrating the deviation from the mean as a result of flow instability

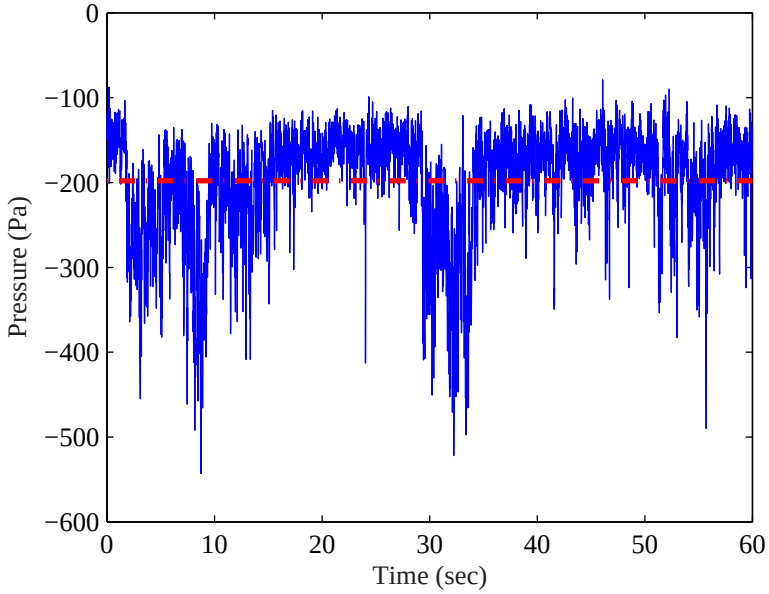

Figure 5.20: Time resolved pressure signal; $y/d = 10\%$ at $\theta = 250^o$

5.3 Fluid Forces

Fluid forces associated with fluidelastic instability are dependent on structural motion. Hence, fluid forces associated with fluidelastic instability on a static cylinder do not exist. However, it is possible to estimate the fluidelastic forces from static measurements made on a displaced body but it must be clear that this is not the same thing. This approach has been employed by many researchers in modelling fluidelastic instability (quasi-steady analysis). In this section the static fluid forces on a cylinder within an array are discussed. The fluid forces were obtained from the surface pressure distribution around the cylinder and are presented in terms of the in flow drag force and the normal lift force. The effect of a static tube displacement within a rigid array on the fluid forces will also be discussed.

Using the pressure data, the drag and lift forces were obtained by decomposing the pressure on the surface of the cylinder into the force contributions in the respective directions at each of the measurement positions. The components were then integrated over the surface of the cylinder to calculate the fluid forces. Eqn. 5.4 was used to calculate the drag force whilst Eqn. 5.5 was used to calculate the lift force on the cylinder. It was reported previously, that there was slight asymmetry in the pressure distribution around $P/d = 1.32$ due to a rotational offset in the position angle. The asymmetry was quantified and accounted when calculating the lift and drag forces and the process is detailed below.

Taking the difference in position angle, $\Delta\theta$, as the difference between the actual 0^o and the measured assumed 0^o. The change in drag, D, and lift, L, as a function of velocity, are ΔD and ΔL, respectively. The equations describing the process are detailed:

$$\Delta D = k(u)\Delta\theta \tag{5.2}$$

$$D = -\int_0^{2\pi} Pdlcos(\theta)d\theta \tag{5.3}$$

However, the offset angle has also got to be considered in 5.3

$$D = -\int_0^{2\pi} Pdlcos(\theta + \Delta\theta)d\theta \tag{5.4}$$

Similarly, the lift force including the offset angle is

$$L = -\int_0^{2\pi} Pdlsin(\theta + \Delta\theta)d\theta \tag{5.5}$$

5.3.1 Drag Force

The drag force on a cylinder in an array is comprised of friction and pressure drag forces. At low Reynolds numbers, the inertia forces are small relative to the viscous forces and friction drag dominates. As the Reynolds number increases, inertia forces dominate to the extent were the contribution from friction drag can be neglected. In the current study the lowest Reynolds number tested was greater than 2×10^4. At these Reynolds numbers the friction forces are small and can be neglected. In the literature, the pressure drag force, D, is presented in terms of drag coefficient, C_D. The drag coefficient has been defined in terms of the in-flow drag force, fluid density (ρ), gap velocity (U_g), tube diameter (d) and tube length (l). The drag coefficient is found experimentally using Eqn. 5.6.

$$C_D = \frac{D}{\frac{1}{2}\rho dl U_g^2} \tag{5.6}$$

Figure 5.21 plots the drag force against the gap velocity for the pitch ratio of 1.32. Note both scales are logarithmic. The data collapses well using a single line indicating that the drag force is directly proportional to the gap velocity and is represented by Eqn. 5.7. Using linear regression, the resultant index, n_1, obtained was 1.67. Note the drag force did not scale proportionally to dynamic head as assumed by models in the literature e.g. Price & Paidoussis [1]. This outcome was not surprising as it was shown in section 5.1.2 that pressure did not generally scale with dynamic head with exception of the front of the cylinder for the higher range of Reynolds numbers tested. When the tests were repeated, it was found that the index obtained fell within 2% of the reported value. Similarly the maximum deviation from the fitted data was less

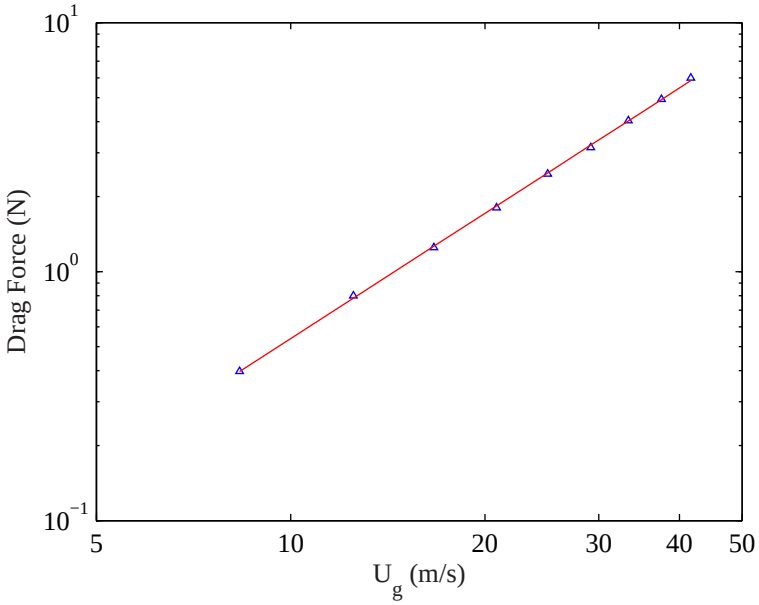

Figure 5.21: P/d=1.32; Drag force, y/d=0%

than 2% illustrating the quality of the fit.

$$D = k_1 U_g^{n_1} \tag{5.7}$$

Inserting Eqn. 5.7 into Eqn. 5.6 gives the gap velocity in terms of non-dimensional drag coefficient.

$$C_D = k_2 U_g^{n_1 - 2} \tag{5.8}$$

Replacing the gap velocity terms with Reynolds number yields:

$$C_D = k_3 Re^{n_2} \tag{5.9}$$

where $n_2 = n_1 - 2$ and Eqn. 5.9 is a fully non-dimensional form illustrating the relationship between drag coefficient and Reynolds number.

When the tube was displaced the system behaved similarly with a line fitting the data sets. Fig. 5.23 plots the extracted indices (in the form of n_2) against tube displacement. The index generally increases with tube displacement. A linear fit was applied to this data ($n_{(y/d)} = 0.00859 \times (y/d) - 0.314$). Using this result the relationship between drag coefficient and Reynolds number for all static tube displacements is formed;

$$C_D = k_{(y/d)} Re^{n_{(y/d)}} \tag{5.10}$$

The constant $k_{(y/d)}$ was obtained by fitting a quadratic curve to the data.

$$k_{(y/d)} = 0.0479 \times (y/d)^2 - 1.56 \times (y/d) + 18.5$$

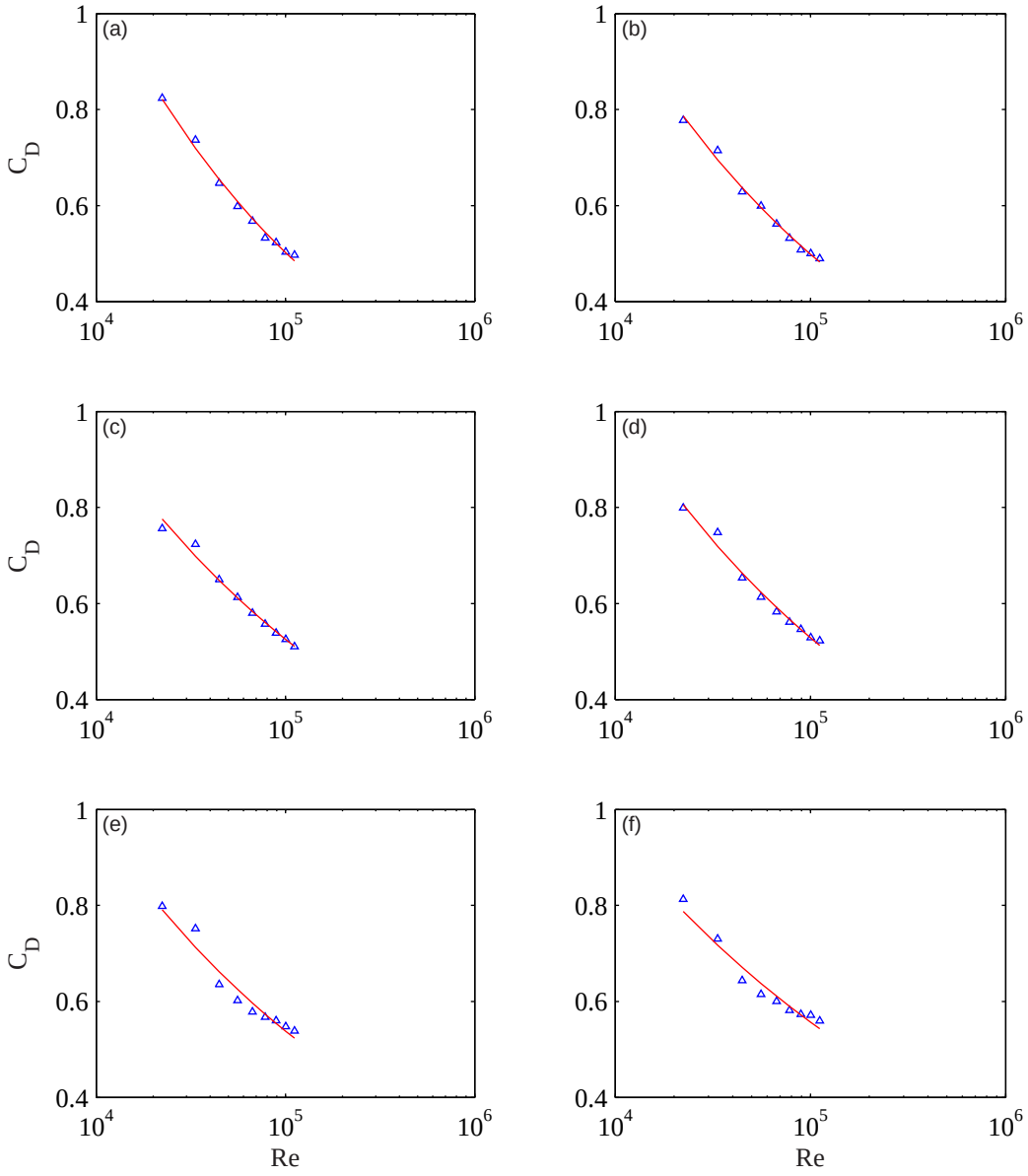

Figure 5.22: P/d=1.32; Drag coefficient against Reynolds number at various tube displacements

For the velocity range tested the effect of tube displacement resulted in a change in the drag force of 12% at most. This suggests that the drag force was only weakly affected by tube displacement. This was investigated further by examining the drag force for a given flow velocity (or Reynolds number) at different displacements. If the

drag force for all displacements at specific flow velocities is examined some interesting results are observed. For the lower flow velocities the effect of tube displacement was minimal with little variation in the force with tube displacement. However, as the velocity is increased, the drag force increases with tube displacement. Further details on this observation can be found in Appendix F.

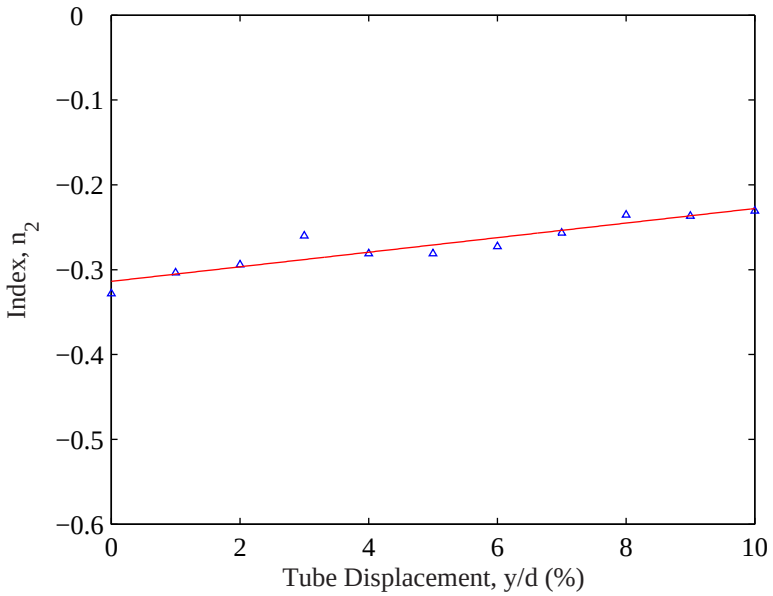

Figure 5.23: P/d=1.32; Index relating drag coefficient and Reynolds number

For P/d=1.58 the randomness in the drag force increased as demonstrated in Fig. 5.24 and was attributed to the jet switching observed in this array. Increasing the duration of the tests and averaging the repeated tests reduced the spread in the data.

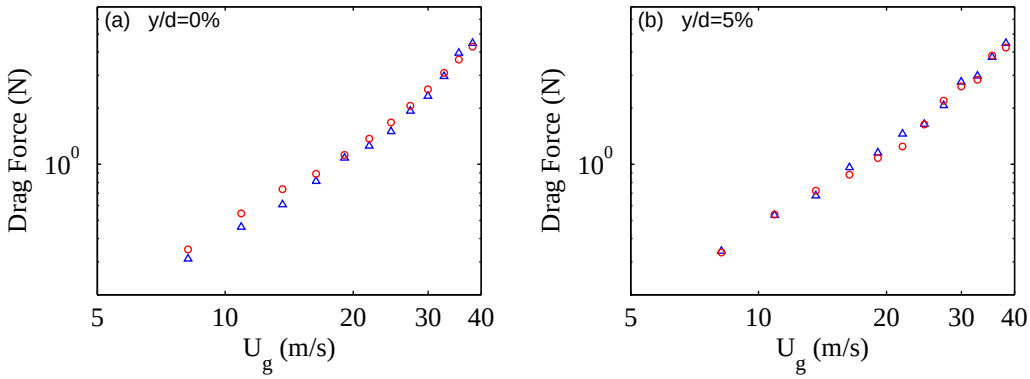

Figure 5.24: P/d=1.58; Drag force: △, Test 1; ∘, Test 2; (a) y/d=0% and (b) y/d=5%

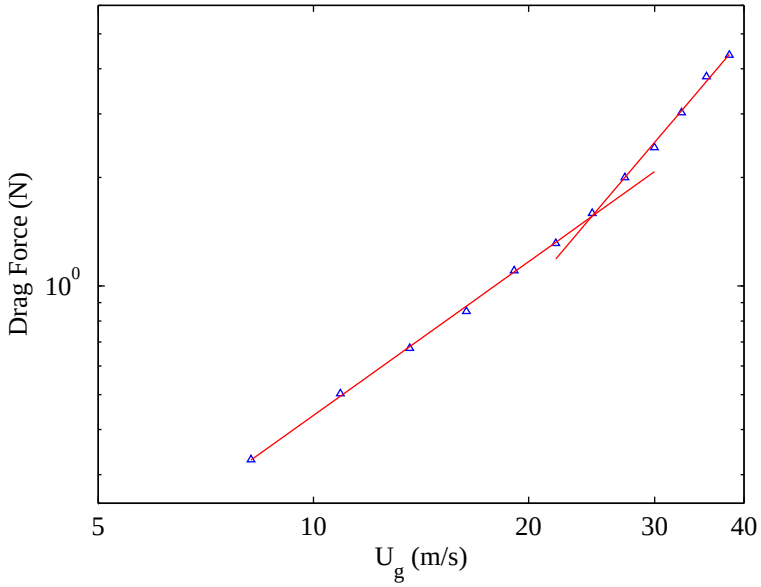

Figure 5.25: P/d=1.58; Drag force at $y/d = 0\%$

Again, the drag force was plot against gap velocity with logarithmic axes. A single line did not fit the data well. A quadratic fit resulted in an improvement at lower Reynolds numbers but was poor at higher Reynolds numbers. In both fits the residuals forces were not random and appeared to take a periodic form illustrating the poor quality of the fits. The data collapsed well using two lines as illustrated in Fig. 5.25. Indices of 1.4 and 2.3 were obtained for the lower and higher Reynolds numbers, respectively. The two lines suggest that there is a transition from one flow regime to another (Re $\approx 6.6 \times 10^4$). This outcome is in agreement with the observations in the literature where its reported that the critical region occurs at lower Reynolds number for tube arrays where the transition region is dependent on array geometry (isolated cylinder, Re $\approx 2 \times 10^5$). When the tube was displaced the system behaved similarly with two lines collapsing the data. However, unlike P/d=1.32 the indices did not increase with tube displacement, they fluctuated about mean values which corresponded to 1.4 and 2.3 as shown in Fig. 5.26. For P/d=1.58 the effect of tube displacement was smaller than the denser array. In addition the most significant changes arising in the pressure distribution from the tube displacement occur at the top and bottom of the cylinder where the contribution to the drag force was small. As it was observed that effect of tube displacement on the drag force was small, the

drag force at all tube displacements was collapsed onto a single plot and was averaged (Fig. 5.27). The resultant indexes obtained where 1.4 and 2.3 for lower and higher Reynolds numbers, respectively. A similar observation was observed for P/d=1.97 and is expanded on in Appendix E.

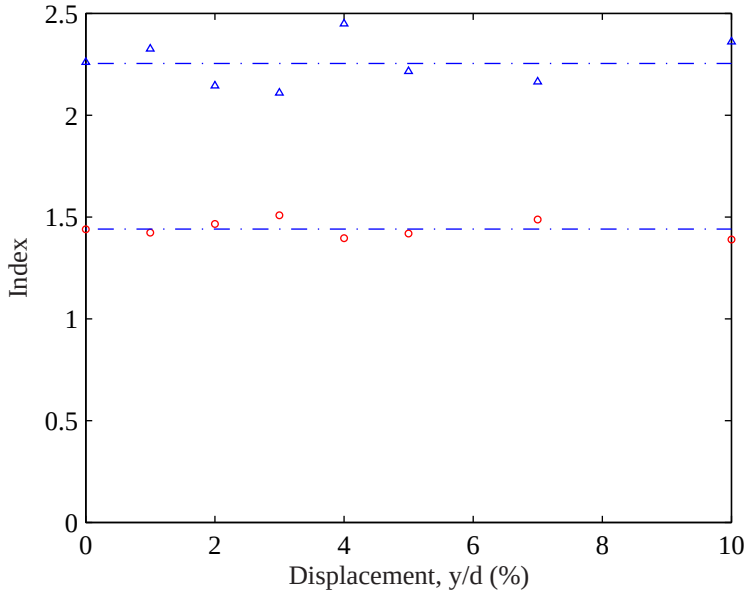

Figure 5.26: P/d=1.58; Index relating drag force and gap velocity; ∘, $U_g < 24.5m/s$, $Re < 6.6 \times 10^4$ and Δ, $U_g > 24.5m/s$, $Re > 6.6 \times 10^4$

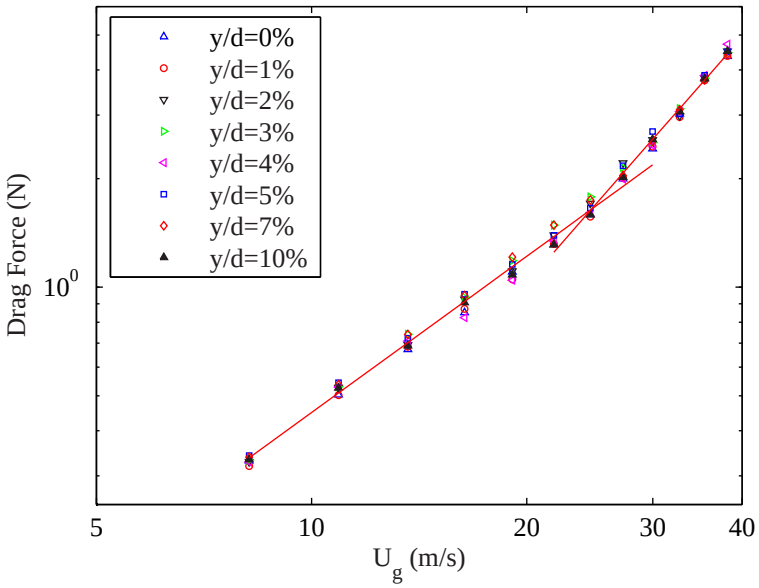

Figure 5.27: P/d=1.58; Drag force at all tube displacements with averaged fitted lines

Using the same approach outlined for the pitch ratio of 1.32, a non-dimensional relationship between drag coefficient and Reynolds number was obtained (Eqn. 5.11). The pitch ratio of 1.58 requires two sets of indices to represent the data above and below Re $\approx 6.6 \times 10^4$ due to the change in behaviour reported above. However, as the effect of tube displacement was small for this pitch ratio the indices can be applied at all tube displacements examined in this study.

$$C_D = kRe^n \tag{5.11}$$

$$Re < 6.6 \times 10^4 \begin{cases} k = 298 \\ n = -0.6 \end{cases}$$

$$Re > 6.6 \times 10^4 \begin{cases} k = 0.0138 \\ n = 0.3 \end{cases}$$

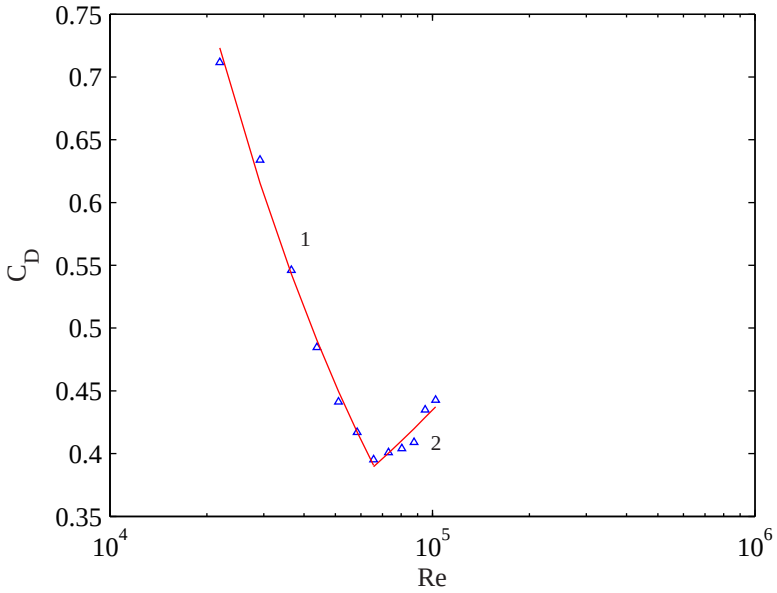

Figure 5.28: P/d=1.58; Drag coefficient averaged at each velocity for all tube displacements

For the pitch ratio of 1.32 the effect of tube displacement on pressure distribution was clearly observable, however, the effect on the drag force was small. In P/d=1.58 the effect of tube displacement was smaller with the bulk changes in pressure at $\pm 90^o$ and the regions fore and aft. However, the contribution to the drag force in these

regions was small. For both arrays it was found that displacing the cylinder changed the pressure distribution at the front of the cylinder where the contribution to the drag force was more significant. However, the changes in pressure were generally not converted into a net change in drag force. Hence, the contribution from the tube displacement to alter the drag force was also deemed to be small as well. These findings suggest that the drag force was largely dependent on the bulk pressure drop across the array and was only weakly dependent on local flow characteristics. It was also apparent that the drag force does not scale with dynamic head with the exception of the sparsest array (P/d=1.97) at higher Reynolds numbers tested (see Appendix E). It was observed that the relationship between fluid forces and flow velocity was dependent on the pitch ratio and Reynolds number.

5.3.2 Lift Force

The lift force for an isolated cylinder is generally assumed to be zero because it is assumed that the flow around the cylinder is uniform and hence no net force in the direction normal to the free stream flow occurs. When the lift force is discussed with regard to a cylinder, it is generally in terms of a fluctuating lift force on an oscillating cylinder or the lift force on a statically displaced cylinder. The lift force is given the same form as the drag force with the drag coefficient term, C_D, being replaced with the lift coefficient term, C_L (see Eqn. 5.12).

$$C_L = \frac{L}{\frac{1}{2}\rho d l U_g^2} \tag{5.12}$$

For P/d=1.32 the lift force around a cylinder in an array at $y/d = 0\%$ fluctuated around zero once the geometrical rotational offset had been quantified and corrected. Once this correction was complete, the lift force appears to be very well behaved. When the tube was displaced, a net lift force in the direction opposite to the tube displacement results. The magnitude of the force generally increased with tube displacement and velocity. This is more clearly observable from Fig. 5.29 which plots the lift coefficient against Reynolds number. C_L increases at the lower Reynolds number range tested. As the Reynolds number is increased further the rate of change reduces and at the higher Reynolds numbers C_L starts to reduce. This occurs at all tube displacements. The rate at which the lift force increases was related to the extent of the tube displacement and the flow velocity and is discussed in Appendix F.

Although the lift force was well behaved, increasing in magnitude with increasing displacement and velocity, no simple parameterisation in terms of displacement and flow velocity was found. Normalising the lift force with respect to various different parameters did not collapse the data. This was because the lift force was far more susceptible to a change in displacement than the drag force. In fact, the lift force increases from $\sim 0.5N$ to $\sim 3N$, when the tube was displaced from $y/d = 1\%$ to $y/d = 10\%$. The upper value of the lift force approximately corresponds to $\sim 40\%$ of the drag force for the same setup and conditions. Unlike, the drag coefficient, the lift force was not as dependent on the bulk pressure drop across the array but was influenced by the local flow characteristics.

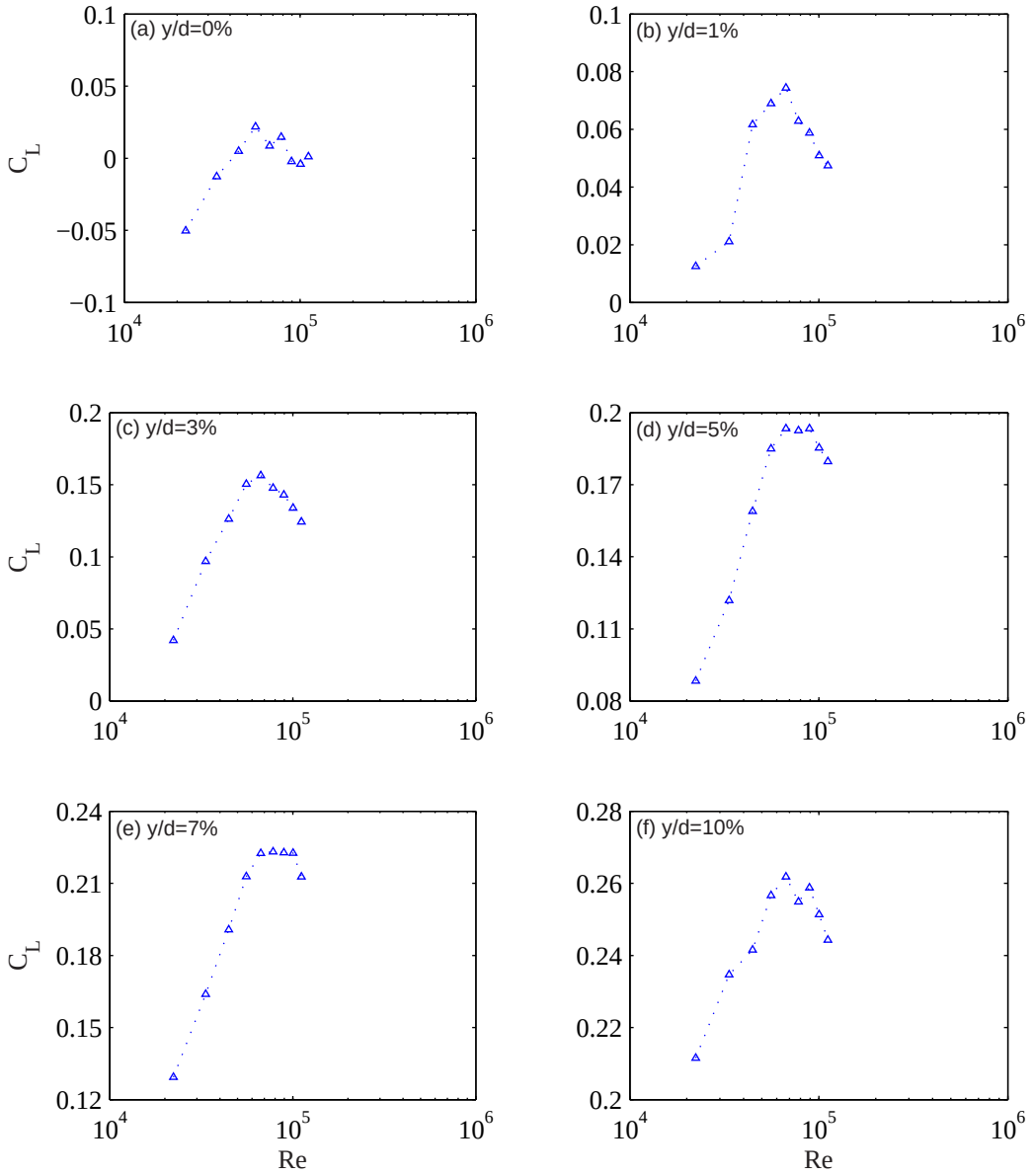

Figure 5.29: $P/d = 1.32$; Lift coefficient against Reynolds number at various tube displacements

The lift force for the pitch ratio of 1.58 was more complex than the pitch ratio 1.32 as a result of the jet switching observed in this pitch ratio. The lift force increased with tube displacement, however on some occasions the force increase was more significant and/or the force was in the opposite direction. When the data is plot in terms of the lift coefficient there is significant scatter for the aforementioned reasons. However, the magnitude of the lift coefficient generally increases with tube displacement as shown in Fig. 5.30. Again no simple parameterisation was found in terms of velocity.

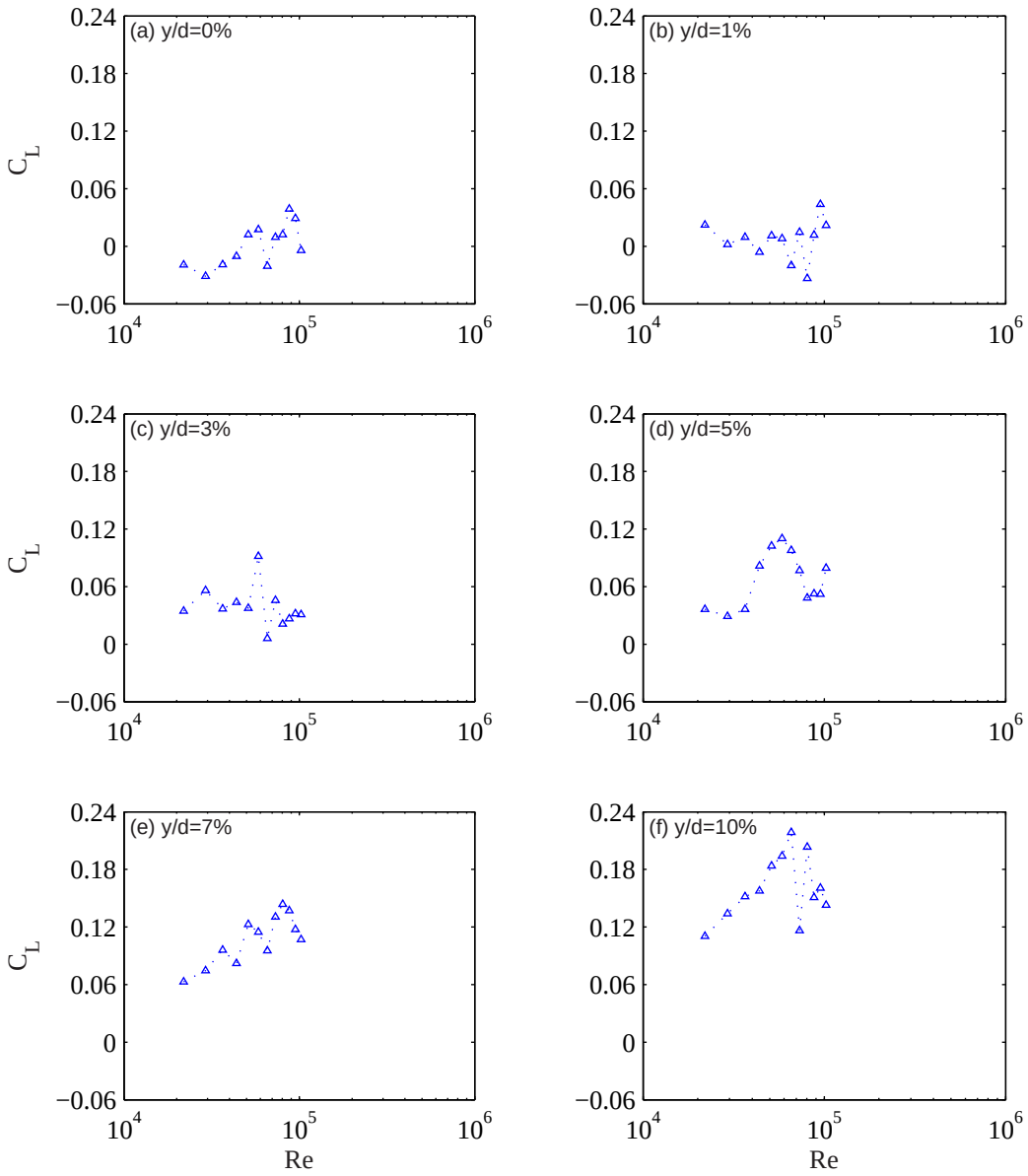

Figure 5.30: $P/d = 1.58$; Lift coefficient against Reynolds number at various tube displacements

It was reported above that no simple parameterisation between lift force and velocity was obtained. In this instance it is clear that the lift force is a function of flow velocity, tube displacement and array geometry (including both array configuration and pitch) and this must be taken into account when including the lift force in models.

5.4 Effect on Fluidelastic Instability

It was shown in section 4.1 that a single flexible cylinder free to oscillate in the lift direction in both P/d=1.32 and 1.58 went unstable due to fluid damping controlled instability. P/d=1.97 on the contrary, did not go unstable due to fluidelastic instability with the vibrations observed attributed to turbulent buffeting.

It was shown that there were differences in the stability thresholds for the two arrays that went unstable due to fluidelastic instability. The more compact array ($P/d = 1.32$) showed a rapid increase in vibration amplitude at the onset of fluidelastic instability whilst the less dense array ($P/d = 1.58$) showed a more gradual change in vibration amplitude as can be seen in Fig. 5.31. The gradual change in vibration amplitude has also been observed in the literature, however, the working fluid was water and in these cases the more gradual change has been attributed to the occurrence of vortex shedding at the same flow velocity. As the current tests are in air, the vortex shedding frequency will be at least an order of magnitude greater than the structural natural frequency, and so this explanation is not applicable. The tube response at ((a), (b), (c) and (d)) a number of flow velocities when the tube motion is considered to be in a post-stable regime were examined to shed light on the behavioural differences of the stability thresholds for the pitch ratios of 1.32 and 1.58. Figure 5.32 shows the tube response signals at (a), (b), (c) and (d). Well established limit cycle amplitudes are observed for the pitch ratio of 1.32 but not for P/d=1.58; the response was dominated by the natural frequency, but the response was more akin to forcing by a narrow band random excitation which could be explained by the jet switching observed (see section 5.2).

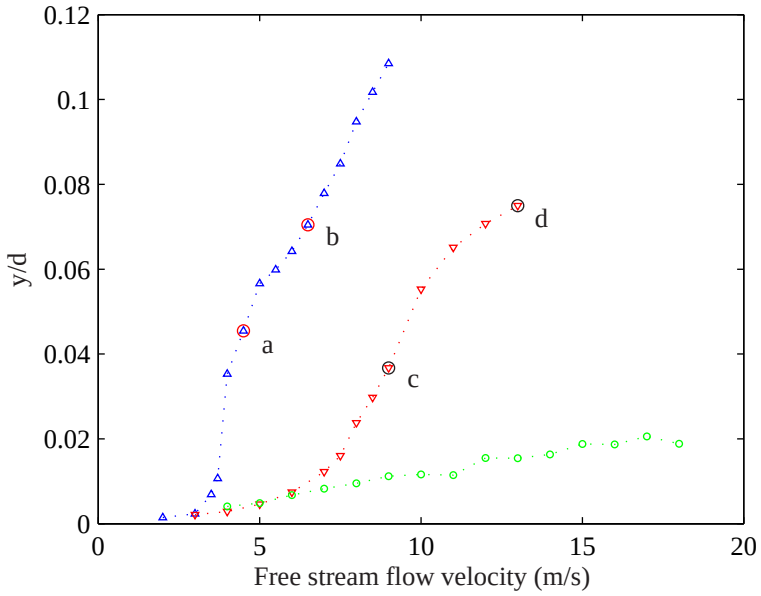

Figure 5.31: RMS of tube motion: Δ, P/d=1.32, $\delta_{st} = 0.123$; ∇, P/d=1.58, $\delta_{st} = 0.030$; $\circ$, P/d=1.97, $\delta_{st} = 0.017$

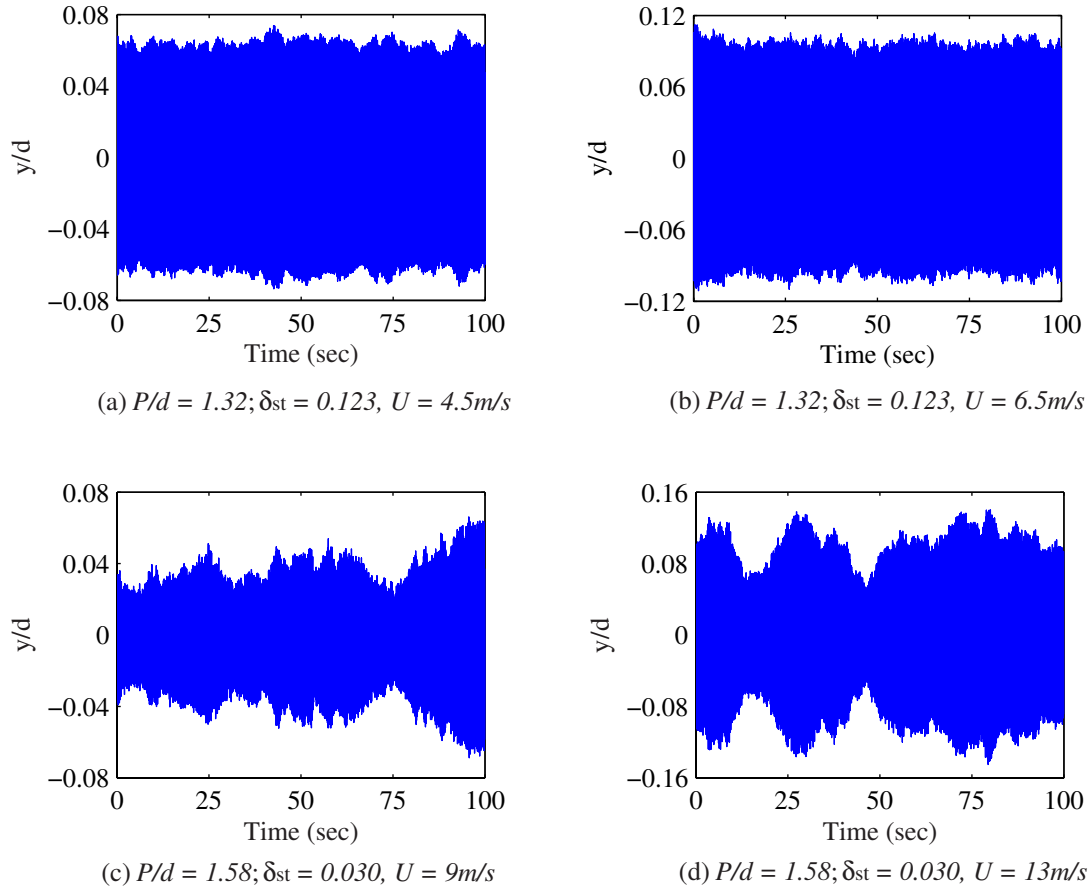

(a) *P/d = 1.32*; δ_{st} = *0.123, U = 4.5m/s*

(b) *P/d = 1.32*; δ_{st} = *0.123, U = 6.5m/s*

(c) *P/d = 1.58*; δ_{st} = *0.030, U = 9m/s*

(d) *P/d = 1.58*; δ_{st} = *0.030, U = 13m/s*

Figure 5.32: Further examination of tube motion from Fig. 5.31

Analysis of the pressure distribution around a static cylinder in the same positions as the threshold tests gives an insight as to why such differences existed between the pitch ratios of 1.32 and 1.58. For the pitch ratio of 1.32, the pressure distribution around the cylinder was relatively symmetric and the flow through the array was regular. The pitch ratio of 1.58 on the contrary showed an asymmetric distribution which was found to change from test to test. Examining the raw pressure data as well as velocity measurements and flow visualisation images indicated that flow instability was occurring in the form of bi-stable jet switching. It was found that jet switching still occurred even when symmetry was broken. It is thought that the jet switching was responsible for producing not well established limit cycles. It is also likely that the occurrence of jet switching resulted in the more gradual change in vibration observed in the stability threshold curves at the onset of fluidelastic instability for the pitch ratio of 1.58. Furthermore, it is likely that jet switching (P/d=1.58) was interfering with the time delay mechanism (convection process) destroying any subtle changes in the process caused by acoustic resonance. Hence, in this array the imposed acoustic field showed no effect on fluidelastic vibration amplitude. Further work is required to explore this hypothesis.

Chapter 6

Interaction between Fluidelastic Instability & Acoustic Resonance Explored

In chapter 4 the interaction between fluidelastic instability and acoustic resonance was captured and quantified. A number of obvious explanations for the observed interaction were examined and discounted. In this chapter two possibilities are examined which are based on the quasi-steady framework proposed by Price & Paidoussis [1] to model fluidelastic instability. In simple terms this separates the fluidelastic force into a magnitude dependent on the static fluid force and a phase component dependent on the time delay.

6.1 Effect of acoustic resonance on static fluid forces

This section examines the effect of acoustic resonance on the surface pressure distribution around a static cylinder in the third row of the array and hence determines if the acoustic resonance alters the force magnitude on the cylinder resulting in the change in vibration amplitude. It was reported in chapter 4 that acoustic resonance was found not to have an effect on fluidelastic vibration amplitude for P/d=1.58, so the discussion in this section is restricted to P/d=1.32. Tests were conducted for a number of flow velocities ($U = 2, 4, 6, 7, 8, 10m/s$); and at a range of tube displacements ($y/d = 0, 1, 3, 5, 7, 10\%$); at various speaker input power (0, 16, 32, 64W). The set up and testing procedure were more rigorously discussed in the previous chapter where the pressure distribution for all three arrays with no forced acoustics was discussed.

At the lower velocities of 2 and 4m/s, acoustic resonance has a small effect on the mean pressure distribution. The pressure distribution at the higher velocities of 6, 7, 8 and $10m/s$ showed a lesser effect as a result of the imposed acoustics. Figs. 6.1 and 6.2 show the mean pressure distribution with and without forced acoustics at the second acoustic mode of the duct.

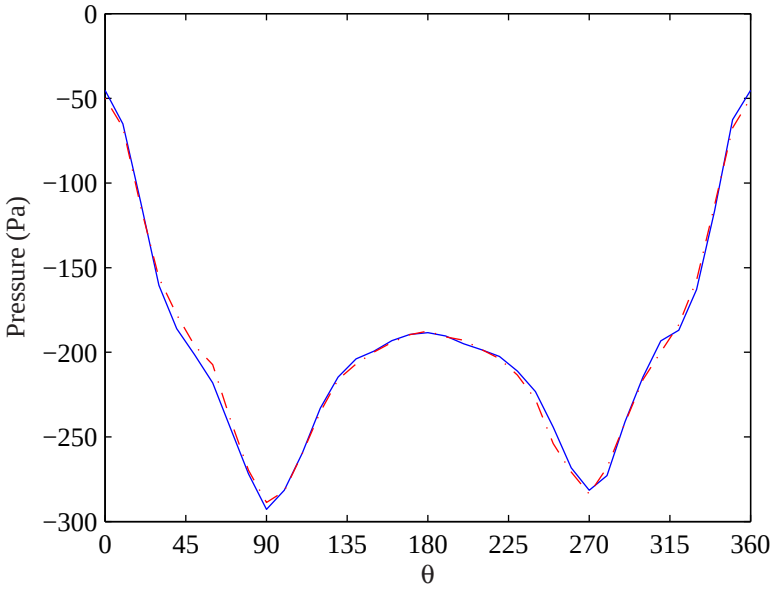

Figure 6.1: Pressure Distribution around at U=4m/s: –, no acoustics; − · −, Frequency=1092Hz (SPL=140dB)

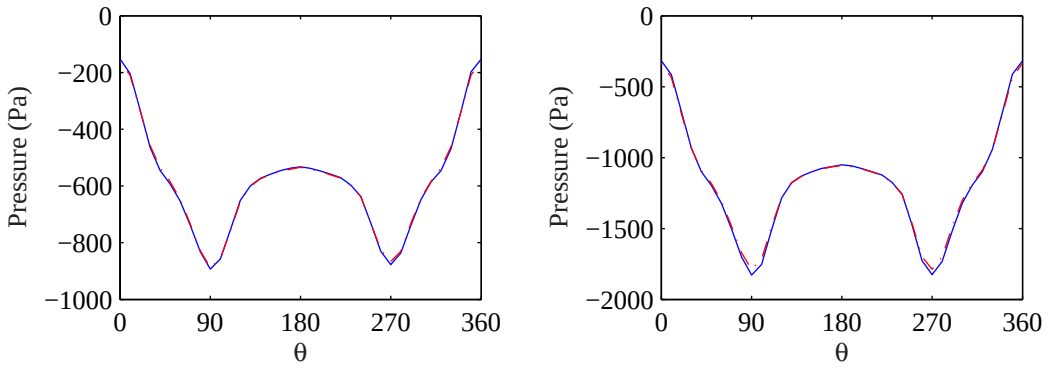

Figure 6.2: Pressure Distribution around at (a) U=7m/s and (b) U=10m/s: –, no acoustics; − · −, Frequency=1092Hz (SPL=140dB)

When the tube was displaced similar findings were observed. The small changes in pressure distribution at lower velocities were not translated into any significant effect on the lift and drag force. Figure 6.3 plots the lift and drag forces at $y/d = 5\%$

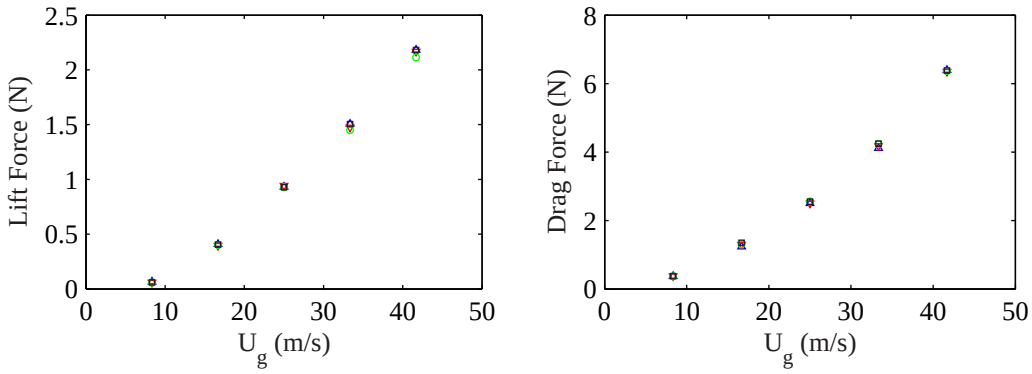

Figure 6.3: Lift and drag force against U_g with and without imposed acoustics. $\triangle$, 0W; ∇, 16W; $\circ$, 32W; $\square$, 64W.

were slight changes in the forces were observed but these were comparable to the random variation in the pressure data. Thus, the effect of the second acoustic mode on the cylinder was minimal, suggesting that acoustic resonance was not affecting the static forces on the cylinder surface. It was also not surprising that as the flow velocity increases, and hence the mean pressure on the surface of the cylinder increases, that the effect of acoustic pressure becomes less significant as the relative magnitude difference (between flow velocity and acoustic particle velocity) increases. A maximum sound pressure level of 140dB was used which corresponds to a pressure of 200Pa. However, it is thought that at higher sound pressure levels that the effect of acoustic resonance on the mean surface pressure would be more significant. For instance, Kacker *et al.* [69] reported that a standing wave (first acoustic mode) of 162dB correlates vortex shedding for a two row tube array whereas 142dB does not. The force experienced increases by a factor of 6. They suggested that the dominant factor of increased force was directly related to the acoustic resonance and that correlated vortex shedding would contribute a force increase of 1.5. Fitzpatrick *et al.* [67] reported on the mean and fluctuating pressure on the surface of cylinders (thirteenth row) in a twenty six row in-line array (P/d=1.73) for non-resonant and artificially excited acoustic standing wave flow regimes. Acoustic resonance substantially altered the pressure distribution on the cylinder. It was reported that acoustic resonance changed the velocity gradients across the array. In fact at non-resonant conditions, velocity gradients across the array were uniform however severe velocity gradients were observed during resonance.

Differences exist between the studies in the literature and work conducted in this study. Firstly, the first acoustic mode was excited and as explained the acoustic particle velocity was a maximum in the center. Furthermore sound pressure levels of 160dB were observed, far in excess of levels reported in this study (140dB). It was shown by Fitzpatrick *et al.* [67] that at sufficient high sound pressure levels the acoustic resonance may alter the velocity gradients across the array thus modifying the force on the cylinder. In the current study, where the sound pressure level was an order of magnitude lower than the studies reported in the literature, the effect on the static fluid force was small. Hence, it is concluded that modification of the static fluid force was not the cause of the observed interaction between fluidelastic instability and acoustic resonance.

6.2 Time Delay

When fluidelastic instability is discussed in the literature, a time delay between the tube motion and the resulting fluid forces is thought to be at the root of fluidelastic instability. The exact nature of the time delay is unclear and has yet to be measured directly. There is some evidence that it exists; Granger & Paidoussis [82] indirectly measured the cause of the time delay using experimental data and a quasi-unsteady model. Abd-Rabbo & Weaver [35] conducted a flow visualisation on rotated square array with P/d=1.41 and water cross-flow. For a single flexible cylinder, flow visualisation "revealed clear flow redistribution with a phase lag". Numerous studies have measured fluid stiffness and damping from which the time delay could be inferred e.g. Tanaka & Takahara [76] and Chen & Srikantiah [83]. There are also a number of models in the literature to model fluidelastic instability. It is apparent that the inclusion of a time delay or phase lag is a prerequisite for the models developed, as without a time delay, the phenomenon cannot be modelled. However, the uncertainty about the origin of the time delay results in different physical explanations for the inclusion of a time delay in the models to predict fluidelastic instability. One of the objectives in this section was to measure the time delay directly. The second objective was to examine the effect of acoustic resonance on the phase dependency component, in the quasi-steady framework proposed by Price & Paidoussis [1]. Explicitly the effect of acoustic resonance on the time delay.

An attempt to measure a time delay between tube motion and a point in the flow located near the flexible cylinder is discussed. In an ideal setup a time delay between tube motion and fluid forces would be measured. This was not achievable due to limitations in the setup. The justification for the current approach stems from the fact that the fluid forces on the cylinder are as a direct consequence of what is happening in the flow around the cylinder. Hence a relationship between the fluid flow and fluid forces are closely related. It would therefore seem reasonable to measure the response of the fluid instead of the fluid force as a first attempt to measure the time delay.

The flexible cylinder was forced to vibrate at its natural frequency of 6.6Hz. This was achieved using the electromagnetic shaker (EMS) system described in sec-

tion 3.1.2.1. The input signal was generated using a HP35665A dynamic signal analyzer via a USA 370 amplifier. The excited vibration amplitude chosen corresponded to 2.5% tube diameter (an RMS value of 1.8%). Using the electromagnetic damper the maximum level of damping achieved was $\delta_{st} = 0.205$. In an effort to reduce the effect of turbulent buffeting additional damping was added. This was achieved by adhering lengths of rubber to the cantilever support. This modification resulted in the damping increasing from $\delta_{st} = 0.205$ to 0.410. At the new level of damping the tube did not go unstable due to fluidelastic instability for the velocity range of the wind tunnel. Tests were conducted for three free stream flow velocities: 4, 7 and 10m/s. The local velocity around the cylinder was measured using a single hot-wire probe. The positions around the cylinder are shown in Fig. 6.4. The local flow velocity was measured at $\theta = 15, 30, 60, 90, 120, 150$ and 165^o in both the in-flow (u) and cross flow (v) directions. Each test was conducted for 15 seconds at a sample rate of 8192Hz. With the excitation frequency of 6.6Hz this translates to 99 averages thus improving the signal-to-noise ratio by a factor of 10.

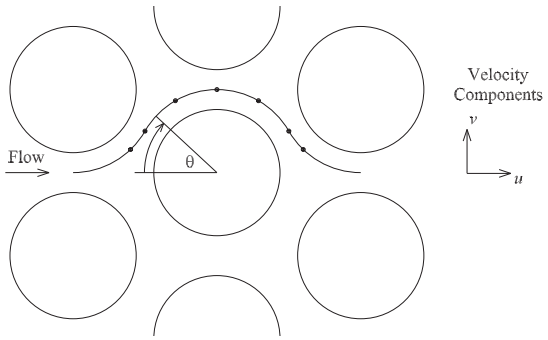

Figure 6.4: Hot-wire positions around the instrumented cylinder

6.2.1 Analysis technique

In the first instance an analysis technique using the cross spectrum between the tube response and the local flow velocity signal was attempted to extract the time delay. However, this approach was limited to due frequency resolution that could be resolved given the test parameters used in the current setup. The cross-correlation between the two signals was also attempted. This provided improved resolution, however, it was not possible rigorously determine the quality of result from cross-correlation. As discussed

below, some of the measurement positions yielded poor results, yet an erroneous time lag could still be extracted. An analysis technique to overcome the issues discussed above will now be expanded on. For each test, tube motion, local flow velocity and the output signal from the amplifier (input signal to EMS) was acquired. This signal from the USA 370 amplifier was used as a reference in the analysis as it produced a clean sinusoid whereas the flow velocity and tube response measurements includes a random component as both were subject to turbulence in the flow. Note, the level of turbulence in a tube array is very high. The reference signal was differentiated using a central difference method;

$$g'(x_0) \approx [g(x_0 + h) - g(x_0 - h)]2f_s \tag{6.1}$$

where f_s is the sample frequency.

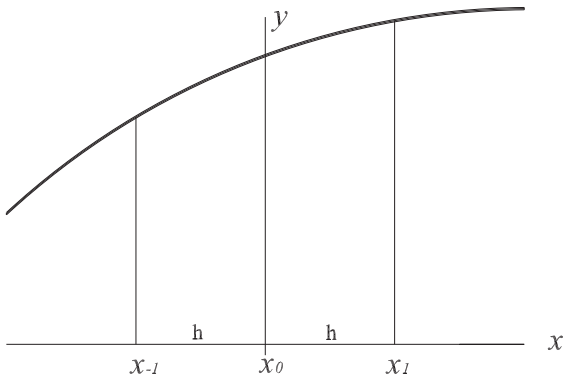

Figure 6.5: Central Difference

The original and differentiated signals were normalised and the inverse tangent taken on the resultant of the normalised original signal divided by the normalised differentiated signal. This process presents the reference signal in the form of an angular position. A snapshot of these signals is shown in Figs. 6.6(a) and (b). The flow velocity and tube motion can now be related to an angular position. As the tube motion was forced using a sinusoid at the natural frequency of the structure it might be expected that this would also be observed in the flow surrounding the cylinder. It can be seen that this is the case but there are significant cycle-to-cycle variations due to turbulence in the flow. The underlying behaviour was extracted fitting a series of harmonic sinusoids:

$$v_M = \sum (A_M \sin M\theta + B_M \cos M\theta) + c \tag{6.2}$$

where v_M is the velocity, θ is the angular position of the reference signal, A_M and B_M are constants. The constants A_M and B_M were obtained using a pseudo-inverse method which yielded a least squares fit for an over determined set of equations (Keays & Meskell [110]).

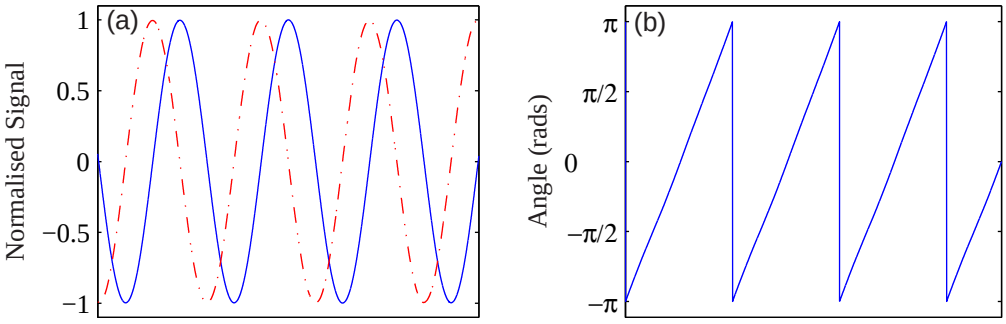

Figure 6.6: (a) –, Original signal; $- \cdot -$, Differentiated signal (b) Angular position

$$\begin{bmatrix} \sin 1\theta_1 & \sin 2\theta_1 & \dots & \sin M\theta_1 & \cos\theta_1 & \cos 2\theta_1 & \dots & \cos M\theta_1 \\ \sin 1\theta_2 & \sin 2\theta_2 & \dots & & & & & \\ \vdots & & & & & & & \\ \vdots & & & & & & & \\ & & & & & & & \\ & & & & & & & \\ & & & & & & & \\ \sin 1\theta_N & \sin 2\theta_N & \dots & \sin M\theta_N & \cos\theta_N & \cos 2\theta_N & \dots & \cos M\theta_N \end{bmatrix} \begin{bmatrix} A_1 \\ A_2 \\ \vdots \\ A_M \\ B_1 \\ B_2 \\ \vdots \\ B_M \end{bmatrix} = \begin{bmatrix} v_1 \\ v_2 \\ \vdots \\ \\ \\ \\ \\ v_N \end{bmatrix}$$

$$\underline{A}\underline{x} = \underline{b} \tag{6.3}$$

$$\underline{x} = \underline{A}^{-P}\underline{b} \tag{6.4}$$

In general:

$$v_1 = A_1 \sin\theta_1 + B_1 \cos\theta_1 + c \tag{6.5}$$

It was found that M=5 was sufficient in all cases on the basis of minimising the normalised error between the fit and the raw data. However, the analysis technique

employed to calculate the time delay between the tube motion and flow reorganisation requires the data to be represented using a single harmonic curve. Figure 6.7(a) and (b) presents the tube motion and flow velocity against angular position, respectively. Also plotted is the respective single harmonic fits and it is observed that the single sinusoid captures the underlying trend in both cases. In some instances the underlying trend was not captured by a single harmonic curve and in these cases the analysis technique cannot be used. The criteria required for the accurate determination of the time delay using the analysis technique is described later in this section.

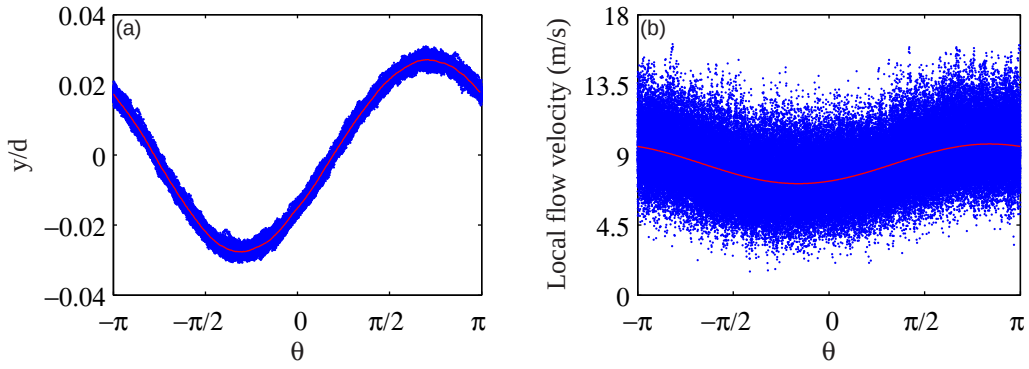

Figure 6.7: First harmonic fit of the tube motion and flow velocity data

If the fits from the tube response and the flow velocity are stripped of the DC information, normalised and plotted together (Fig. 6.8), there is a phase difference between the two traces. Specifically, the flow velocity lags behind the tube response. Hence, there is a time delay between tube motion and the fluid reorganising which would imply a delay in the resultant force on the cylinder. Using the constants A_1 and B_1 the phase with respect to the reference signal for both fits can be obtained by obtaining the $tan^{-1}\frac{A_1}{B_1}$. Subtracting the phases between the two traces yields a phase difference, $\Delta\phi$. This was converted into a time delay, Δt, as the natural frequency is known:

$$\Delta\phi = \omega\Delta t \tag{6.6}$$

where $\omega = 2\pi f$

Rearranging and isolating Δt

$$\Delta t = \frac{\Delta \phi}{2\pi f} \tag{6.7}$$

A time delay of $9.3ms$ was obtained at $U = 4m/s$ and $\theta = 165^o$ with the flow velocity component in the in-flow direction. The sceptic may argue that the measured quantity is not a time delay but the time taken for the fluid to convect downstream. Consider at $U = 4m/s$ this corresponds to a maximum gap velocity of $16.667m/s$. The shortest distance between the cylinder and the velocity measurement position is $\sim 8mm$. This corresponds to a convection time of $0.48ms$. If half the maximum gap velocity is used to calculate the convection time, the time is doubled giving a value of $0.96ms$. This is far less than the 9.3ms obtained. Hence, it would appear that the time delay is that which is related to the reorganisation of the flow field surrounding the cylinder resulting from the tube motion.

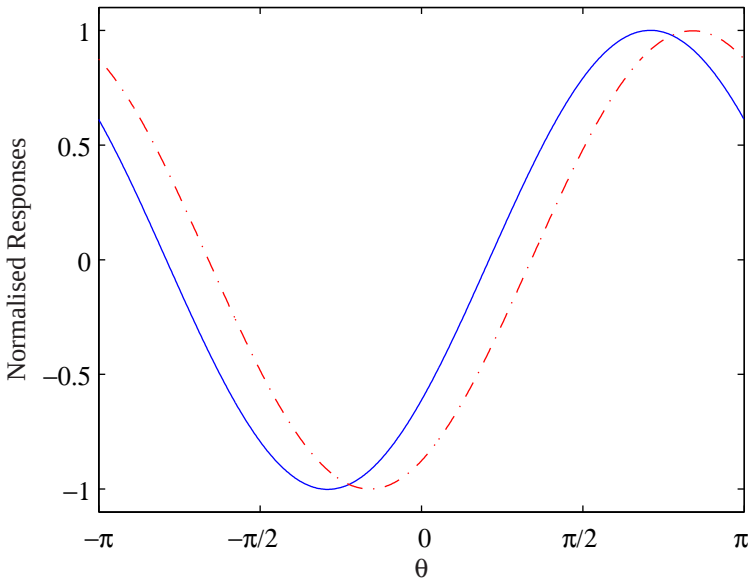

Figure 6.8: $-$, Tube response, and $- \cdot -$, velocity response, showing a time delay between the two traces

The measured time delay was found to change slightly from test to test with the extent of the deviation from the mean varying with measurement position. On average a deviation of $\sim 10\%$ was observed. This is not surprising given that the time delay has been obtained from a measurement in a flow which is highly sheared and turbulent.

It is envisaged that the spread in the measured delay would reduce if the delay was directly measured from the fluid forces on the cylinder. This is likely as the static surface pressure measurements showed smaller deviation from the mean compared to the velocity measurements in the array when all tubes were rigid.

The drawback with this approach is that the tube response and flow velocity data are fit using a single harmonic fit. As the tube was forced to oscillate at its natural frequency using a single harmonic fit yields a good fit. However, the flow field around the cylinder in a tube array is highly sheared and in some positions it was clear that the flow velocity does not respond linearly to the tube motion. Even where the fit was good there was considerable spread from the fitted sinusoid due to large fluctuating velocities caused by the turbulence structures. Also separation regions and shear layer positions will fluctuate compounding the problem. In those instances where the fit was poor it was not possible to accurately measure a time delay as this process was highly reliant on the data being fit using a single harmonic curve. It is therefore important to consider how the quality of the fit was determined. This was determined using a number of criteria. It would be incorrect and highly subjective for one to determine the quality of the fit by visual means. The approach used in this study examined the energy contribution at each harmonic in conjunction with the auto-correlation between the actual data less the first harmonic fit.

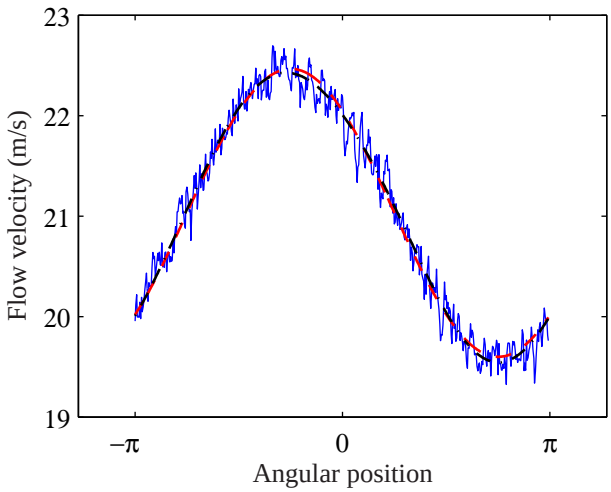

Figure 6.9: Ensemble averaged velocity $\theta = 165^o$, u - dir; $--$ (red), 1st Harmonic fit; and $- \cdot -$ (black), Harmonic fit (inclusive of 3rd harmonic)

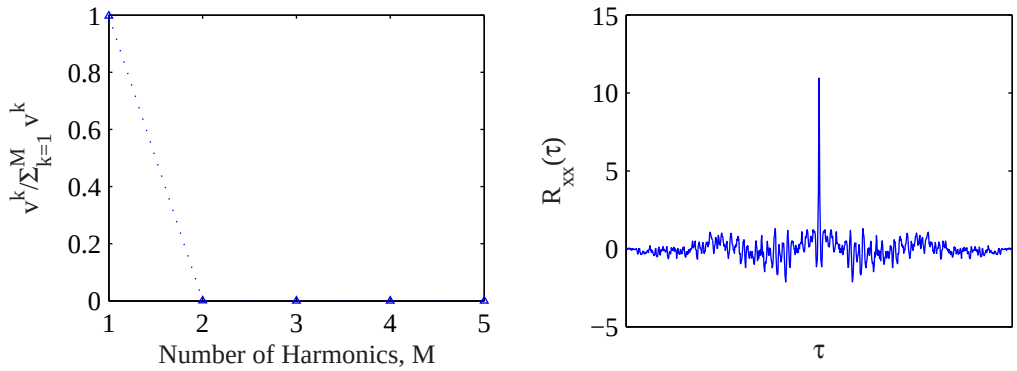

Figure 6.10: Good Fit: $\theta = 165^o$, u-dir and $U = 10m/s$; (a) Energy distribution at each harmonic (b) Auto-correlation

A good fit was deemed to have been achieved when the energy distribution at the first harmonic was greater than 95% as illustrated by Fig. 6.10 (a). Below that threshold the fit was deemed to be not of the base line quality. The second criteria also had to be satisfied. This involved examining the auto-correlation of the raw data less the fit of the first harmonic. If the fit was good random noise should be all that remains. Viewing the auto-correlation of this signal determines if the resulting distribution was random or if it contained periodic artifacts. A delta function is representative of random noise (see Fig. 6.10(b) $\theta = 165^o$, u-direction). However, if the periodic artifacts are present the auto-correlation also takes a periodic form. As noise (turbulence) was also present this results in the correlation diminishing see Fig. 6.11 (b).

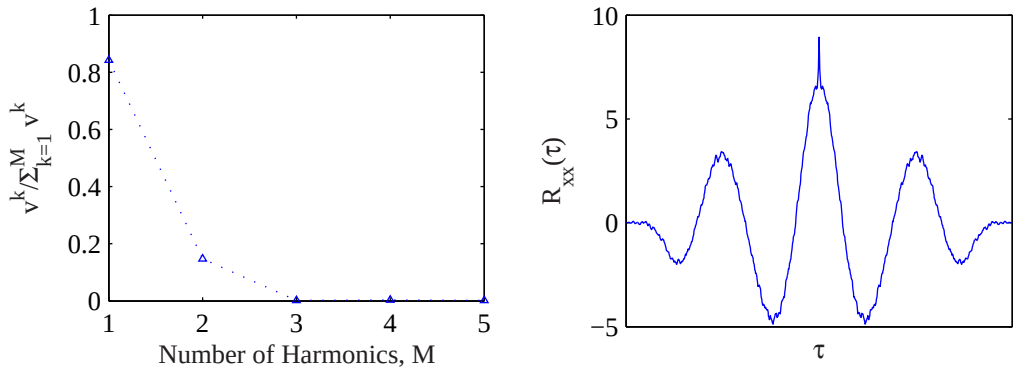

Figure 6.11: Poor Fit: $\theta = 150^o$, v-dir; (a) Energy distribution at each harmonic ($U = 4m/s$) (b) Auto-correlation ($U = 7m/s$)

The fits judged to be of acceptable quality level are presented in Table 6.1 with the measured time delays. Although the single harmonic fit was poor at some measure-

ment positions, it was observed using the qualitative approach described earlier that a delay between tube motion and the flow reorganisation resulted but this could not be quantified.

When the time delay is discussed in the literature, researchers refer to it as a single quantity, which in the case of Granger & Paidoussis [82] was shown not to be instantaneous. In this study the time delay was found to change with the measurement location around the cylinder. There was no definitive trend relating the time delay with measurement position but it does appear that it was smaller at the front of the cylinder and increases at the rear. However, the largest delay was observed at side of the cylinder ($\theta = 90^o$) in the in flow direction. The difference in the time delay at various positions is not unreasonable as the diffusion-convection of vorticity would also be evolving at different rates around the cylinder. However, it is not clear if this result would be replicated if the pressure on the surface of the cylinder was measured instead of the velocity at the point measurements. Further work is required to explore this effect but was beyond the scope of the current study.

Position	$U = 4m/s$	$U = 7m/s$	$U = 10m/s$
15^o (v -dir)	3.0	3.5	4.4
30^o (u -dir)	5.1	3.4	3.5
30^o (v -dir)	6.6	4.9	5.8
90^o (u -dir)	42.0	52.4	-
150^o (u -dir)	-	5.5	4.6
165^o (u -dir)	9.3	7.9	7.0
165^o (v -dir)	10.3	8.8	8.0

Table 6.1: Time Delay (ms) at a range of positions in the flow field

Another approach to measure the time delay between tube motion and the flow field was attempted with no harmonic fitting of the data. This was achieved by not forcing a sinusoidal response but by displacing the cylinder by a similar distance in a short time ($\sim 1ms$). Effectively, the indicial response of the coupled fluid structure system was measured. The electromagnetic shaker was replaced with a solenoid. However, the force produced by the solenoid was large and the tube overshot with a resulting transient motion. A number of suppression measures such as using additional damping, rubbing plates, stopping blocks and reducing the applied force reduced the

transient effects somewhat but not sufficiently. To better resolve this issue the twin beam support set up would need to be replaced with a system designed specifically for this type of test.

It is also envisaged that the measurement on the surface of the cylinder (pressure) rather than in the flow would result in a cleaner response, facilitating improved measurements for both approaches outlined above to measure the time delay. It is likely that the step response would be the better approach as it would not only quantify the time delay but would also give rise to a function similar to the memory effect proposed by Granger & Paidoussis [82].

6.3 Effect of acoustic resonance on the Time Delay

A number of attempts to explain the interaction between fluidelastic instability and acoustic resonance have been discussed and discounted by experimental tests. It has been reported in the literature that there is a time delay between tube motion and the resulting fluid forces. The current study has measured a time delay of sorts, by measuring the flow around a cylinder in response to tube motion. Andjelic & Popp [84] showed the importance of a time delay, comparing their experimental data with the "wavy wall channel model" developed by Lever & Weaver [85]. Andjelic & Popp found that the fit between the analytical curve and experimental data was poor. Modifying the time delay resulted in a much better fit. As it was observed that the stability threshold was modified with acoustic resonance (AR), it is possible that acoustic resonance interferes with the time delay. The time delay between tube motion and flow velocity at a number of positions around the cylinder with and without acoustic resonance was measured.

	$U = 4m/s$		$U = 7m/s$		$U = 10m/s$	
Position		AR		AR		AR
15^o (v -dir)	3.0	0	3.5	3.7	4.4	2.3
30^o (u -dir)	5.1	1.4	3.4	5.7	3.5	3.6
30^o (v -dir)	6.6	0	4.9	5.4	5.8	0
90^o (u -dir)	42.0	45.9	52.4	51.1	-	-
150^o (u -dir)	-	-	5.5	9.1	4.6	3.4
165^o (u -dir)	9.3	7.9	7.9	8.1	7.0	6.0
165^o (v -dir)	10.3	8.1	8.8	9.1	8.0	6.8

Table 6.2: Time Delay (ms) at a range of positions in the flow field with and without acoustic resonance. Shading - illustrates the hot-wire positions and velocities where overlap between the individual time delays measured with and without forced acoustics occurs

The series of tests discussed in section 6.2 were extended to measure the time delay with forced acoustics and each test was repeated five times. Tests were repeated for other flow velocities and also the other hot-wire positions. It was discussed previously that the measured time delay was found to wander slightly from test to test. The average (five tests) time delays with and without acoustic resonance are summarised in Table 6.2. In some instances a change in time delay with forced acoustics occurred but

there was an overlap between the individual time delays measured with and without acoustic resonance. These are denoted by the shading in Table 6.2. In these instances no conclusive outcome as to the influence of acoustic resonance was realised. However, at the other positions a definitive phenomenon emerged: the acoustic resonance modified the time delay. In some instances the time delay was increased; more often the time delay was reduced. The reduced duration of the time delay resulting in a reduction in tube oscillation is in agreement with the model proposed by Price & Paidoussis [1]. Furthermore, the proposition that modification of the time delay shifts the stability threshold is in agreement with the conclusions of Andjelic & Popp [84] which were based on experimental considerations. Further work is required to explore this result but this can only be rigorously examined when the time delay between tube motion and fluid forces is measured.

Assuming that acoustic resonance modifies the time delay, how could this process be justified physically? Granger & Paidoussis' [82] formulation of a memory effect (cause of the time delay) refer to vorticity generated on the surface of the cylinder resulting from tube motion. This vorticity is diffused and convected downstream by the mean flow. When the vorticity is convected far enough downstream a new steady state is reached. It was shown that the effect of acoustic resonance on the static fluid forces was negligible (i.e. the vorticity generation process). So, as acoustic resonance was observed to have modified the time delay it must be interfering with the vorticity diffusion-convection process. In Figs. 6.12 and 6.13 it was also observed that the acoustic resonance shifted the mean velocity (both increasing and decreasing) at some positions as well as the form of the distribution with reference to the angular position of the tube vibration. This is curious, as at the current tube position the acoustic particle velocity corresponds to a minimum in this region. In this instance it appears that acoustic resonance is causing streaming. It is not unreasonable to suggest that the acoustic streaming may be interfering with the diffusion-convection of vorticity process from the surface of the cylinder suggested by Granger & Paidoussis.

It has been shown that acoustic resonance effects fluidelastic instability and this has been quantified. Acoustic resonance does not change the static fluid force. It has also been shown that at some hot-wire (local flow velocity) positions a definitive

change in the time delay between tube motion and the flow field around the cylinder emerged as a result of acoustic resonance. It is also clear that acoustic resonance modifies the mean velocity at some positions in this region where it is thought this results from acoustic streaming. Further work is required to further explore the time delay mechanism and hence the effect of acoustic resonance on it.

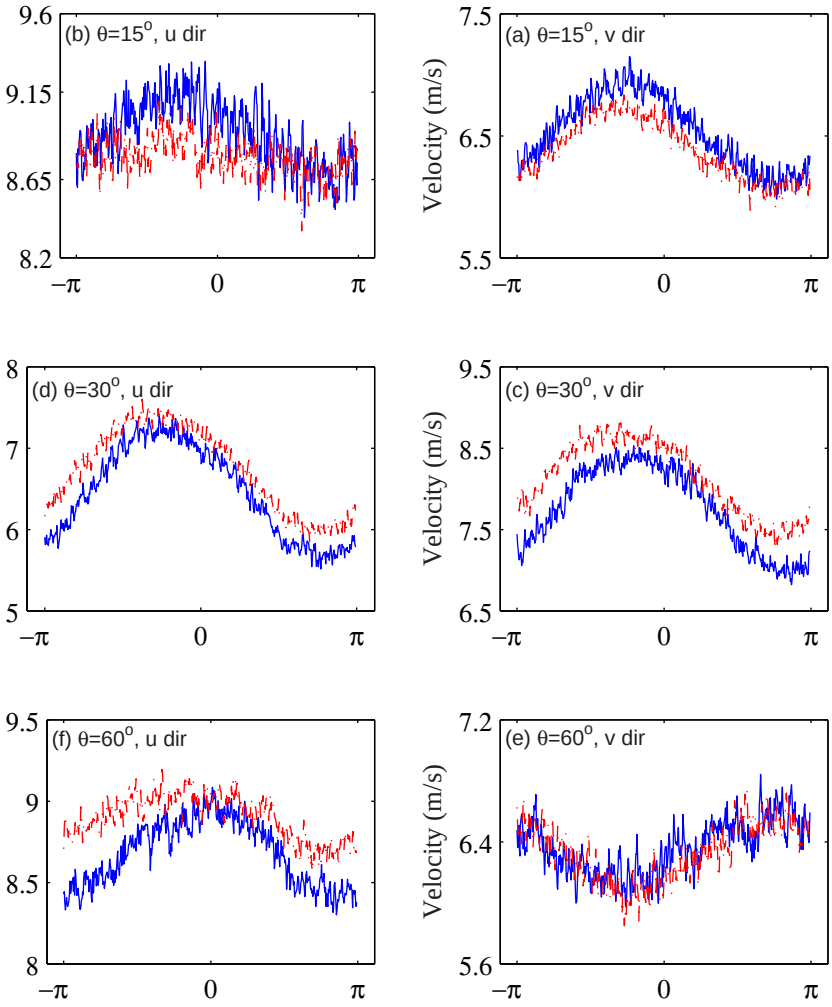

Figure 6.12: Ensemble averaged Velocity data: – (blue), without acoustic excitation and – · – (red), with artificially excited acoustic resonance (speaker power = 64W)

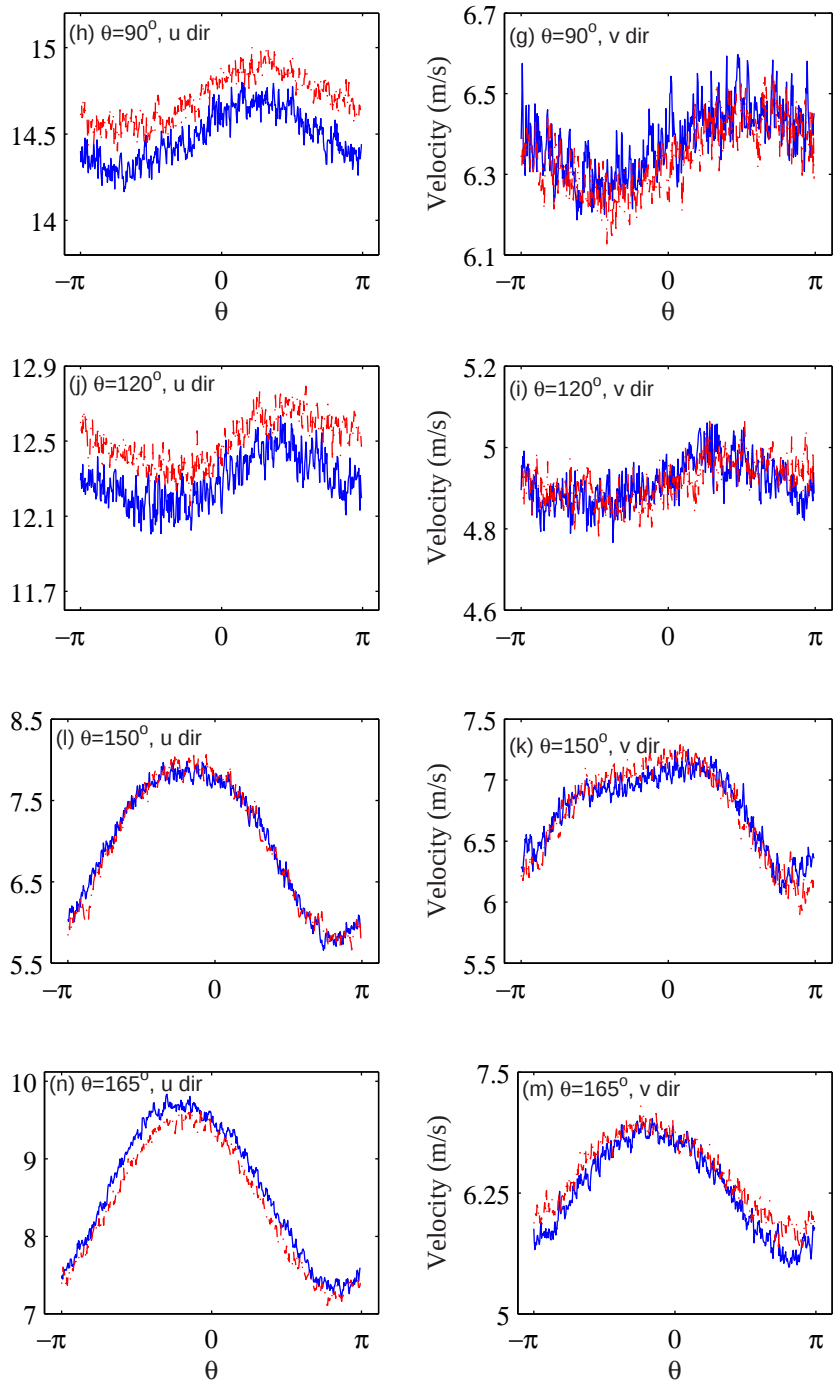

Figure 6.13: Ensemble averaged Velocity data: – (blue), without acoustic excitation and – · – (red), with artificially excited acoustic resonance (speaker power = 64W)

Chapter 7

Conclusion

An investigation into the interaction between fluid damping controlled instability and acoustic resonance in normal triangular tube arrays with pitch ratios of 1.32 and 1.58 has been investigated. This was achieved by experimental means. A single flexible cylinder was free to oscillate in the cross flow direction only. The duct acoustics were excited with speakers placed adjacent to the tube array to artificially replicate flow-induced acoustic resonance (second acoustic mode). It was observed that the imposed acoustic field showed no apparent effect on the vibration amplitude for the pitch ratio of 1.58. For the pitch ratio of 1.32 acoustic resonance modified fluidelastic vibration amplitude, increasing the critical flow velocity, delaying the onset of fluidelastic instability. In a post stable regime, a drop in the amplitude of tube vibration was observed with increasing sound pressure level of the acoustic resonance. In terms of the system dynamics, it has been shown that acoustic resonance adds positive damping, reducing the apparent negative fluid damping associated with fluidelastic instability.

Using the quasi-steady framework proposed by Price & Paidoussis [1] to model fluidelastic instability, two possibilities were examined to explain the interaction between the two phenomena. The first examined the steady effects, i.e. the effect of acoustic resonance on the magnitude of the static fluid forces. It was observed that static fluid forces were not affected by the imposed acoustic field (SPL$\approx$140dB). The second possibility examined the phase dependency of the fluidelastic force. This required the measurement of a time delay between tube motion and fluid forces. In the current setup a time delay between tube motion and a point in the flow was measured. Acoustic resonance was shown to modify the time delay associated with

fluid damping controlled instability at some of the measurement positions (around the measurement cylinder). It is proposed that acoustic streaming was interfering with the diffusion-convection of vorticity process detailed by Granger & Paidoussis [82]. However, additional testing is required to better explore this hypothesis.

In addition, some baseline surface pressure measurements for a tube in the third row of three normal triangular tube arrays have also been conducted with various static displacements applied to the tube. This data provides a valuable reference for validation of simulations of fluidelastic instability in staggered arrays.

The fluid forces did not scale proportionally to dynamic head as assumed by models in the literature. It was found that the fluid forces which are related to fluidelastic instability are dependent on Reynolds number and pitch ratio. A non-dimensional relationship between drag coefficient and Reynolds number was found for all three arrays. For P/d=1.32 the equation included tube displacement. This was not required for the other pitch ratios as the effect of tube displacement was small. However, the change in flow regime observed for P/d=1.58 and 1.97 resulted in different indices and constants for lower and higher Reynolds number ranges. For all array pitches tested no simple parameterisation was found for the lift force as it was observed to be highly dependent on the flow velocity, array geometry and tube displacement.

A jet switching phenomenon was also observed in the pitch ratio of 1.58. It is possible that the jet switching interfered with the time delay mechanism resulting in the more gradual change in vibration at the onset of fluidelastic instability and the poorly established limit cycle amplitudes. It is also likely that jet switching interfered with the time delay mechanism destroying any subtle changes caused by acoustic resonance. Further work is required to explore this hypothesis.

7.1 Future Work

From the conclusions drawn in this testing programme it is apparent that more work is needed to understand the fluid dynamics underlying fluidelastic instability but also the interaction with acoustic resonance.

To fully explore the physical mechanisms responsible for fluid damping controlled instability an improvement in the technique to measure the time delay is required. It is not possible to measure a time delay at all positions in the flow field due to the highly sheared nature of the flow field and the process used to determine the time delay. The setup and process used could be improved upon by a two pronged approach. Firstly the measurement of the fluid forces on the cylinder as opposed to the flow velocity, would be a more appropriate measure of the time delay. The force measurements would be based on the measurement of the pressure distribution on the cylinder undergoing sinusoidal vibration. This would require calibrating and adapting the pressure transducers and pressure tapped cylinder for dynamic measurements. This would not only quantify the time delay in terms of fluid force but would identify the regions of relevance. The second approach would re-examine the idea of displacing the cylinder by a small distance in a finite time (i.e. step response). This would require the modification of the twin beam support setup or more preferably the design of a new support which would enable the tube to be displaced in a finite time without the adverse effects of a transient decay at the cylinders new position. This approach would not only measure the time delay but would illustrate the transition process from one steady state position to the next with the possibility of validating the framework of Granger & Paidoussis [82].

Using both the improved time delay measurement techniques as well as the full field velocity measurements would further clarify the relationship between the time delay and acoustic resonance. In addition, the full field velocity measurements would help identify if acoustic streaming was interfering with the convection-diffusion of vorticity process.

Bibliography

[1] S J Price and M P Paidoussis. An improved mathematical model for the stability of cylinder rows subject to cross-flow. *Journal of Sound and Vibration*, 97(4):615–640, 1984.

[2] R Austermann and K Popp. Stability behaviour of a single flexible cylinder in rigid tube arrays of different geometry subjected to cross-flow. *Journal of Fluids and Structures*, 9:303–322, 1995.

[3] S J Price and M L Zahn. Fluidelastic behaviour of a normal triangular array subject to cross-flow. *Journal of Fluids and Structures*, 5:259–278, 1991.

[4] A Zukauskas. Cylinders in crosflow. *High-Performance Single-Phase Heat Exchangers, Hemisphere Publishing Corporation*, Chapter 10:187–206, 1989.

[5] S Ziada and A Oengoren. Vortex shedding in an in-line tube bundle with large tube spacings. *Journal of Fluids and Structures*, 7:661–687, 1993.

[6] S Ziada, A Oengoren, and E T Buhlmann. On acoustical resonance in tube arrays. part i: Experiments and part ii: Damping criteria. *Symposium on flow induced vibration and noise*, pages 219–254, 1989.

[7] S Ziada and A Oengoren. Flow periodicity and acoustic resonance in parallel triangle tube bundles. *Journal of Fluids and Structures*, 14:197–219, 2000.

[8] M. Paidoussis. Flow-induced vibrations in nuclear reactors and heat exchangers. practical experiences and state of knowledge. *In E. Naudascher and D. Rockwell (Eds.), Practical experiences with flow-induced vibration*, pages 1–56, 1979.

[9] A Adobes, J Pillet, F David, and M Gaudin. Influence of steam generator tube bundle vibrations on the operating diagram of a nuclear plant during strech out. *ASME PVP, Flow Induced Vibrations*, ICPVT-11(93239):1–10, 2006.

[10] C Meskell and J A Fitzpatrick. Investigation of nonlinear behaviour of damping controlled fluidelastic instability in a normal triangular tube array. *Journal of Fluids and Structures*, 18:573–593, 2003.

[11] M Paidoussis. Fluidelastic vibration of cylinder arrays in axial and cross flow: state of the art. *Journal of Sound and Vibration*, 76(3):329–360, 1981.

[12] D S Weaver and J A Fitzpatrick. A review of cross-flow induced vibrations in heat exchanger tube arrays. *Journal of Fluids and Structures*, 2:73–93, 1988.

[13] S J Price, M P Paidoussis, R MacDonald, and B Mark. The flow-induced vibration of a single flexible cylinder in a rotated square array of rigid cylinders with pitch-to-diameter ration of 2.12. *Journal of Fluids and Structures*, 1:359–378, 1987.

[14] M J Pettigrew and D J Gorman. Vibration of heat exchange components in liquid and two-phase cross-flow. *International Conference Vibration in Nuclear Plant, Kewswick, U.K.*, 2(2.3), 1978.

[15] S Savkar. Buffeting of cylindrical arrays in cross flow. *Vibration of arrays of cylinders in cross flow, ASME Symposium on Flow Induced Vibrations*, 2:195–210, 1984.

[16] A Zukauskas. Crossflow over tube bundles. *High-Performance Single-Phase Heat Exchangers, Hemisphere Publishing Corporation*, Chapter 12:241–264, 1989.

[17] M M Zdravkovich and J E Namork. Structure of interstitial flow between closely spaced tubes in staggered array. *FIV Conf*, pages 41–46, 1979.

[18] M M Zdravkovich and J E Namork. Flow structure within both stationary and vibrating tube banks with triangular pitch. *Proceedings of Vibration In Nuclear Plant, Keswick, U.K.*, paper 2:5:1–9, 1978.

[19] L K Grover and D S Weaver. Cross-flow induced vibrations in a tube bank - vortex shedding. *Journal of Sound and Vibration*, 59(2):263–276, 1978.

[20] D S Weaver and L K Grover. Cross-flow induced vibrations in a tube bank - turbulent buffeting and fluid elastic instability. *Journal of Sound and Vibration*, 59(2):277–294, 1978.

[21] D S Weaver and M El-Kashlan. On the number of tube rows required to study cross-flow induced vibrations in tube banks. *Journal of Sound and Vibration*, 75(2):265–273, 1981.

[22] J A Fitzpatrick and I S Donaldson. Row depth effects on turbulence spectra and acoustic vibrations in tube banks. *Journal of Sound and Vibration*, 73(2):225–237, 1980.

[23] S S Chen and J A Jendrzejczyk. Fluid excitation forces acting on a square tube array. *ASME Journal of Fluids Engineering*, 109:415–423, 1987.

[24] J Fitzpatrick, I Donaldson, and W McKnight. The structure of the turbulence spectrum of flows in deep tube array models. *ASME Symposium on Flow-induced vibration*, 104:21–30, 1986.

[25] J P Batham. Pressure distribution on in-line tube arrays in cross flow. *International Symposium, Vibration Problems in Industry, Keswick, U.K.*, Paper No. 411:1–24, 1973.

[26] S J Price and M P Padoussis. The flow-induced response of a single flexible cylinder in an in-line array of rigid cylinders. *Journal of Fluids and Structures*, 3:61–82, 1989.

[27] P J Southworth and M M Zdravkovich. Effect of grid-turbulence on the fluid-elastic vibrations of in-line tube banks in crosss flow. *Journal of Sound and Vibration*, 39(4):461–469, 1975.

[28] R E Franklin and B M H Soper. An investigation of fluid elastic instabilities in tube banks subject to fluid cross-flow. *In Proceedings 4th International Conference on Structural Mechanics in Reactor Technology*, Paper F6/7:1–14, 1977.

[29] S S Chen and J A Jendrzejczyk. Experiments on fluidelastic instability in tube banks subjected to liquid cross flow. *Journal of Sound and Vibration*, 78:355–381, 1981.

[30] M Rottmann and K Popp. Influence of upstream turbulence on the fluidelastic instability of a parallel triangular tube bundle. *Journal of Fluids and Structures*, 18(5):595–612, 2003.

[31] O Romberg and K Popp. Influence of upstream turbulence on the stability of tube bundles subject to cross-flow. *ASME PVP, Flow Induced Vibrations*, 328:11–18, 1996.

[32] G Rzentkowski and J H Lever. An effect of turbulence on fluidelastic instability in tube bundles: a nonlinear analysis. *Journal of Fluids and Structures*, 12:561–590, 1998.

[33] P R Owen. Buffeting excitation of boiler tube vibration. *Journal of Mechanical Engineering Science*, 7(4):431–439, 1965.

[34] D S Weaver and A Abd-Rabbo. A flow visualization study of a square array of tubes in water cross-flow. *ASME Journal of Fluids Engineering*, 107:354–363, 1985.

[35] A Abd-Rabbo and D S Weaver. A flow visualisation study of flow development in a staggered tube array. *Journal of Sound and Vibration*, 106(2):241–256, 1986.

[36] S J Price, M Paidoussis, W N Mureithi, and B Mark. Flow visualization in a 1.5 pitch-to-diameter rotated square array of cylinders subject to cross-flow. *Flow Induced Vibrations, Proceedings of the Instituation of Mechanical Engineers*, 6, 1991.

[37] S J Price, M P Paidoussis, and B Mark. Flow visualization in a 1.375 pitch-to-diameter parallel triangular array subject to cross-flow. *Proceedings International Sysmposium on Flow Induced Vibration and Noise*, 1:29–38, 1992.

[38] D S Weaver, H Y Lian, and X Y Huang. Vortex shedding in rotated square arrays. *Journal of Fluids and Structures*, 7(2), 1993.

[39] A Oengoren and S Ziada. Vortex shedding, acoustic resonance and turbulent buffeting in normal triangular tube arrays. *P Bearman (Ed.), Flow-Induced Vibration*, Balkema:295–313, 1995.

[40] J S Fitz-Hugh. Flow-induced vibrations in heat exchangers. *International Symposium on Vibration Problems in Industry, Kewsick, U.K.*, Paper No. 427, 1973.

[41] Y N Chen. The sensitive tube spacing region of the tube bank exchangers for fluid-elastic coupling in cross-flow. *ASME PVP, Symposium on Fluid-Structure Interaction*, PVP-PB-026:1–18, 1977.

[42] D S Weaver, J A Fitzpatrick, and M El-Kashlan. Strouhal numbers for heat exchanger tube arrays in cross flow. *ASME Journal of Pressure Vessel Technology*, 109:219–223, 1987.

[43] A Oengoren and S Ziada. Vorticity shedding and acoustic resonance in an in-line tube bundle. part ii:acoustic resonance. *Journal of Fluids and Structures*, 6:293–309, 1992.

[44] S Ziada and A Oengoren. Vorticity shedding and acoustic resonance in an in-line tube bundle. part i:vorticity shedding. *Journal of Fluids and Structures*, 6:271–292, 1992.

[45] S Ziada. Vorticity shedding and acoustic resonance in tube bundles. *Journal of the Brazilian Society of Mechanical Sciences and Engineering*, 2:186–199, 2006.

[46] D Polak and D S Weaver. Vortex shedding in normal triangular tube arrays. *Journal of Fluids and Structures*, 9:1–17, 1995.

[47] A A Zukauskas and V J Katinas. Flow-induced vibration in heat exchanger tube banks. *In Practical Experiences with Flow-Induced Vibrations, Berlin*, pages 188–196, 1980.

[48] A Oengoren and S Ziada. An in-depth study of vortex shedding, acoustic resonance and turbulent buffeting in normal triangular tube arrays. *Journal of Fluids and Structures*, 12:717–758, 1998.

[49] R Parker. Acoustic resonances in passages containing banks of heat exchanger tubes. *Journal of Sound and Vibration*, 57(2):245–260, 1978.

[50] S S Chen. Flow induced vibration and noise tube-bank heat exchangers due to von karman streets. *Journal of Engineering for Industry*, 90:134–146, 1968.

[51] J A Fitzpatrick. Acoustic resonance in in-line tube banks. *Journal of Sound and Vibration*, 85(3):435–437, 1982.

[52] J A Fitzpatrick. The predicition of flow-induced noise in heat exchangers tube arrays. *Journal of Sound and Vibration*, 99(3):425–435, 1985.

[53] B J Grotz and F R Arnold. Flow induced vibrations in heat exchangers. *Department of Mechanical Engineering Technical Report No. 31, Stanford University, California*, 1956.

[54] J A Fitzpatrick and I S Donaldson. Effects of scale on parameters associated with flow induced noise in tube arrays. *Proceedings of Symposium on Flow Induced Vibrations, Vol 2: Vibrations of Arrays of Cylinders in Cross Flow*, pages 243–250, 1984.

[55] J A Fitzpatrick and I S Donaldson. A preliminary study of flow and acoustic phenomena in tube banks. *Journal of Fluids Engineering*, 99:681–686, 1977.

[56] R D Blevins and M M Bressler. Acoustic resonance in heat exchanger tube bundles-part ii: Prediction and suppression of resonance. *ASME Journal of Pressure Vessel Technology*, 109:282–288, 1987.

[57] F L Eisinger and R E Sullivan. Suppression of acoustic waves in steam generators and heat exchanger tube banks. *ASME Journal of Pressure Vessel Technology*, 125:221–227, 2003.

[58] P A Feenstra, D S Weaver, and F L Eisinger. The effects of duct width and baffles on acoustic resonance in a staggered tube array. *Proceedings of the 8th International Conference on Flow-Induced Vibration*, 1:459–464, 2004.

[59] J A Peterka and P D Richardson. Effects of sound on separated flows. *Journal of Fluid Mechanics*, 37:265–287, 1969.

[60] R D Blevins. The effect of sound on vortex shedding from cylinders. *Journal of Fluids Mechanics*, 161:217–237, 1985.

[61] M Mathias, A N Stokes, K Hourigan, and M C Welsh. Low-level flow induced acoustic resonances in ducts. *Symposium on fundamental aspects of vortex motion, Tokyo*, 1987.

[62] J W Hall, S Ziada, and D S Weaver. Vortex-shedding from single and tandem cylinders in the presence of applied sound. *Journal of Fluids and Structures*, 18:741–758, 2003.

[63] X Y Huang. Suppression of vortex shedding from a circular cylinder by internal acoustic excitation. *Journal of Fluids and Structures*, 9:563–570, 1995.

[64] N Fujisawa and G Takeda. Flow control around a circular cylinder by internal acoustic excitation. *Journal of Fluids and Structures*, 17:903–913, 2003.

[65] S C Kacker and Hill R S. Flow over a circular cylinder in the presence of standing sound waves. *The Department of Mechanical Engineering, The University of Newcastle Upon Tyne.*

[66] P A Feenstra, D S Weaver, and F L Eisinger. Acoustic resonance in a staggered tube array: Tube response and the effect of baffles. *Journal of Fluids and Structures*, 21:89–101, 2005.

[67] J A Fitzpatrick, I S Donaldson, and W McKnight. Some observations of the pressure distribution in a tube bank for conditions of self generated acoustic resonance. *International Symposium, Vibration Problems in Industry, Keswick, U.K.*, Paper 3:6:1–13, 1978.

[68] M C Welsh, K Hourigan, R J Alfredson, and Pan Di Lin. Active control of flow-excited acoustic resonance: higher order acoustic modes. *IMechE 1991*, C416/068:531–538, 1991.

[69] S C Kacker, B Pennington, and R S Hill. Measurements of the fluctuating lift coefficient and of the correlation length for vortex shedding from cylindrical tubes. *Proceedings of Vibration In Nuclear Plant, Kewsick, U.K.*, Paper No. 416:1–15, 1973.

[70] B W Roberts. Low frequency aeroelastic vibrations in a cascade of circular cylinders. *Mechanical engineering science monographs. Institute of Mechanical Engineers.*

[71] S J Price. A review of theoretical models for fluidelastic instability of cylinder arrays in cross-flow. *Journal of Fluids and Structures*, 9:463–518, 1995.

[72] H J Connors. Fluid-elastic vibration of tube arrays excited by cross flow. *Proceedings, Flow-induced vibrations in heat exchangers, ASME, Chicago*, pages 42–56, 1970.

[73] S J Price. An investigation on the use of connors' equation to predict fluidelastic instability in cylinder arrays. *ASME Journal of Pressure Vessel Technology*, 123:448–453, 2001.

[74] S S Chen. Instability mechanisms and stability criteria of a group of circular cylinders subjected to cross-flow. part i: Theory. *ASME Journal of Vibrations, Acoustics, Stress, Reliability and Design*, 105:51–58, 1983.

[75] S S Chen. Instability mechanisms and stability criteria of a group of circular cylinders subjected to cross-flow. part ii: Numerical results and discussion.

ASME Journal of Vibrations, Acoustics, Stress, Reliability and Design, 105:253–260, 1983.

[76] H Tanaka and S Takahara. Fluid elastic vibration of tube array in cross flow. *Journal of Sound and Vibration*, 77(1):19–37, 1981.

[77] S J Price and S Kuran. Fluidelastic stability of a rotated square array with multiple flexible cylinders, subject to cross-flow. *Journal of Fluids and Structures*, 5:551–572, 1991.

[78] J H Lever and D S Weaver. A theoretical model for fluidelastic instability in heat exchanger tube bundles. *ASME Journal of Pressure Vessel Technology*, 104:147–158, 1982.

[79] D S Weaver and M El-Kashlan. The effect of damping and mass ratio on the stability of tube bank. *Journal of Sound and Vibration*, 76(2):283–294, 1981.

[80] S Granger, R Campistron, and J Lebert. Motion-dependent excitation mechanisms in a square in-line tube bundle subject to water cross-flow: an experimental and modal analysis. *Journal of Fluids and Structures*, 7:521–550, 1993.

[81] M P Paidoussis and S J Price. The mechanisms underlying flow-induced instabilities of cylinder arrays in crossflow. *Journal of Fluid Mechanics*, 187:45–59, 1988.

[82] S Granger and M Paidoussis. An improvement to the quasi-steady model with application to cross-flow-induced vibration of tube arrays. *Journal of Fluid Mechanics*, 320:163–184, 1996.

[83] S S Chen and G S Srikantiah. Motion-dependent fluid force coefficients for tubes arrays in crossflow. *ASME Journal of Pressure Vessel Technology*, 123:429–436, 2001.

[84] M Andjelic and K Popp. Stability effects in a normal triangular cylinder array. *Journal of Fluids and Structures*, 3(2):165–185, 1989.

[85] J Lever and D Weaver. On the stability of heat exchanger tube bundles. part i: modified theoretical model. part ii: numerical results and comparison with experiment. *Journal of Sound and Vibration*, 107:375–410, 1986.

[86] A Andjelic, R Austermann, and K Popp. Multiple stability boundaries of tubes in a normal triangular cylinder array. *ASME Journal of Pressure Vessel Technology*, 114:336–343, 1990.

[87] M Yetisir and D S Weaver. On an unsteady theory for fluidelastic instability of heat exchanger tube arrays. *Proceedings International Symposium on Flow Induced Vibration and Noise*, 3:181–195, 1988.

[88] S J Price and M P Paidoussis. Fluidelastic instability of an infinite double row of circular cylinders subject to a cross-flow. *ASME Journal of Vibrations, Acoustics, Stress, Reliability and Design*, 105:59–66, 1983.

[89] A Simpson and J W Fowler. An improved mathematical model for the aerodynamic forces on tandem cylinders in motion with aeroelastic applications. *Journal of Sound and Vibration*, 51(2):183–217, 1977.

[90] S S Chen and J A Jendrzejczyk. Characteristics of fluidelastic instability of tube rows in crossflow. *International Conference on Flow Induced Vibrations, Bowness-on-Windermere, England*, (B3):77–84, 1987.

[91] J L Parrondo, C Santolaria, and D S Weaver. The effect of partial admission on the fluidelastic instability of a parallel triangular tube array subject to water cross-flow. *Flow induced vibrations*, Balkema 1995:315–326, 1995.

[92] M P Paidoussis, S J Price, and N W Mureithi. On the practical nonexistence of multiple instability regions for heat-exchange arrays in cross-flow. *Flow induced vibrations, (Balkema 1995)*, pages 283–294, 1995.

[93] C Meskell. On the underlying mechanisms responsible for damping controlled fluidelastic instability in tube arrays. *2005 ASME Pressure Vessels and Piping Division Conference*, 2005.

[94] S Granger. A new signal processing method for investigating fluidelastic phenomena. *Journal of Fluids and Structures*, 4:73–97, 1990.

[95] C E Teh and H G D Goyder. Data for the fluidelastic instability of heat exchanger tube bundles. *Flow Induced Vibration and Noise in Cylinder Arrays*, 3:77–94, 1988.

[96] S S Chen, S Zhu, and J A Jendrzejczyk. Fluid damping and fluid stiffness of a tube row in crossflow. *Journal of Pressure Vessel Technology*, 116:370–383, 1994.

[97] H Tanaka, S Takahara, and K Ohta. Flow-induced vibration of tube arrays with various pitch to diameter ratios. *ASME Journal of Pressure Vessel Technology*, 104:168–174, 1982.

[98] E Achenbach. Investigations on the flow through a staggered tube bundle at reynolds numbers up to $re = 10^7$. *Warmë und Stoffübertragung*, Bd 2:47–52, 1969.

[99] M M Zdravkovich and J E Namork. Excitation, amplification and suppression of flow-induced vibration in heat exchangers. *Proceedings Practical Experiences with Flow Induced Vibrations*, Paper A5:107–117, 1980.

[100] S J Price and M P Paidoussis. The aerodynamic forces acting on groups of two and three circular cylinders when subject to a cross flow. *Journal of Wind Engineering and Industrial Aerodynamics*, 17:329–347, 1984.

[101] O Romberg and K Popp. Fluid damping controlled instability in tube bundles subjected to air cross-flow. *Flow, Turbulence and Combustion*, 61:285–300, 1999.

[102] A A Zukauskas, R Ulinskas, and V J Katinas. Fluid dynamics and flow induced vibrations in tube banks. *Hemisphere Publishing Corporation*, 1988.

[103] D S Weaver and H C Yeung. The effect of tube mass on the flow induced response of various tube arrays in water. *Journal of Sound and Vibration*, 93(3):409–425, 1984.

[104] C Meskell. Identification of a non-linear model for fluidelastic instability in a normal triangular tube array. *PhD Thesis*, 1999.

[105] H C Yeung and D S Weaver. The effect of approach flow direction on the flow-induced vibrations of a triangular tube array. *ASME Journal of Vibration, Acoustics, Stress and Reliability in Design*, 105:76–82, 1983.

[106] S S Chen. Guidelines for the instability flow velocity of tube arrays in crossflow. *Journal of Sound and Vibration*, 93(3):439–455, 1984.

[107] R D Blevins and M M Bressler. Acoustic resonance in heat exchanger tubbe bundles-part 1: Physical nature of the phenomenon. *ASME Journal of Pressure Vessel Technology*, 109:275–281, 1987.

[108] M M Zdravkovich and K L Stonebanks. Intrinsically nonuniform and metastable flow in and behind tube arrays. *Journal of Fluids and Structures*, 4:305–319, 1990.

[109] M M Zdravkovich. On suppressing metalstable interstitial flow behind a tube array. *Proceedings Fifth Internation Conference on Flow Induced Vibrations, IMechE 1991-6, Brighton, UK*, (C416/071):185–190, 1991.

[110] J Keays and C Meskell. A study of the behaviour of a single-bladed waste-water pump. *Journal of Process Mechanical Engineering*, 220(2):79–87, 2006.

Appendix A

Terms related to Vortex Shedding

Symmetric vortex shedding - vortices are shed out of phase from the upstream wakes resulting in vortices shed from both sides simultaneously of the cylinder downstream of the wakes.

Anti-symmetric vortex shedding - vortices are shed alternatively and are in phase with neighbouring cylinders. This results in alternate vortices shed in the next row of cylinders.

Alternate vortex shedding - vortices are shed from alternate sides of the cylinder.

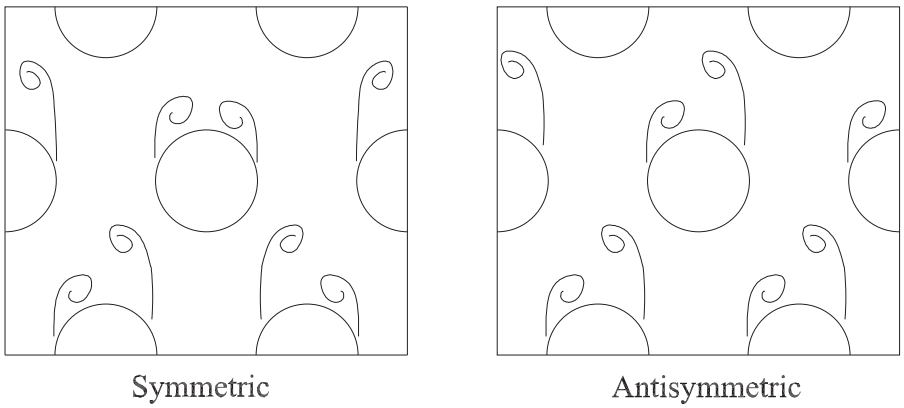

Figure A.1: Vortex Shedding

When tubes are arranged in an in-line configuration flow lanes develop. As the flow proceeds past successive tube rows a jet-like profile develops. Jet instability is initiated at locations of flow separation from tubes in the first row. It initial starts off as thin shear layers of the jet. Vortices in jet shear layers roll up and grow in size and strength as the flow proceeds past successive tube rows. This produces vortices both sides of

the flow lane inside the tube wake. Figure A.2 shows an image from Ziada & Oengoren [5] showing jet instability.

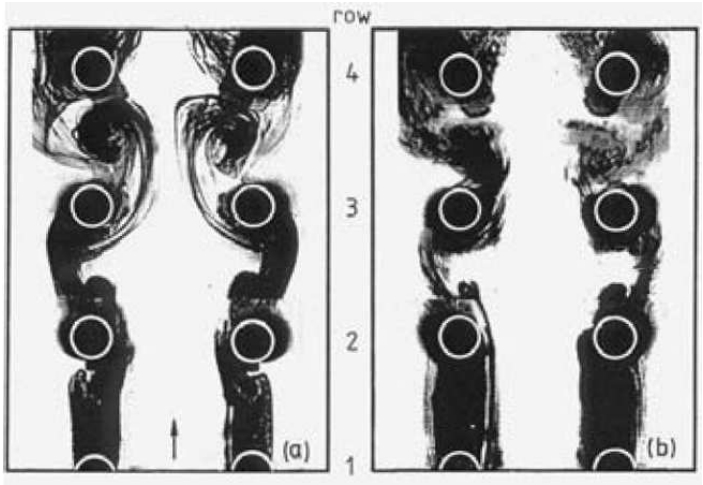

Figure A.2: Jet Instability [5]

Shear layer instability - When the tube spacing is more restricted again the flow separates from the cylinder and two shear layers develop. Small vortices develop in the shear layer as shown in Fig. A.3 (Ziada *et al.* [6]). For shear layer instability to occur the shear layers at both sides of the flow lane oscillate. This results in an unstable reattachment at the downstream cylinder causing increased oscillations and shear layer instability.

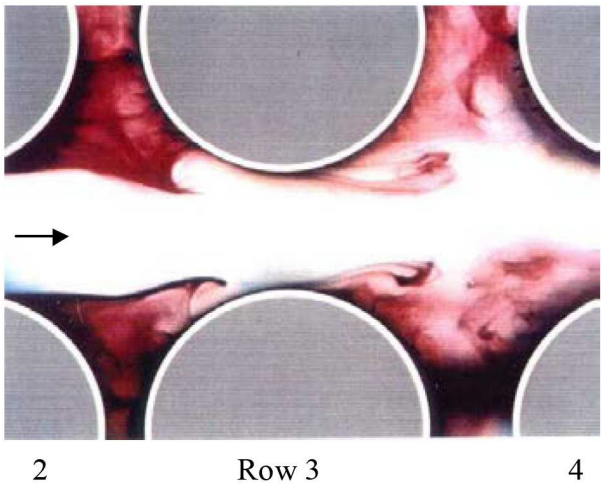

Figure A.3: Shear layer Instability [6]

Wake instability - flow separates from the cylinder and two shear layers develop and role up shedding vortices which become distorted and stretched out as the two shear layers interact and eventually become dissipated in the turbulent flow generated within the array. See Fig. A.4 (Ziada & Oengoren [7]) for a visual representation.

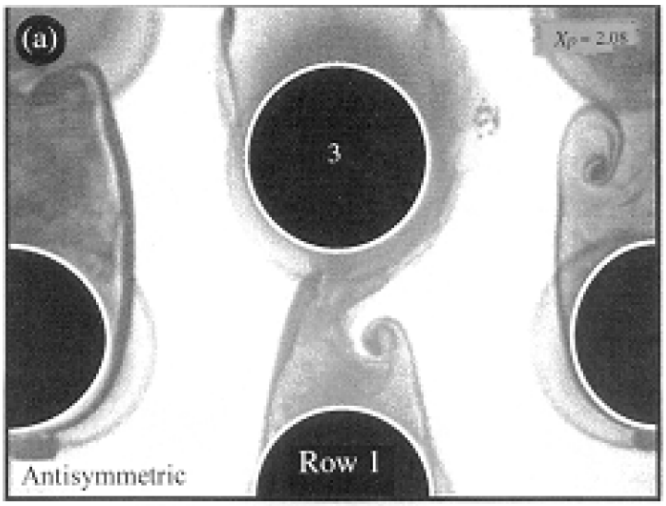

Figure A.4: Wake instability [7]

Appendix B

Pressure Tapped Tube Drawings

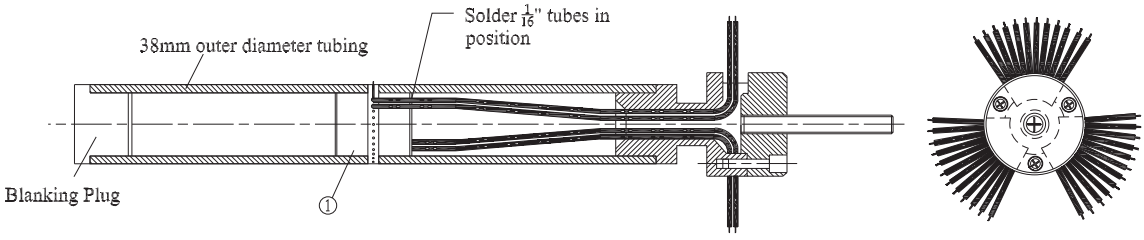

Figure B.1: Schematic of the Pressure Tapped Tube

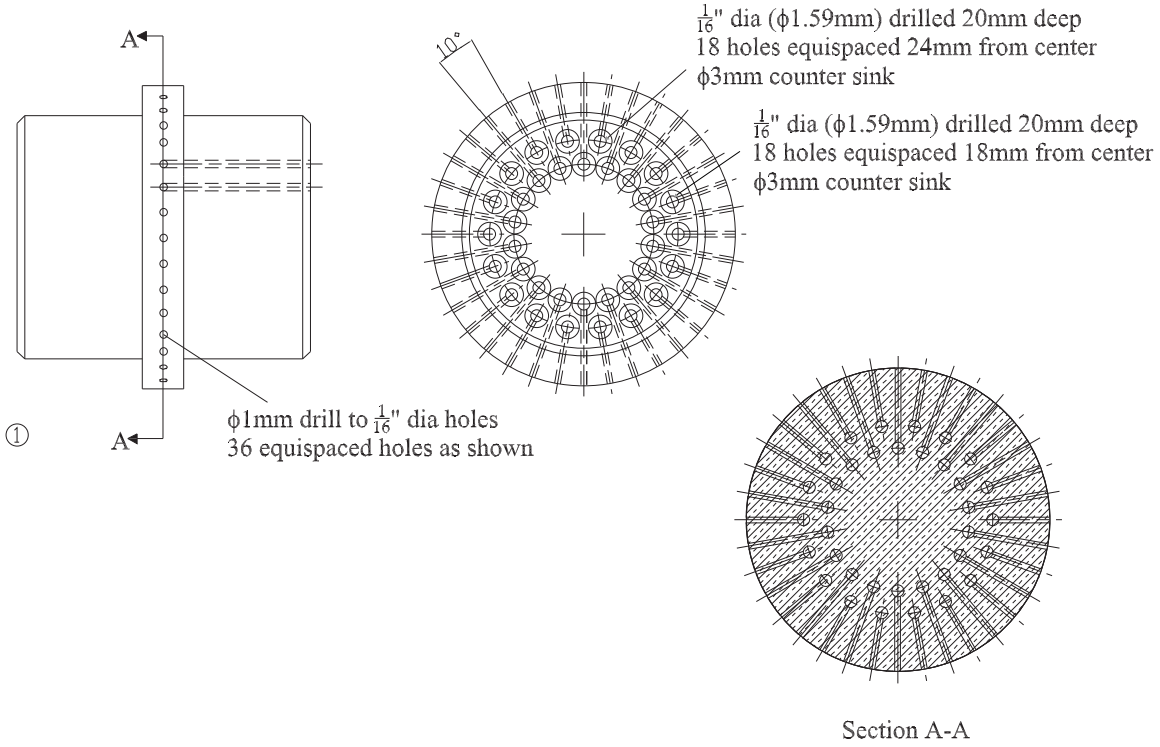

Figure B.2: Schematic of the Machined Block(1) - The location of the Pressure Taps on the Tube

Appendix C

FEA Analysis of Test Section

FEA analysis was performed with ANSYS on the test section for two tube arrays installed with pitch ratios of 1.32 and 1.58. This was done to measure the frequencies of the transverse acoustic modes of the test section. The frequencies obtained were found to be in reasonable agreement with the quantities measured experimentally. As agreement between the FEA model and experiments was good, the FEA model was used to determine sources (nodes) and sinks (anti-nodes) within the test section. From Fig. C.1 it was observed that the sources were located at the center of the array and at the side walls with a peak in energy at the third row. Determining the location of the nodes and anti-nodes was important, because placing the speaker at an anti-node would have made artificial excitation of acoustic resonance using speakers very difficult. Hence, the speakers where located at a node. It was observed that a node was located at the test section wall with the energy peaking at third row (middle). However, the setup used had half cylinders mounted against the test section walls at first, third and fifth (last) rows. So if the speakers had of been centered at those positions direct propagation into the test section would have been restricted. Hence, the speakers were located at the location closest to the highest available energy levels where direct propagation into the test section could be achieved explicitly in line with the second row. Once the speakers were installed the first and second acoustic modes could be excited by wiring the speakers in different configurations as described previously.

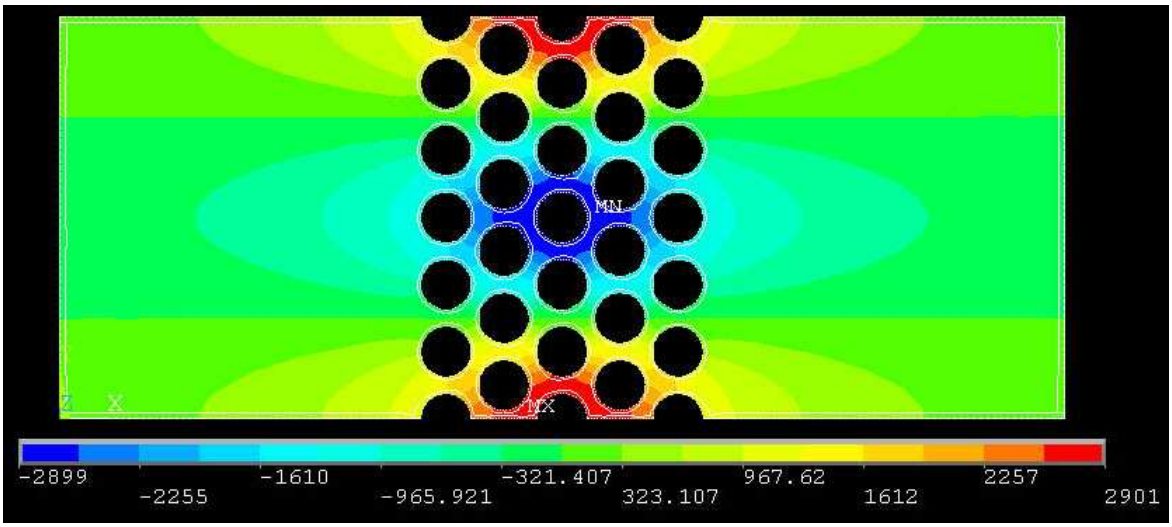

Figure C.1: FEA model showing the pressure distribution for the second acoustic mode of the test section with P/d=1.32

Appendix D

Error Analysis

In the chapter 3 the instruments used in this study were discussed. This section examines the error of uncertainty in the measurement techniques. The uncertainty associated with each technique is reported with a 95% confidence interval. The uncertainty interval ($\pm E$) is the band about the reported result within which the true value is expected to lie with 95% confidence. The uncertain is the combination of the systematic error (S) and the random error (R) as detailed in Eqn. D.1.

$$E = \sqrt{S^2 + R^2} \tag{D.1}$$

Systematic errors are errors which tend to shift all measurements in a systematic way so their mean value is displaced. Random errors are errors which fluctuate from one measurement to the next. They yield results distributed about some mean value. The random error is defined as twice the standard deviation.

The free stream velocity flow measurements were conducted using a Furness Control micromanomenter (model FC015). According to manufacturer's specification the instrument has an uncertainty of 1%. This flow meter has an output display with a precision of three decimal places. The velocity measurements used in this study were based on a ten second sample. However, due to the fluctuating velocity in the flow using a precision of three decimals would have been erroneous. The measurement was accurate to $\pm$ 0.03m/s. Given a 95% confidence interval the velocity was given a precision of 0.1m/s.

The gap velocity was calculated from free stream flow velocity. It was obtained by multiplying the free stream free velocity by a constant where the constant was

obtained from the geometry of the array. As the geometry measurement was accurate to 0.01mm, no significant additional uncertainty was introduced into the gap velocity measurement.

Reynolds number was obtained using free stream flow velocity, tube diameter, fluid density and fluid viscosity. The first two terms were measured. The latter terms where available from standard tables. The largest uncertain in the Reynolds number is the temperature, as the fluid density and viscosity are temperature dependent. The error associated with the Reynolds was not possible to determine as the temperature was not rigorously monitored. In this instance the error is systematic and would be applied at all calculated values of Reynolds number.

The local flow velocity was measured using hot-wire anemometry. Hot-wire anemometry was used in two experimental setups. In the first setup, local flow velocity measurements were made with all tubes stationary. In the second setup, local flow velocity measurements around an oscillating cylinder (time delay tests) were made. In the first setup, it was possible to measure the random error using standard deviation of the measurement signal. This resulted in an uncertainty of 20-40% depending on the magnitude of the free stream flow velocity and position around the cylinder. The reason for the large uncertainty is due to the high fluctuating velocities due to the high levels of turbulence in the tube array. In the latter setup, a phase lag between the oscillating local flow velocity and the tube motion was extracted. Effects of turbulence were observed in both signals. However, 99 oscillations were averaged reducing the noise level by a factor 10. Using an analysis technique described in section 6.2, a phase lag between tube motion and local flow velocity was extracted. This process was repeated five times. The uncertainty in the measurement was position dependent, however on average it was of the order of 10%. The value given in the uncertainty was only for the time delay measurements deemed to be of acceptable quality (time delays presented in Tables. 6.1).

The error associated with the measurements that utilised an accelerometer as a measurement device were dependent on the measurement type. The accelerometer was used to measure: structural and fluid damping, the stability threshold and tube motion in the time delay measurements (discussed in previous paragraph).

The uncertainty in structural and fluid damping measurements are given in terms of standard deviation. For structural damping, there was no flow and as a result the uncertainty in the measurement was approximately 2%. The fluid damping measurement on the contrary was subject to flow. As the instrumented tube was subject to high levels of turbulence, the uncertainty in the measurement increased five fold and is why the tests were repeated twenty times to obtain a statically meaningful value.

The uncertainty in the stability threshold measurements was dependent on the array pitch ratio. However as the measurement signal was oscillatory, using the standard deviation to determine the uncertainty was not applicable. The tube oscillation at a fixed velocity was measured and the tests repeated 10 times. For P/d=1.32 the uncertainty was generally less than 1.2% and similarly for the pitch ratio of 1.97. For P/d=1.58 the uncertainty in the measurement was much larger at 30% when the tube unstable due fluidelastic instability. The large uncertainty was due to jet switching also observed in this pitch ratio.

The frequency resolution measured was dependent on the sampling frequency, the duration of the test and the number of averages. When calculating the natural frequency of the structure, a low sampling frequency was used. If the measurement length was long the precision was high plus the number of averages was also high. The higher the number averages the lower the noise level. The noise level reduced by a factor of the square root of the number of averages. The precision of other measurements taken were not required to be as accurate as above. The microphone measurements required a higher sampling frequency to measure the higher frequency components. In this instance a frequency resolution of 1Hz sufficed.

As discussed previously the pressure transducers where calibrated by applying a fixed known pressure. The applied pressure was 5kPa and this was determined to within $\pm$0.01kPa. Applying this known pressure the uncertainty in the pressure transducer measurement was less than 1%. However, when the pressure on the surface of the measurement cylinder was measured, pressure fluctuations due to turbulence in the tube array increased the spread in the measurement signal. Furthermore, this was a function of position and pitch ratio. Like the stability threshold uncertainty, the pitch ratio of 1.58 showed the largest variation with an uncertainty of 32% caused by

the jet switching in this array. For the pitch ratios of 1.32 and 1.97 the uncertainty was smaller with the largest uncertain been 5.4% and 7%, respectively.

The pressure coefficient was obtained from pressure at the stagnation point, the pressure at a given position angle, square of the gap velocity and fluid density. The uncertainty in the pressure coefficient is therefore a combination of the uncertainties. However, as the fluid density is temperature dependent and the temperature was not rigorously monitored it was no possible to specify the uncertainty in the pressure coefficient.

The uncertainty in the lift and drag force was obtained by repeating tests at given parameters and measuring the static fluid forces. This was repeated for a number of flow velocities in the pitch ratio of 1.32. The largest uncertainty in the lift and drag force was at the lowest flow velocity (2m/s) with values of 34% and 6%, respectively. The uncertainty reduces significantly as the flow velocity increases. In fact the uncertainty reduces to 8% and 0.5% for the lift and drag forces, respectively.

The input power to the speakers was measured with a precision of 0.1W using a digital multi-meter. The acoustic sound pressure level as a result of the speakers was measured using G.R.A.S. microphones. The acoustic pressure sensitivity was obtained using a *Brüel* and Kj*ae*r Sound Level Calibrator Type 4231 at 1Pa (94dB). According to manufacturer's specification the sound level calibrator has an uncertainty of ±0.2dB. However, the peak value of sound pressure level will reduced somewhat due to leakage of energy when the spectral analysis was performed on the signal. As the exact determination of sound pressure level was not necessary, the amount of leakage was not measured. Hence, no measurement of uncertainty was determined.

Tube displacement was measured using a displacement gauge which was accurate to 0.01mm. As the displacement gauge was an analogue device, the degree of uncertainty was $\pm 0.01mm$.

Appendix E

Pitch Ratio of 1.97

E.1 Pressure Distribution

The pressure distribution around a cylinder in the third row was discussed in section 5.1.2. The effect of Reynolds number and tube displacement will now be briefly discussed. At the front of the cylinder at all Reynolds numbers the pressure coefficient was relatively constant. This trend changes quickly at all other positions around the cylinder. At higher Reynolds numbers C_P collapses well, fluctuating about a constant value indicating that the pressure scales with dynamic head. This change in behaviour would suggest a change in the behaviour of the flow. This was shown to be the case as will be demonstrated by the change in the drag force behaviour at a comparable Reynolds number ($\sim 6.8 \times\ 10^4$).

The effect of tube displacement was least distinct with the pitch ratio of 1.97. This was not surprising as the gap between neighbouring cylinders was larger. In fact, the largest change as a result of tube displacement occurred at the front of the cylinder and not at the minimum gap between neighbouring cylinders. This suggests that the effect of the neighbouring cylinders was very small especially as the largest changes resulted from the redistribution of the fluid impinging on the front of the cylinder. There was no significant changes in pressure at the rear of the cylinder. This was not surprising as there was only minimal changes on the front face of the cylinder. Hence, no significant reorganization of the flow occurred.

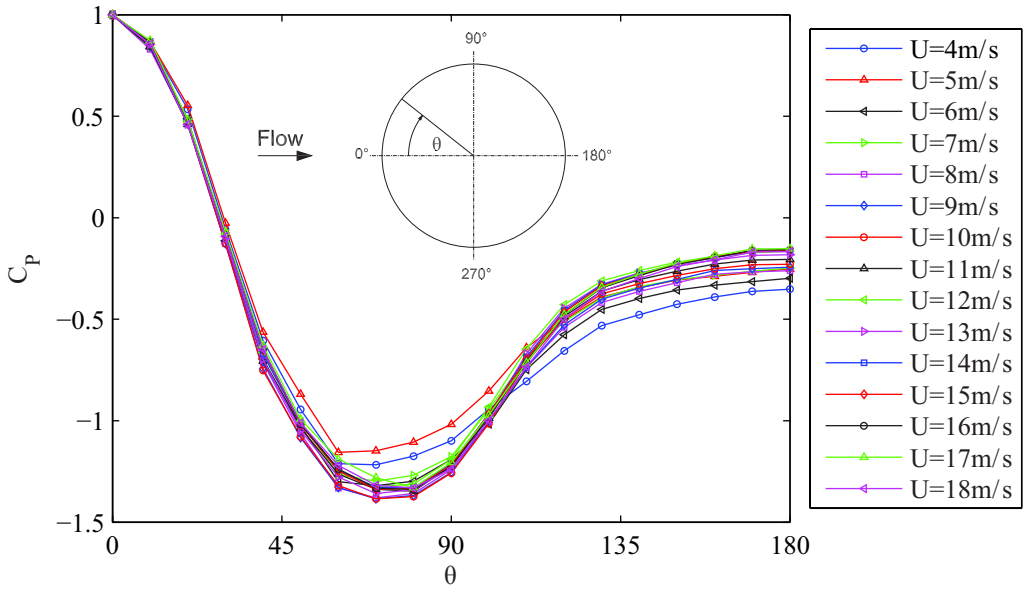

Figure E.1: P/d=1.97; $y/d = 0$, C_P at all velocities tested

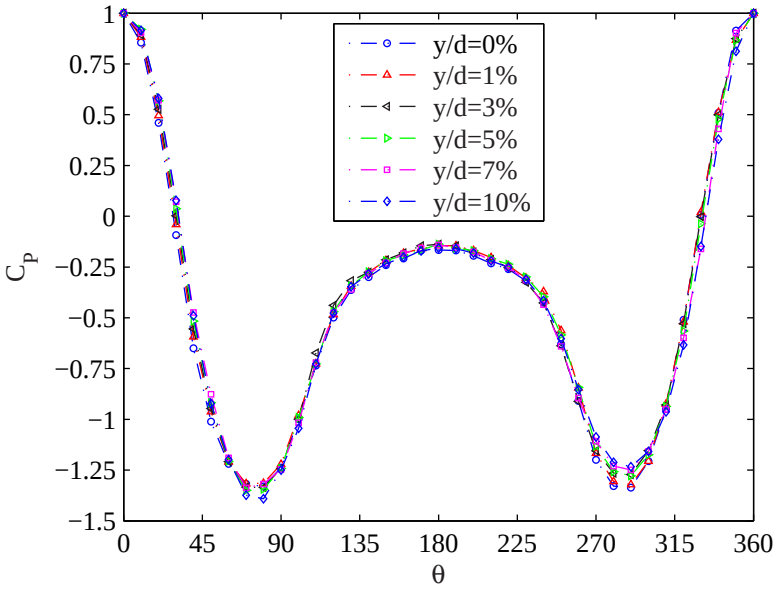

Figure E.2: $P/d = 1.97$; C_P at various tube displacements, $U = 18m/s$

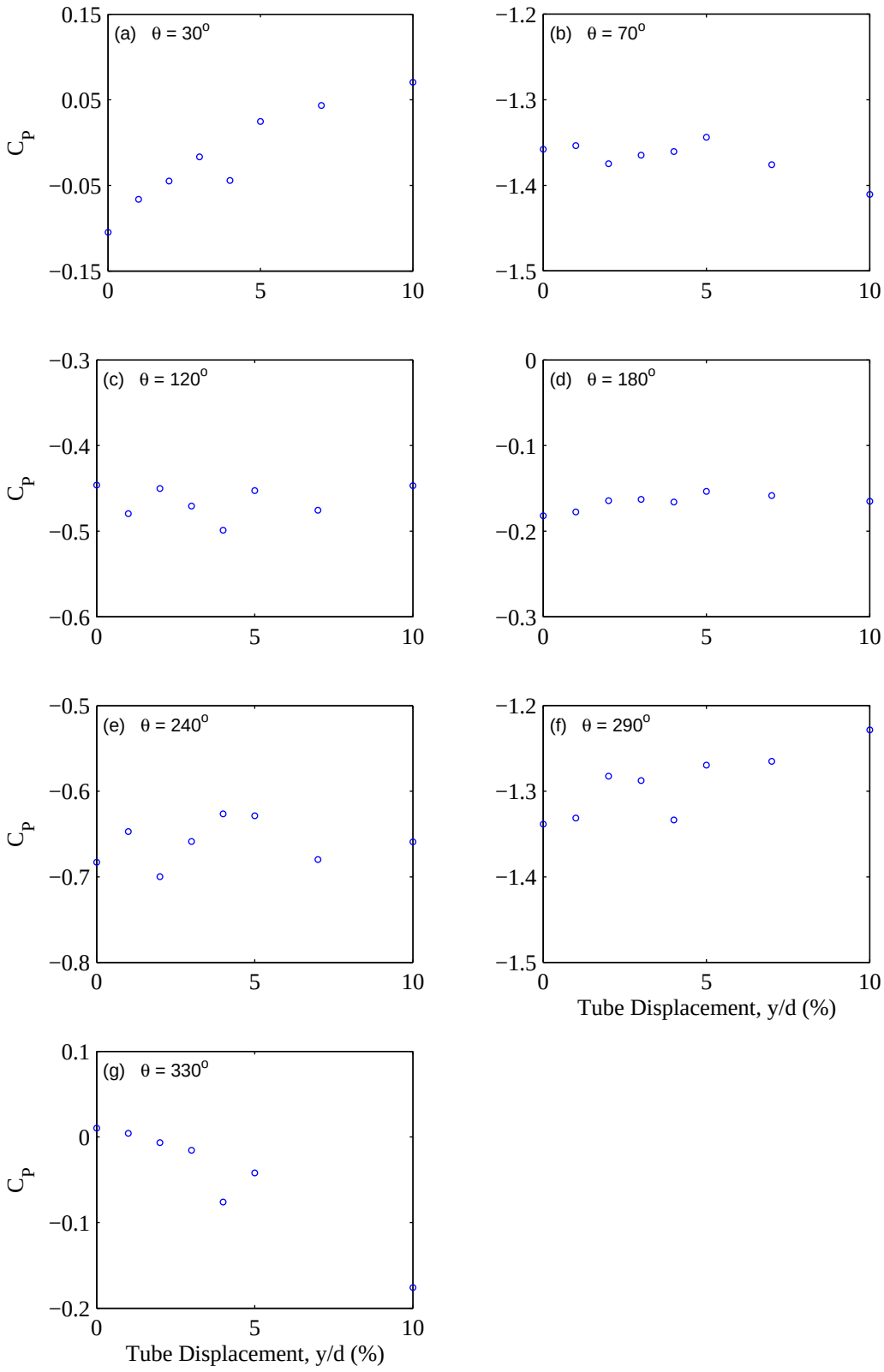

Figure E.3: $P/d = 1.97$; C_P at various positions around the cylinder for $y/d = 0-10\%$ and $U = 13m/s$

E.2 Drag Force

For $P/d = 1.32$ and more so in $P/d = 1.58$ the effect of tube displacement on the drag force was small. This trend continued as the array pitch increased (P/d=1.97) with the effect of tube displacement reduced further. Plotting the drag force data at all tube displacements resulted in the various traces collapsing well (see Fig. E.4), far better than that observed for the pitch ratio of 1.58. This was as a consequence of there been no flow instability in the tube array with pitch ratio of 1.97 unlike $P/d = 1.58$ were flow instability was dominant. Again, fitting a single line and a quadratic curve provided an inferior fit compared to two lines. The indices obtained were 1.4 and 2 for the lower and higher Reynolds numbers, respectively, with the transition in the flow regime occurring at a slightly higher Reynolds number ($\approx 6.8 \times 10^4$). For the sake of brevity the respective indices obtained separately at all tube displacements tested are shown in Fig. E.6. The indices again fluctuate about mean values illustrating the minimal effect of tube displacement on the drag force.

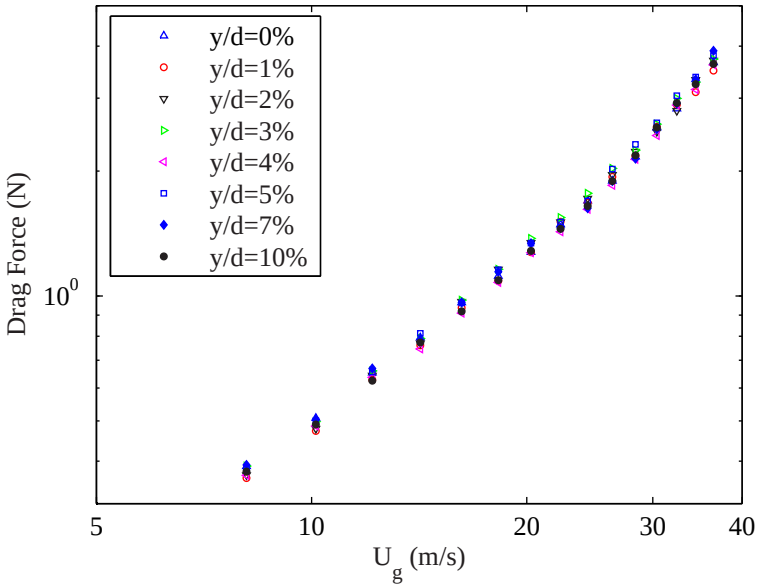

Figure E.4: $P/d = 1.97$; Drag force against gap velocity at all tube displacements

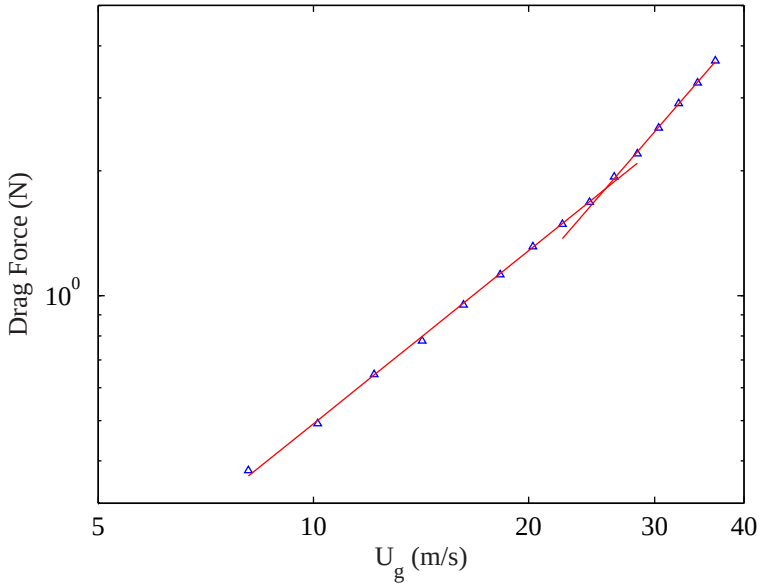

Figure E.5: $P/d = 1.97$; Drag Force for all tube displacements averaged

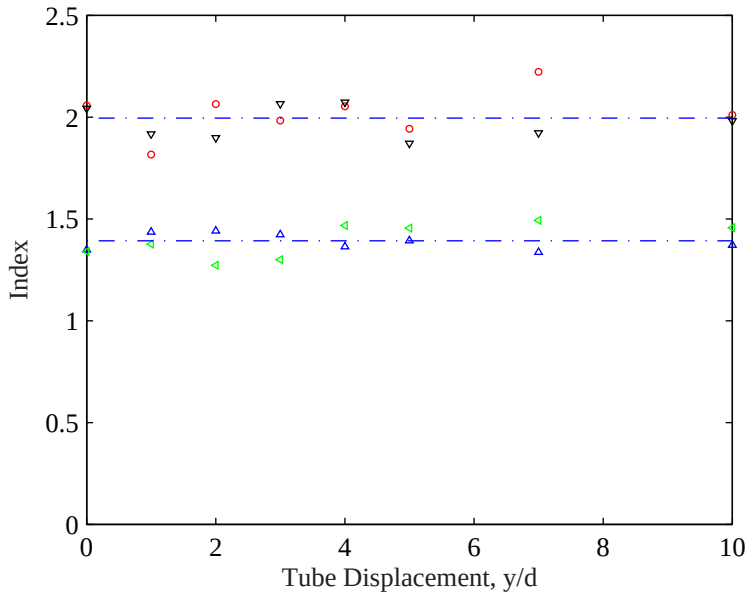

Figure E.6: $P/d = 1.97$; Index relating drag force and gap velocity

Using a similar analysis to that carried out for other pitch ratios of 1.32 and 1.58. The relationship between drag coefficient and Reynolds number is shown in Eqn. E.1. Like P/d=1.58 the index, n and constant k for the lower and higher Reynolds number range were different to account for the change in the flow regime.

$$C_D = kRe^n \tag{E.1}$$

$$Re < 6.8 \times 10^4 \begin{cases} k = 319 \\ n = -0.6 \end{cases}$$

$$Re > 6.8 \times 10^4 \begin{cases} k = 0.396 \\ n = 0 \end{cases}$$

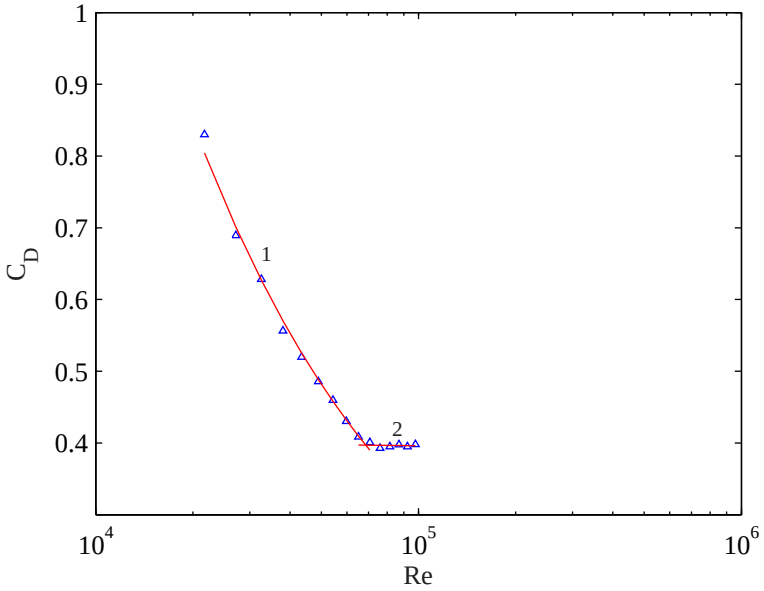

Figure E.7: P/d=1.97; Drag Coefficient (averaged for all tube displacements) against Gap Velocity

E.3 Lift Force

It was discussed in section 5.1.2 that the lift distribution for $P/d = 1.97$ was peculiar with the lift force fluctuating about zero at lower Reynolds numbers and a net force generated at higher Reynolds numbers. The peculiarity in the lift distribution was not attributed to a rotational offset and could only be explained by a flow induced phenomena. Figure E.8 shows the lift coefficient for a range of tube displacements. Further experiments are required to better understand the pitch ratio of 1.97.

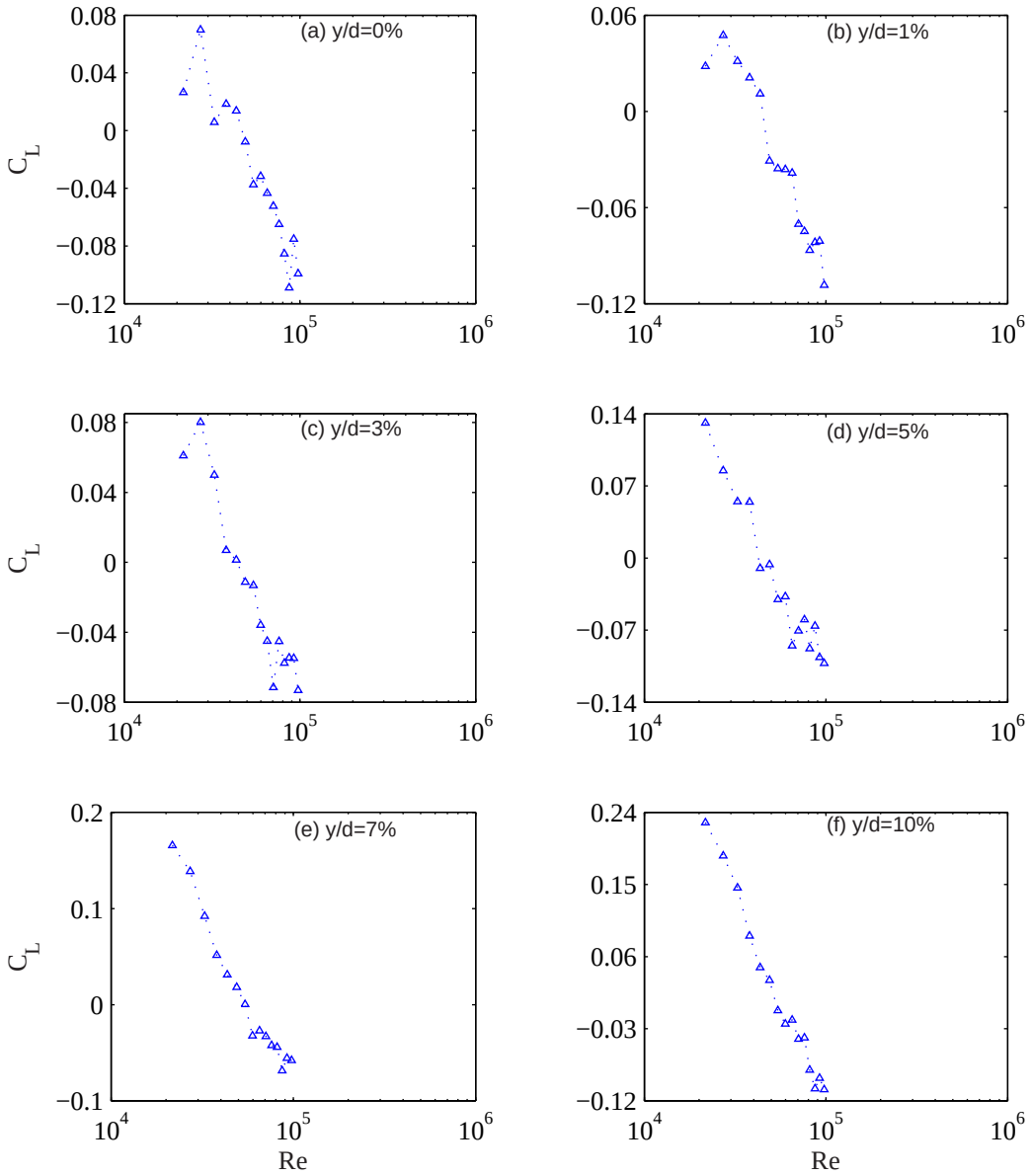

Figure E.8: P/d=1.97; Lift Coefficient against Reynolds number at various tube displacements

The lift coefficient against tube displacement for a range of flow velocities was also plot (see Fig. E.9). It can be seen that at the lower velocities the lift coefficient behaves as would be expected, that is, increasing with tube displacement. However, as the velocity was increased the peculiarity observed previously results in the lift coefficient generated in the opposite direction (negative) fluctuating about a constant.

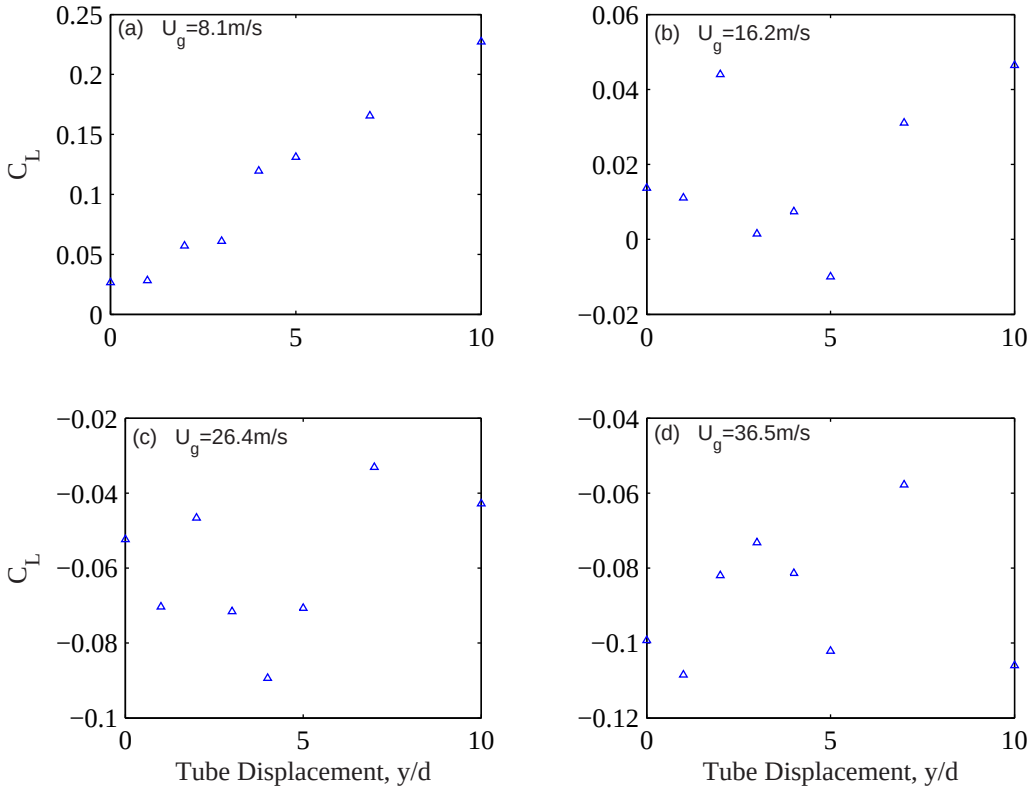

Figure E.9: P/d=1.97; Lift coefficient against tube displacement at various velocities

Appendix F

Further Analysis of P/d=1.32 and P/d=1.58

F.1 Pressure Coefficient; P/d=1.32

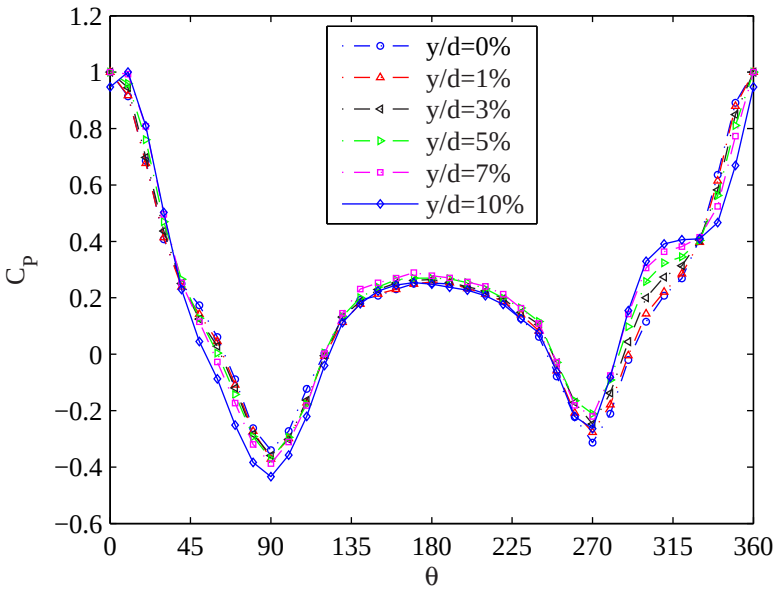

Figure F.1: $P/d = 1.32$; C_P at various tube displacements, $U = 4m/s$

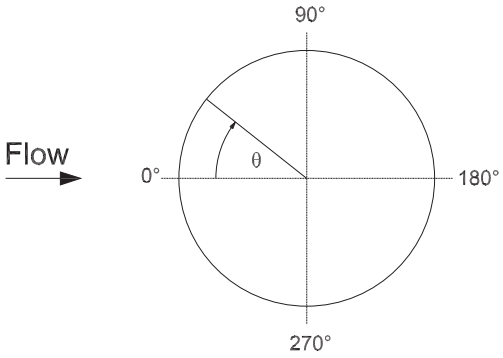

Figure F.2: Schematic of position angle

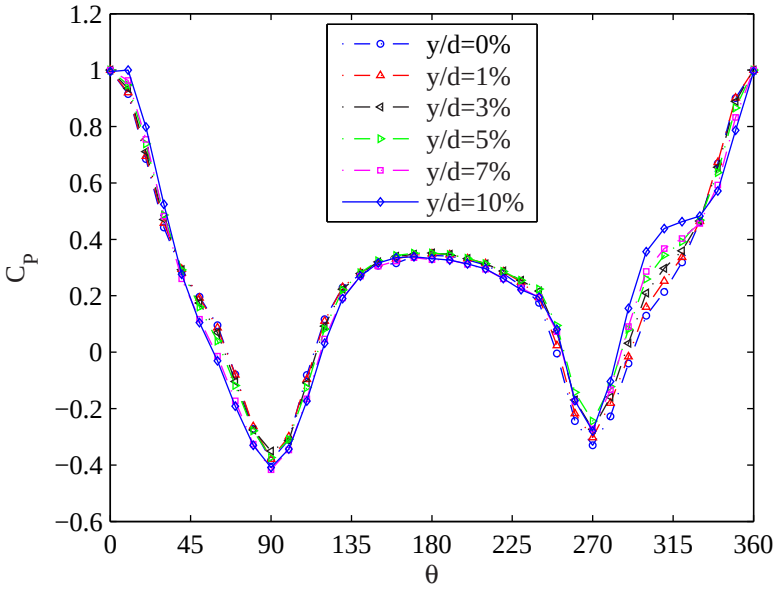

Figure F.3: $P/d = 1.32$; C_P at various tube displacements, $U = 10m/s$

F.2 Pressure Coefficient; P/d=1.58

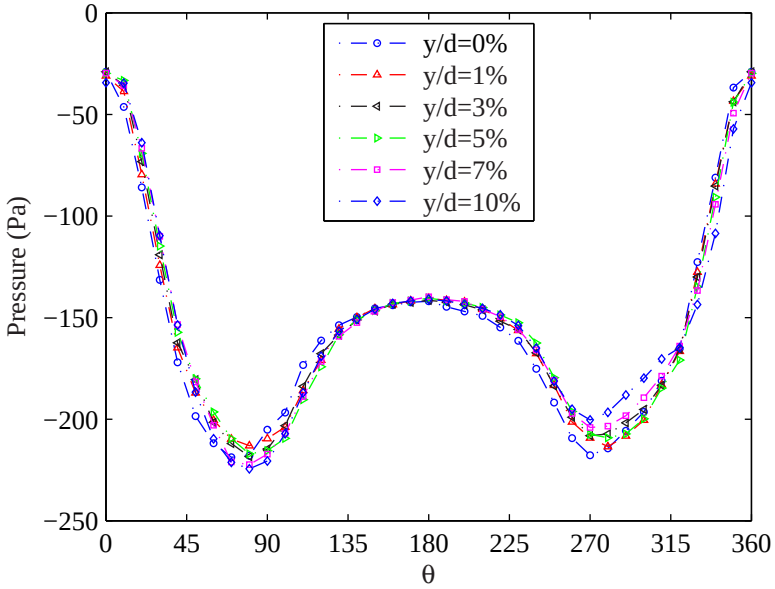

Figure F.4: $P/d = 1.58$; C_P at various tube displacements, $U = 5m/s$

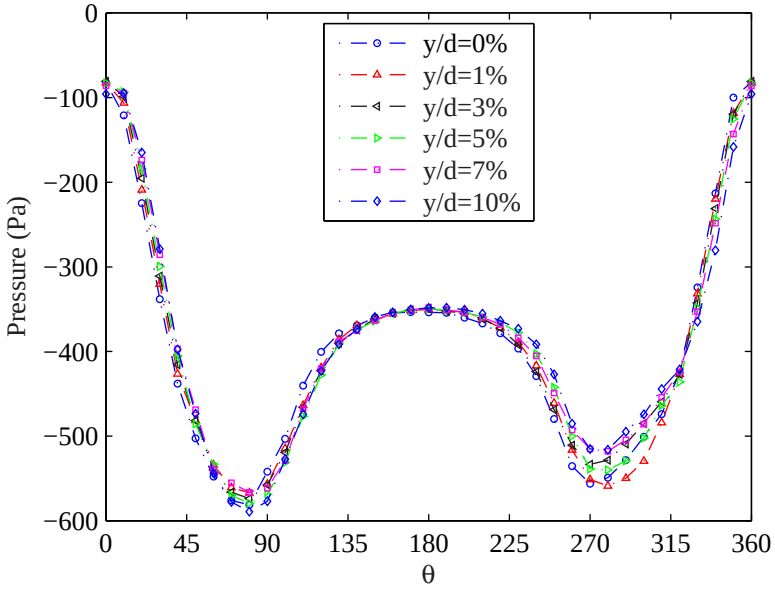

Figure F.5: $P/d = 1.58$; C_P at various tube displacements, $U = 8m/s$

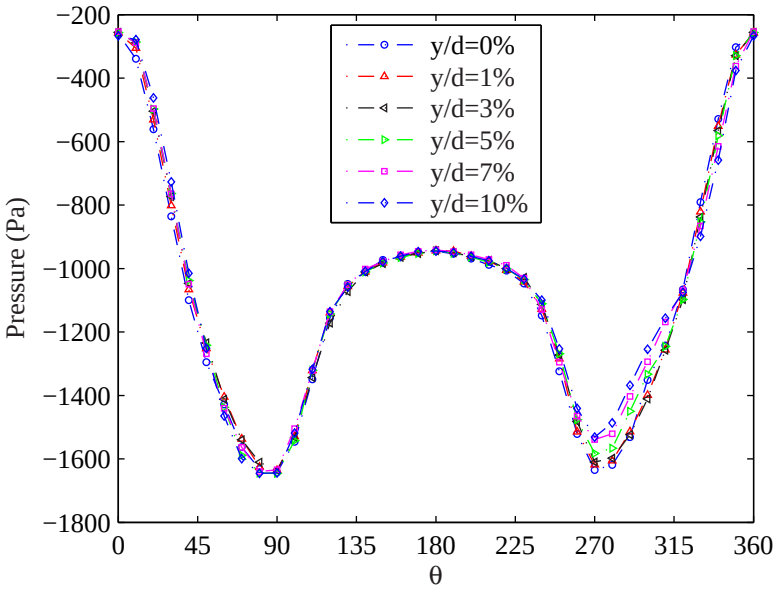

Figure F.6: $P/d = 1.58$; C_P at various tube displacements, $U = 14m/s$

F.3 Drag Force

In section 5.3.1 results on the drag force and drag coefficient were presented. For $P/d = 1.32$ it was reported that effect of tube displacement was small at low Reynolds numbers. However, with increasing Reynolds number the drag coefficient increases with tube displacement. This is illustrated in Figs. F.7 and F.8. The behaviour of the drag force and drag coefficient is investigated in this section. This is achieved by examining the additional contribution to the drag force resulting from tube displacement. The change in drag profile as a result of tube displacement is shown in Figs. F.9, F.10 and F.11. These where obtained by removing the drag profile at $y/d = 0\%$ from the profile at the various displacements tested.

It was observed that there was a change in pressure at the front of the cylinder when it was displaced. For all Reynolds numbers it was found that the additional positive and negative contributions to the drag force either side of the front stagnation point generally cancel resulting in a redistribution of the drag force around the cylinder but no additional net force. In the region after the minimum inter-row gap it was observed from the pressure distribution that a kink developed on the side of increasing blockage as a result of tube displacement. At lower Reynolds numbers the additional

contribution from this region was negligible cancelling with the opposite side of the cylinder. As the Reynolds number was increased a net positive contribution to the drag force resulted at all displacements. The other noticeable changes occurred at the rear of the cylinder. At displacements up to 5% a negative contribution as a result of tube displacement results. However, as the tube displacement $(1 - 5\%)$ was increased the contribution diminishes. Beyond a tube displacement of 5% a net positive drag contribution results. The observations at the rear of the cylinder applied at all Reynolds numbers tested.

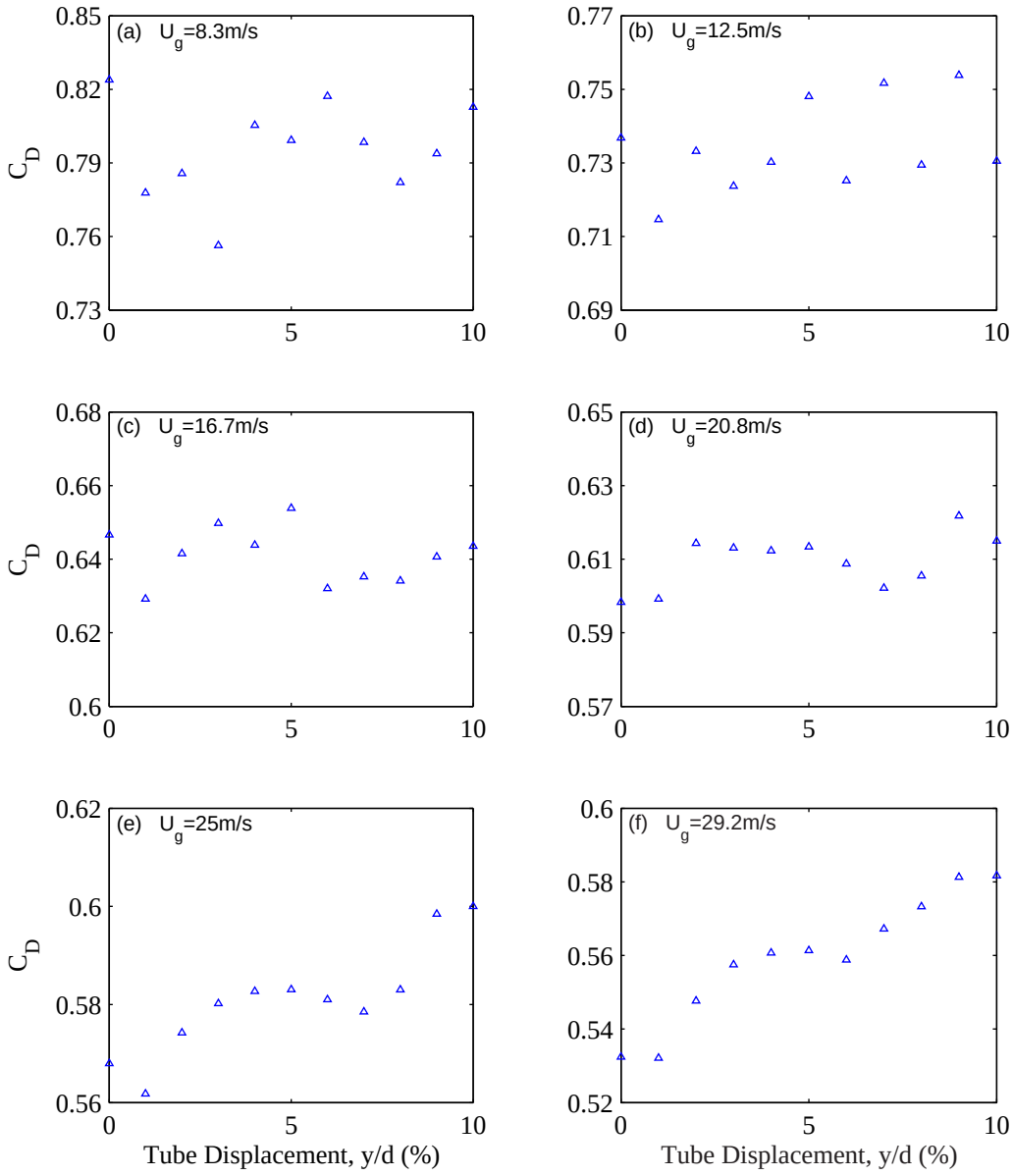

Figure F.7: $P/d = 1.32$; Drag coefficient at various velocities. Part 1

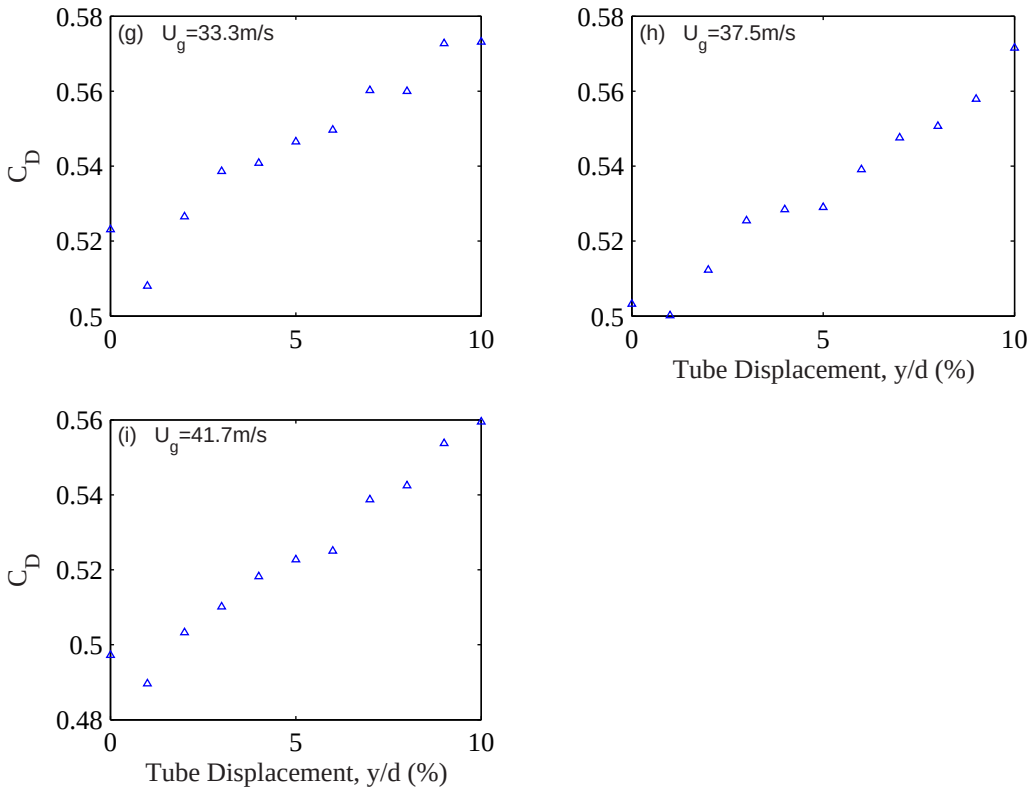

Figure F.8: $P/d = 1.32$; Drag coefficient at various velocities. Part 2

For $P/d = 1.58$ the largest changes in pressure distribution as a result of tube displacement where observed at the front of the cylinder and the region around the base coefficient. Like $P/d = 1.32$ the net contribution to the drag force at the front of the cylinder was small as the effects either side of the stagnation point were nullified. At the region around the base coefficient the change in pressure was significant, however, the contribution to the drag force in that region was small. So as concluded in section 5.3.1 the effect of tube displacement on the drag force was small for $P/d = 1.58$ with the variability observed when the tube was displaced attributed to the jet switching in this pitch ratio.

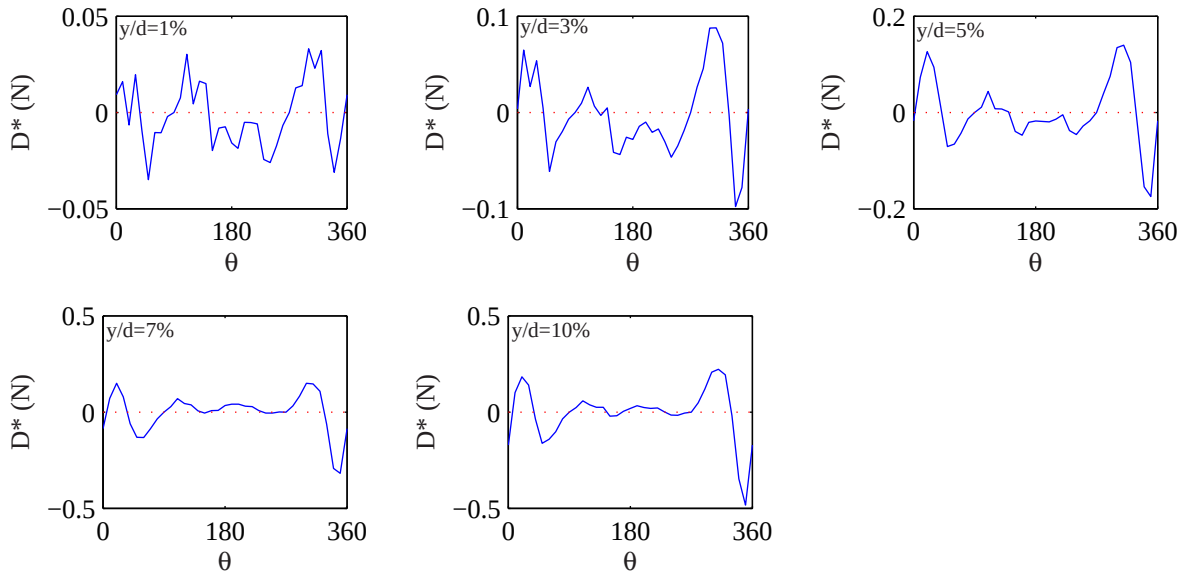

Figure F.9: $P/d = 1.32$; Drag Force generation, $U = 4m/s$, $y/d = 1$, 3, 5, 7 and 10%

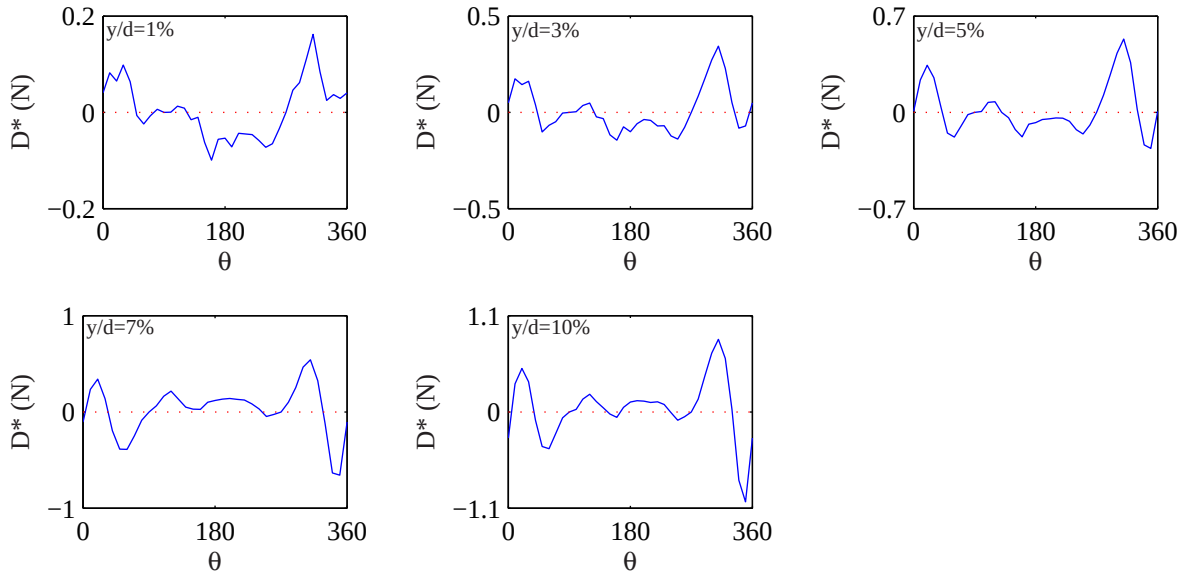

Figure F.10: $P/d = 1.32$; Drag Force generation, $U = 7m/s$, $y/d = 1$, 3, 5, 7 and 10%

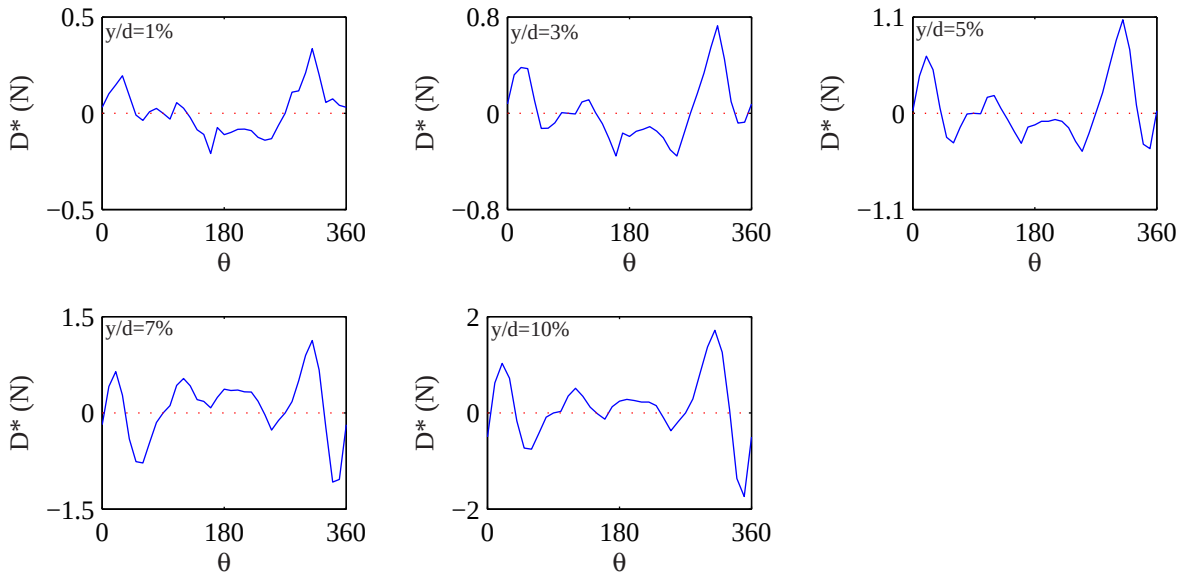

Figure F.11: $P/d = 1.32$; Drag Force generation, $U = 10m/s$, $y/d = 1$, 3, 5, 7 and 10%

F.4 Lift Force

In section 5.3.2 it was detailed that the lift force increases with tube displacement and increasing Reynolds number. The lift coefficient on the contrary increases at low Reynolds numbers. As the Reynolds number is increased further, the rate at which the lift coefficient increases, reduces. At higher Reynolds number the lift coefficient reduces. Examining the lift force against tube displacement for all velocities tested, it was observed (Figs. F.12 and F.13) that as the Reynolds number was increased beyond 4.5×10^4 the bulk of the lift generated occurred by $y/d = 4\%$. Thereafter the rate at which the lift coefficient increases with increasing tube displacement reduces. To better understand how above trend occurs, the contribution to the lift force was examined. Figures F.14 and F.15 show the contribution to the lift force for number of tube displacements and flow velocities. The lift force generation at each velocity and displacement was examined independently. The lift force was in the direction normal to the free stream flow direction. So, the cylinder can be split along a center line $(0 - 180^o)$. The difference in the lift at the same position angle but either side of the center was obtained (i.e. $lift_{\Delta 20^o} = lift_{20^o} + lift_{-20^o}$). The values at each position angle are normalised with respect to the overall lift generated.

It was observed that two main changes in the contribution to the lift force occur in the regions (a) $45 - 90^o$ and (b) $90 - 130^o$. At the lower Reynolds numbers examined ($< 3.34 \times 10^4$) the majority of the lift was generated at $\theta = 45 - 90^o$ and peaks at $\theta = 60 - 70^o$. This trend emerges at all displacements. As shown previously the pressure distribution in this region shows one of the largest changes due to tube displacement. A peak also emerges at region (b), it is thought that this peak was as a consequence of the flow separating. For the lowest Reynolds number tested it was found that as the displacement increased, the change in contribution to the lift force from the different regions around the cylinder was small with the net contribution increasing in the region $45 - 90^o$.

With increasing Reynolds number at small displacements ($y/d = 1\%$) the contribution to the lift force changes from a larger amount in the region (a) to region (b). A similar trend emerges as the tube displacement increases but rate at which energy

redistribution occurs, reduces with increasing displacement. Only at higher Reynolds numbers does the largest contribution to the lift force change from region (a) to region (b) occur. In fact at $y/d = 5\%$ the contribution to the lift force is similar in both regions. As the displacement was increased further (6%), region (a) dominates at all Reynolds numbers with contribution in this region reducing with increasing Reynolds number. The contribution to the lift force increases in region (b) but not to the extent as was observed for the smaller displacements.

Conversely, at the front of the cylinder $(0 - 35^o)$ there was a negative contribution to the lift force. The negative contribution reduced with increasing Reynolds number but increased with increasing tube displacement. This suggests that the extent of the non-recoverable pressure loss in this region was increased as the blockage increases.

For all Reynolds numbers the contribution to the lift force at the rear of the cylinder $(140 - 180^o)$ was negligible up a tube displacement of 7%. As the displacement was increased beyond 7% there was a very small change resulting in a negative contribution to the lift force. Although a small negative contribution was observed, the contribution to the overall lift generation was minimal and can realistically be ignored.

Examining the observations regarding lift generation as a whole, it was concluded that the reason for the bulk of the lift been generated at displacements up to 4% for the low-mid to high Reynolds numbers tested was as a result of the larger contribution in region (b). Also as the displacement increases there was an increasing negative contribution in the regions $0 - 35^o$ at the front of the cylinder and to a lesser extent at the rear of the cylinder $(140 - 180^o)$.

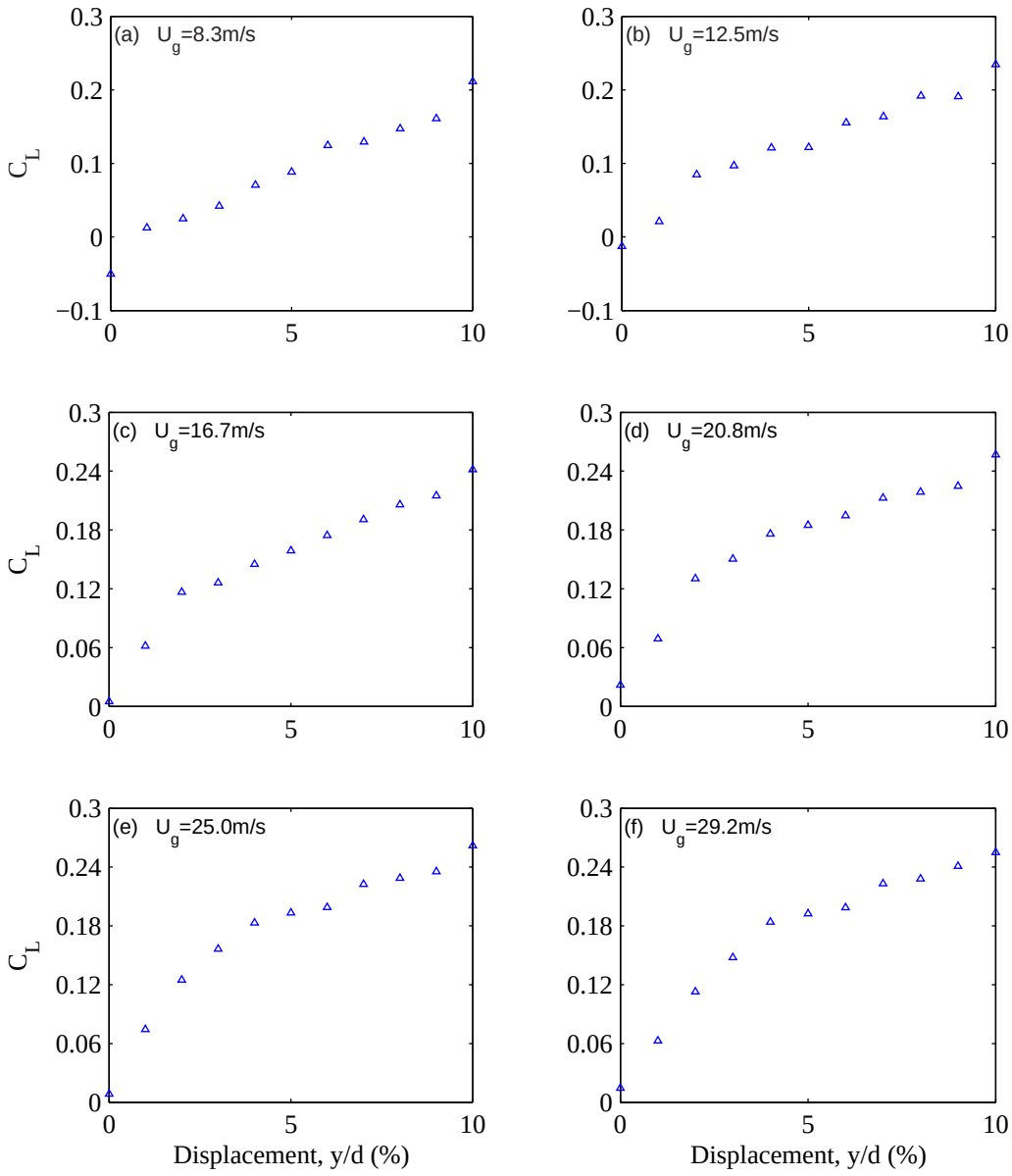

Figure F.12: $P/d = 1.32$; Lift coefficient at various velocities. Part 1

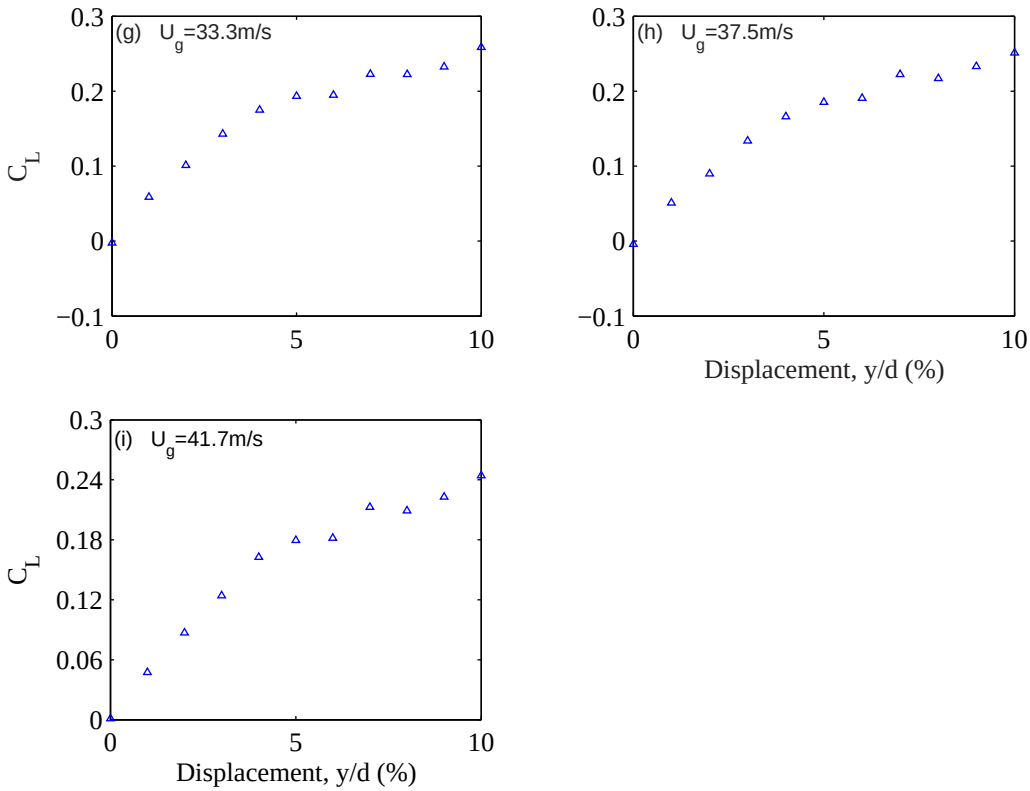

Figure F.13: $P/d = 1.32$; Lift coefficient at various velocities. Part 2

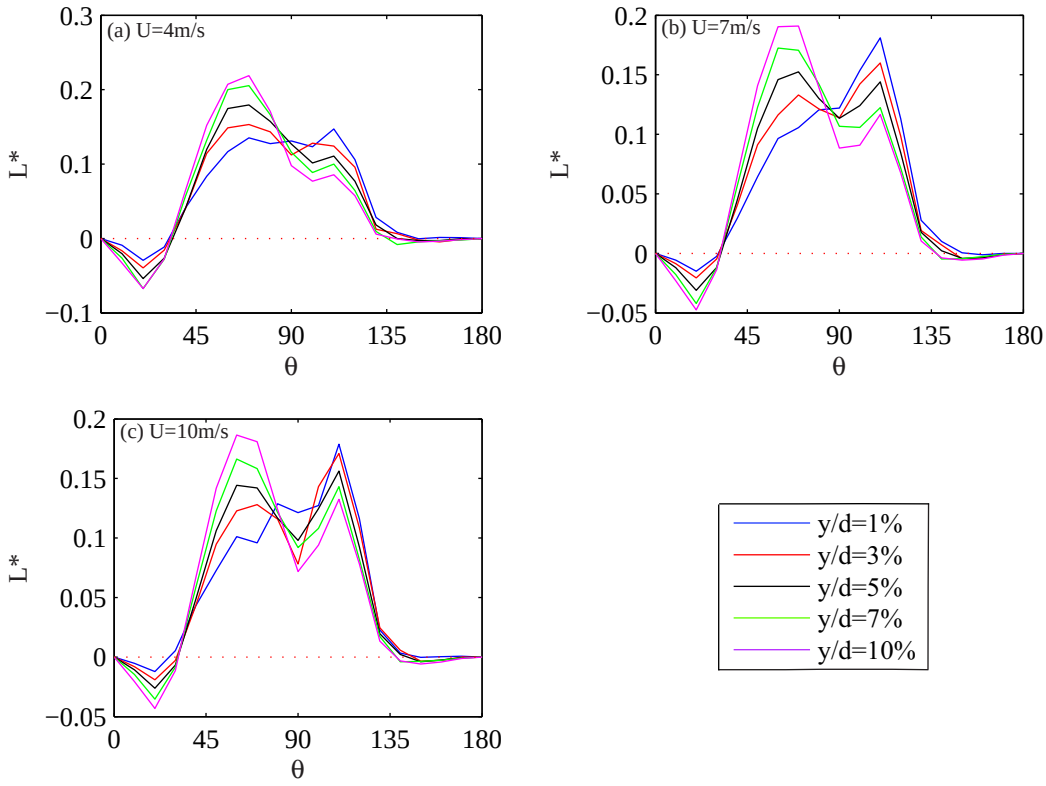

Figure F.14: $P/d = 1.32$; Lift Force generation at various displacements: 1, 3, 5, 7 and 10% at (a) $U = 4m/s$, (b) $U = 7m/s$ and (c) $U = 10m/s$

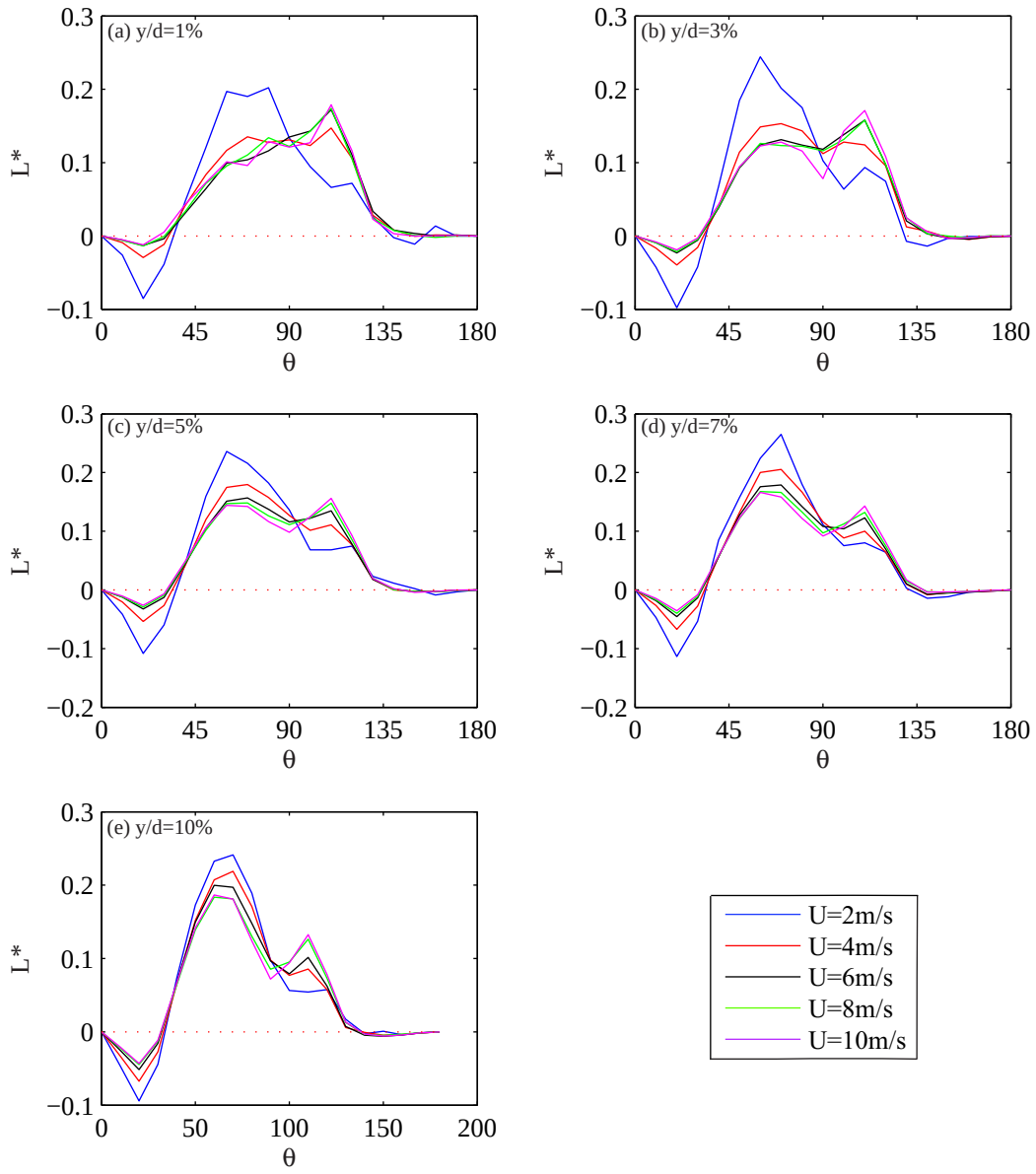

Figure F.15: $P/d = 1.32$; Lift Force generation at various velocities: $U = 2$, 4, 6, 8, and $10m/s$ at (a) $y/d = 1\%$, (b) $y/d = 3\%$, (c) $y/d = 5\%$, (d) $y/d = 7\%$, and (e) $y/d = 10\%$

For $P/d = 1.58$ it was reported that effect of jet switching resulted in the lift force behaving poorly. In general, it was shown that lift force increases with tube displacement and flow velocity, similar to that observed for the pitch ratio of 1.32. Figure F.16 shows contribution to the lift force for the pitch ratio of 1.58. At small displacements it was difficult to report definitively about the various contributions to the lift force and this lack of clarity was attributed to the jet switching observed in

this array. No real clarity in relation to the lift force generation was realised until a displacement of 7%. At the rear of the cylinder there was a negligible contribution. At the front of the cylinder there was a negative contribution which reduces with increasing Reynolds number similar to that observed for the pitch ratio of 1.32. The main contribution to the lift force was in the region $45 - 120^o$ with a peak occurring at 70^o. Because of the flow instability it is difficult to report if the contribution changes with Reynolds number or tube displacement. If it does change, the change is thought to be less than that observed for the pitch ratio of 1.32 as the geometry in the current pitch ratio was not as restrictive. The disruptive nature of the flow instability further provides evidence that, the lift force was mainly affected by local flow conditions and was only weakly affected by the bulk pressure drop across the array. This was not surprising as the affect of the bulk pressure drop on either side of the cylinder $(0-180^o)$ and $(180 - 360^o)$ will cancel and hence, the local flow features will dominate in the formulation of a lift force.

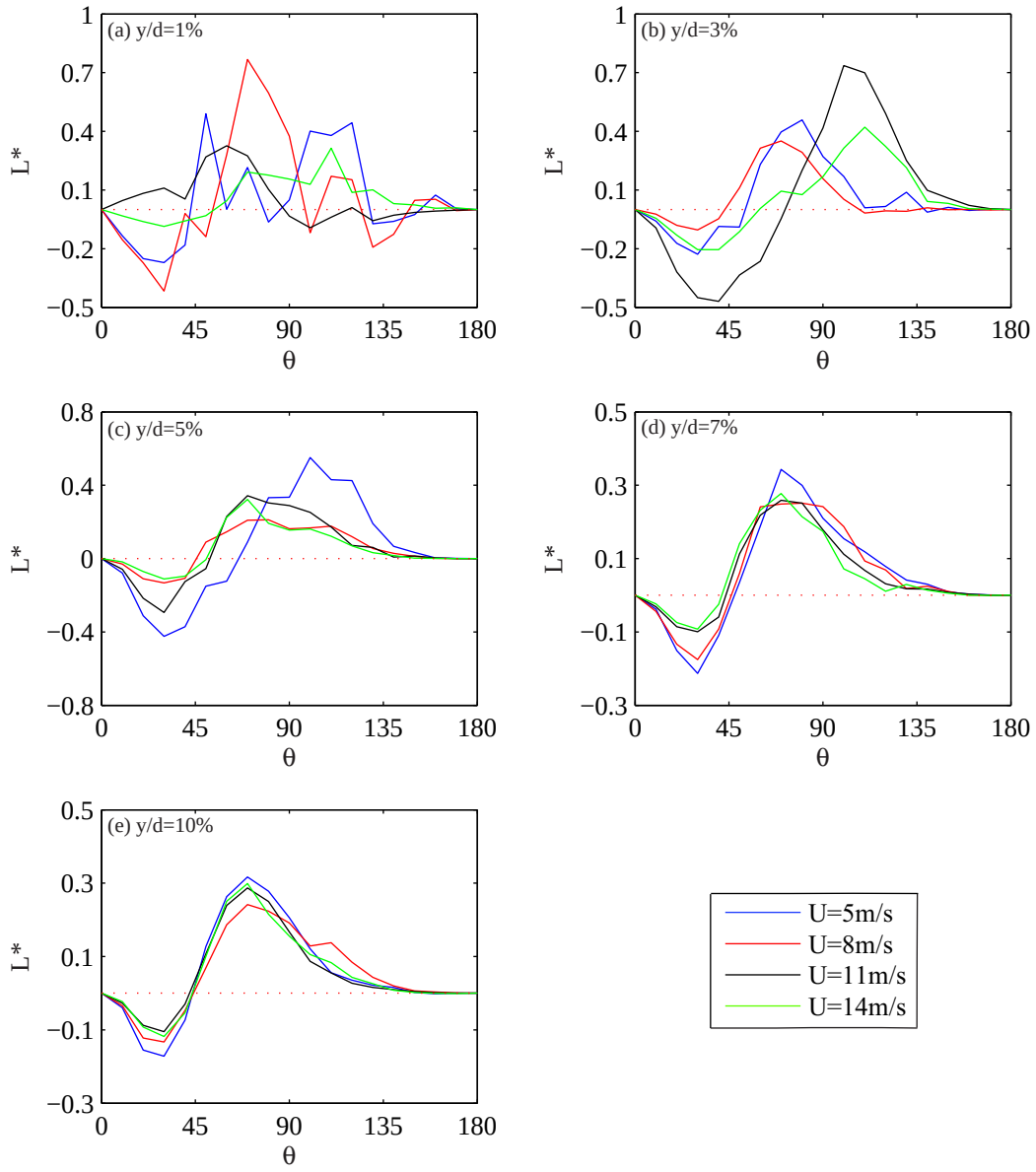

Figure F.16: $P/d = 1.32$; Lift Force generation at various velocities: $U = 5$, 8, 11 and $14m/s$ at (a) $y/d = 1\%$, (b) $y/d = 3\%$, (c) $y/d = 5\%$, (d) $y/d = 7\%$, and (e) $y/d = 10\%$